



# Janus Colloids Surfing at the Surface of Water

Xiaolu Wang

## ► To cite this version:

Xiaolu Wang. Janus Colloids Surfing at the Surface of Water. Fluid mechanics [physics.class-ph]. Université Montpellier, 2015. English. NNT : 2015MONT272 . tel-02409132

**HAL Id: tel-02409132**

**<https://theses.hal.science/tel-02409132>**

Submitted on 13 Dec 2019

**HAL** is a multi-disciplinary open access archive for the deposit and dissemination of scientific research documents, whether they are published or not. The documents may come from teaching and research institutions in France or abroad, or from public or private research centers.

L'archive ouverte pluridisciplinaire **HAL**, est destinée au dépôt et à la diffusion de documents scientifiques de niveau recherche, publiés ou non, émanant des établissements d'enseignement et de recherche français ou étrangers, des laboratoires publics ou privés.

# THÈSE

Pour obtenir le grade de  
**Docteur**

Délivré par l'**Université Montpellier**

Préparée au sein de l'école doctorale **I2S\***  
Et de l'unité de recherche **L2C - UMR 5221**

Spécialité : **Physique**

Présentée par **Xiaolu WANG**  
xiaolu.wang@univ-montp2.fr

## **Janus Colloids Surfing at the Surface of Water**

Soutenue le 11/12/2015 devant le jury composé de:

|                       |                               |                       |
|-----------------------|-------------------------------|-----------------------|
| Véronique PIMIENTA    | Professeur, Univ. Toulouse    | Président du Jury     |
| Jonathan HOWSE        | Reader, Univ. Sheffield       | Rapporteur            |
| Cécile COTTIN-BIZONNE | CdR, CNRS Lyon                | Rapporteur            |
| Thierry ONDARÇUHU     | DdR, CNRS Toulouse            | Examineur             |
| Maurizio NOBILI       | Professeur, Univ. Montpellier | Invité                |
| Martin IN             | DdR, CNRS Montpellier         | Directeur de Thèse    |
| Antonio STOCCO        | CdR, CNRS Montpellier         | Co-Directeur de Thèse |





## Acknowledgements

This manuscript of the thesis not only includes my contributions of the research but also the help from people by my side.

First of all, I'd like to thank my two supervisors, Antonio Stocco and Martin In. I am grateful to you for offering me the opportunity to come to France and work on this fascinating project. Under the patient, careful and correct guidance, I could carry on my work effectively during the past three years. Whenever I met problems, I never felt alone as you were always there for me. Each meeting we held and discussion we made helped me understand better the problems, gave me new ideas and advanced my work. I always received answers from you to the questions I had on the phenomena I've observed in the experiments, which may sometimes be naive. This helped me accumulate knowledge step by step and be able to grasp the highlights which constituted parts of my thesis.

Then, I'd like to thank the referees of my thesis, Jonathan Howse and Cécile Cottin-Bizonne, and all the other members of the jury, Véronique Pimienta, Thierry Ondarçuhu and Maurizio Nobili, for reading my manuscript and giving me pertinent remarks. It's my pleasure and honor to show you my work. Especially, I am grateful to Maurizio Nobili for following my work in the past three years and the contributions to the program *IDL*. I also would like to thank Jonathan Howse for pointing out not only the scientific problems but also the grammar mistakes I've made in the written English of the manuscript.

Thanks a lot to my colleagues in Soft Matter group, in particularly people who contributed directly to my work. I'd like to thank Christophe Blanc who helped me very much on the experimental setups, especially on the using of the optical microscopy for particle tracking and the gel-trapping method. Thanks a lot to Mayssa Medfai and Giuseppe Boniello for teaching me some experimental skills. I also would like to thank all the permanent colleagues, Michel Gross, Gladys Massiera, Domenico Truzzolillo, Laura Casanellas Vilageliu, Amélie Banc, Daniel Alexandre, Luca Cipelletti, Pascale Fabre, Christian Ligoure, Julian Oberdisse and Laurence Ramos. At the same time, many thanks to the Ph.D. and Post-doctoral students, Octavio, Srishti, Alexandra, Valentin, Clara, Stefano, Dario, Luca, Dafne, Yassine, Adrian and Rym. We've spent much time together for the weekly group seminar and shared ideas and knowledge.

I appreciate Frédéric Pichot and Christophe Roblin (Centrale de Technologie en Micro et Nanoélectronique, Université Montpellier) helping me in preparing Janus colloids by the metal deposition technique. Thanks a lot for the help from Claude Gril and Frédéric Fernandez (Service Commun de Microscopie Electronique, Université Montpellier) on the Scanning Electron Microscopy analysis.

I also would like to thank the colleagues in the Laboratoire Charles Coulomb who made my works and life better and more enjoyable in the past three years, especially to Adoration, Jean-Christophe and Tina for the assistance. At the same time, thanks a lot to Ty and Raymond for providing me some reagents. I also thank Ludovic Berthier participating in my thesis monitoring committee (Comité de suivi de thèse).

In particular, I greatly appreciate Professor Dr. Helmuth Möhwald (Max Planck Society, Germany) not only being in my thesis monitoring committee but also giving me suggestions and



remarks on my paper. I am also very grateful to Dr. Duyang Zang (Northwestern Polytechnique University, China) who recommended me as a candidate for this Ph.D. position three years ago.

At last, I'd like to thank my parents. They support me a hundred percent from ten thousand kilometers away, even they don't know what a Janus colloid is. Many thanks to my friends here in France and in China who shared the spare time with me in real or by the internet.

I am appreciative of all the people I met and all the things happened in the past three years.

# Contents

|   |    |
|---|----|
| <b>Acknowledgements</b> .....   | i  |
| <b>Plan of the Thesis</b> .....   | 1  |
| <b>Chapter 1</b> .....  | 3  |
| 1 State of art and background.....  | 3  |
| 1.1 Active matter.....  | 4  |
| 1.2 Motion of passive and active microscale particles.....                    | 5  |
| 1.2.1 Motion of bacteria.....   | 5  |
| 1.2.2 Brownian motion.....  | 7  |
| 1.2.3 Péclet number.....  | 9  |
| 1.2.4 Motion of active colloids .....   | 9  |
| 1.3 Microscale active artificial particles .....                              | 11 |
| 1.3.1 Catalytic swimmers.....   | 11 |
| 1.3.2 Active colloids powered by external fields.....                         | 15 |
| 1.4 Self-propulsion Mechanisms.....   | 16 |
| 1.4.1 Slip condition .....  | 16 |
| 1.4.2 Self-diffusiophoresis .....   | 17 |
| 1.4.3 Bubble detachment.....  | 18 |
| 1.4.4 Self-electrophoresis.....   | 20 |
| 1.5 Passive and active motion of colloid at the fluid interface.....          | 21 |
| 1.5.1 Boundary effect.....  | 21 |
| 1.5.2 Partial wetting of colloids at the liquid surface.....                  | 22 |
| 1.5.3 Brownian motion at the water interface .....                            | 27 |
| 1.5.4 Active motion at the interface .....                                    | 30 |
| 1.6 Motivation and aim of the thesis.....                                     | 32 |
| References.....   | 32 |
| <b>Chapter 2</b> .....  | 39 |
| 2 Fabrication of Platinum-Silica Janus colloids and experimental methods..... | 39 |
| 2.1 Preparation of Janus colloids .....                                       | 39 |
| 2.1.1 Physical deposition.....  | 39 |
| 2.1.2 Chemical deposition of Pt nanoparticles.....                            | 43 |
| 2.2 Characterization of the wetting properties .....                          | 48 |
| 2.2.1 Contact angle measurements.....   | 48 |

|                  |   |    |
|------------------|---|----|
| 2.2.2            | Contact angle of liquid at planar surface and interfacial tension measurement .....             | 50 |
| 2.3              | Studying the motion of colloids at the air-water interface .....                                | 51 |
| 2.3.1            | Trapping of colloids at the water surface .....   | 51 |
| 2.3.2            | Particle tracking methods .....   | 52 |
| 2.3.3            | Pt-cap orientation from image treatments .....  | 53 |
| 2.3.4            | Trajectory analysis.....  | 53 |
| 2.4              | Conclusions .....   | 56 |
|                  | References .....  | 56 |
| <b>Chapter 3</b> | .....   | 59 |
| 3                | Wetting and orientation of Janus colloids at the surface of water.....                          | 59 |
| 3.1              | Wetting property of colloids at the interface.....  | 59 |
| 3.1.1            | Theoretical description of a colloid trapped at the interface .....                             | 59 |
| 3.1.2            | Determination of the interfacial energy terms .....   | 61 |
| 3.1.3            | Surface energy calculation of Platinum and Silica .....   | 64 |
| 3.1.4            | Contact angle dependence of the free energy .....   | 66 |
| 3.2              | Orientation of Janus colloids at the air-water interface.....                                   | 67 |
| 3.2.1            | Analytical expression of the interfacial energy as a function of orientation .....              | 67 |
| 3.2.2            | Observation of the orientation of Janus colloids .....  | 70 |
| 3.3              | Discussions.....  | 72 |
| 3.4              | Conclusions .....   | 75 |
|                  | References .....  | 75 |
| <b>Chapter 4</b> | .....   | 77 |
| 4                | Directional motion of Janus Colloids at the surface of water.....                               | 77 |
| 4.1              | Concentration, contact angle and orientation of Janus colloids at the air-water interface ..... | 77 |
| 4.2              | Trajectories.....   | 78 |
| 4.3              | Motion analysis .....   | 79 |
| 4.3.1            | Velocity autocorrelation functions .....  | 79 |
| 4.3.2            | Propulsion velocity.....  | 80 |
| 4.3.3            | Rotational diffusion coefficient.....   | 81 |
| 4.3.4            | Drift velocity and Mean squared displacement.....   | 82 |
| 4.4              | Interfacial orientation of swimming Janus colloids.....   | 85 |
| 4.4.1            | Orientation of Pt cap.....  | 85 |
| 4.4.2            | Characterization of orientation by velocity autocorrelation function.....                       | 86 |

|                                     |  |            |
|-------------------------------------|--|------------|
| 4.5                                 | Discussions and conclusions .....  | 88         |
| 4.5.1                               | Persistence of trajectory .....  | 88         |
| 4.5.2                               | Rotational diffusion time .....  | 88         |
| 4.5.3                               | Propulsion mechanism and active velocity .....   | 89         |
|                                     | References .....   | 90         |
| <b>Chapter 5</b>                    | .....  | <b>93</b>  |
| 5                                   | Rotational diffusion of Janus colloids .....   | 93         |
| 5.1                                 | Equations describing rotational motion of an active spherical Janus particle .....           | 93         |
| 5.2                                 | Active motion in bulk .....  | 95         |
| 5.2.1                               | Trajectories of active colloids in bulk .....  | 95         |
| 5.2.2                               | Velocity autocorrelation function of the motion in bulk .....                                | 96         |
| 5.3                                 | Rotational diffusion of Janus colloid in the absence of $H_2O_2$ at the surface of water ... | 98         |
| 5.4                                 | Cycloidal motion at the surface of water .....   | 100        |
| 5.4.1                               | Trajectories of active colloid at the interface .....  | 100        |
| 5.4.2                               | Velocity autocorrelation function .....  | 100        |
| 5.5                                 | Rotational motion of Janus colloid at the water surface .....                                | 103        |
| 5.6                                 | Conclusions .....  | 105        |
|                                     | References .....   | 106        |
| <b>Conclusions and Perspectives</b> | .....  | <b>109</b> |
| <b>List of symbols</b>              | .....  | <b>113</b> |



## Plan of the Thesis

The *active* motion of Janus colloidal particles at the air-water interface is the subject of the present manuscript. As it will be described in **Chapter 1**, we are dealing with the study of the motion generated by converting different forms of energy into propulsion. This motion is called *active* because it is driven by the activity of the particle which can be regarded as an engine. In the first chapter, we introduce active matter and describe the motion of self-propelled particles in a fluid, presenting examples from the literature. The focus is on colloidal particles, whose size lay between few nanometers and few microns. The fabrication and propulsion mechanisms of a special class of these particles called “Janus” will be described in detail. The motion under confinement is also introduced in the context of partial wetting. For single particles only partially wetted by a liquid (i.e. particles at the gas-liquid interface), interactions and dynamics are very different when compared to that of colloids fully immersed in the liquid bulk. Hence, the active motion of Janus colloids at the air-water interface is expected to show features reflecting some of the dynamics of partial wetting.

**Chapter 2** deals with the fabrication of spherical platinum-silica Janus colloids and also the experimental methods and protocols used throughout this Ph.D. work. Experimental results and some modeling of the partial wetting of Janus colloids are shown in **Chapter 3**.

The enhanced active motion of Janus colloids at the air-water interface is described in **Chapter 4** and the roles of the rotational motion and frictions are discussed in **Chapter 5**.

**Conclusions and Perspectives** are presented as a closing section.



# Chapter 1

## 1 State of art and background

### Introduction

Many biological living systems such as bacteria, birds or humans are all good examples of *active matter*. As a new field of soft condensed matter physics, *active matter* deals with particles which are able to take and consume energy to generate systematic movement.<sup>1</sup> Hence, many systems at very different length scales can be described as active systems.

Inspired by the nature, lab-made active matter at different length scales have been developed, and today one finds examples of artificial nanocars,<sup>16</sup> microswimmers<sup>17</sup> and robotic flies<sup>24</sup> which are able to mimic many functions of living active systems.<sup>2</sup> For micronized objects, the swimming in liquid at low Reynolds number competes with the Brownian diffusion. Natural evolution finds ways to generate propulsion in these conditions. For example, *E. coli* (*Escherichia coli*) use flagella rotation and chemical sensing to propel themselves, search for food and flee from poison.<sup>28</sup> The current microscale active artificial devices themselves are designed to break time-reversal symmetry or symmetry in particle compositions, shape or surface reactions, in order to propel at low Reynolds number.<sup>2</sup> Self-generated gradients are used as means of breaking symmetry to achieve autonomous motion. Catalytically propelled devices such as bi-metallic rods and spherical Janus colloids convert internal chemical energy into mechanical work. Electric field, magnetic field and light illumination are also used as external energy sources to drive autonomous movements.<sup>3</sup>

Active artificial devices have valuable potential applications in a diversity of fields like medical, biological, material, and environmental science. Motivated by this versatility, most currently autonomous swimmers in the microscale have been designed to produce intrinsically controllable propulsion within the constraints of unavoidable Brownian rotational diffusion. In fact, directional motion due to the self-propulsion is not persistent at large time scale. In many cases, the direction of the motion changes after a characteristic time which is the Brownian rotational diffusion time.<sup>4</sup> Self-propulsion mechanisms like bubble detachment,<sup>5</sup> self-diffusiophoresis<sup>4</sup> and self-electrophoresis<sup>6</sup> have been implemented for colloidal systems. For every mechanism, the roles of interfacial forces and frictions are of key importance for the directional transport in liquid.

Self-propulsion can also be generated by exploiting interactions and properties of liquid-gas and liquid-liquid interfaces. Self-propelling liquid droplets at the gas-liquid or in a liquid bulk move due to self-generated Marangoni flows created by non-equilibrium chemical or wetting conditions.<sup>7–10</sup>

Wetting and hydrodynamics of colloids at the liquid-gas interface offer specific interactions and dynamics able to enhance self-propulsion. The confinement effect given by partial wetting guarantees a truly two-dimensional motion and the asymmetric translation and rotational frictions at the liquid-gas interface could be exploited to control the motion of self-propelling systems.

In this first chapter, the main focus is on microscale active artificial particles (also called active colloids). The motion of such particles will be introduced after describing the general field of



active matter. A gallery of some artificial active colloids and related mechanisms is presented in the following sections. Towards the end, the influence of interfacial interactions on the active motion at the fluid interface is presented as the main motivation for this research.

## 1.1 Active matter

In a recent review<sup>5</sup>, the *active matter* was defined as “a collection of active particles<sup>6</sup> which absorb energy from their surroundings or from an internal fuel tank and dissipate it to engage in a variety of non-equilibrium activities, usually, but not solely, connected to motility, growth or replication”. The term *active matter* was first used by Ramaswamy<sup>13</sup> and then used in the review «Soft Active Matter»<sup>14</sup> to describe the systems “composed of self-driven units—active particles—each capable of converting stored or ambient free energy into systematic movement”.<sup>15</sup> From this broad definition, there are many systems that can be regarded as active matter, including life-forms large (e.g. humans) and small macroscopic machines and organisms, living cells, and their components such as myosin or kinesin. Examples are shown in Figure 1.1 dividing into two kinds: living and non-living active matter.

An example of living active matter in the nanoscale is kinesin. It is a protein, which belongs to a class of active particle found in eukaryotic cells and it's powered by the hydrolysis of adenosine triphosphate (ATP) and moves along microtubule filaments. This active movement of kinesin supports several cellular functions including mitosis, meiosis and transport of cellular cargo. Well studied biological active systems in the microscale are bacteria like *Escherichia coli*, *Spermatozoa*, and *Paramecia*. They are typically of a few to several tens of micrometers in size and rotating helical flagella is exploited to propel motion as snake-like or whip-like. Going into the centimeter length scale, purple snails are an example of active systems following a bubble propulsion mechanism. They live on the surface of the ocean and trap air bubbles with a layer of clear chitin to move and maintain their positions. As also shown in Figure 1.1, a large amount of anchovy fish forms a big group of active systems is able to swim in a directed way. From a physical point of view, the interactions of each fish with others and with the water medium give rise to this highly active collective motion.

Non-living active matter describes artificial devices able to propel by internal or external energy sources. It's only recently that scientists successfully constructed nano- and micro- scaled devices. This is due to the fact that it's difficult to fabricate structurally complex objects of these sizes and also it is challenging to scale down an efficient powering system. For example, the nanocar shown in Figure 1.1 has fullerene wheels that roll on a gold surface but their motion is limited by the lack of internal combustion.<sup>16</sup>

Nano- and micro- artificial active particles are fascinating systems because of potential applications in the area of microfluidic transport, drug delivery and water purification.<sup>40,51</sup> Motivated by these potential applications, scientists tried to tune the device structures, components and their powering systems to achieve controllable movements like linear or rotational motions. As shown in Figure 1.1 at the bottom, nanorods<sup>17</sup> and Janus colloids<sup>5</sup> are nowadays fabricated to move autonomously by converting chemical energy present in the aqueous phase. In some systems, the motion can be also guided by external fields.<sup>18</sup> Even if many microscale artificial active devices have been developed, motor efficiency and motion control need further improvement to be comparable with the living active systems. To tackle these issues

and discover new concepts, investigations on the behavior of artificial active particles are of great importance. Active artificial systems are, in a certain degree, imitations of natural matter. At the same time, the well-studied bacteria systems are good paradigms for active devices.

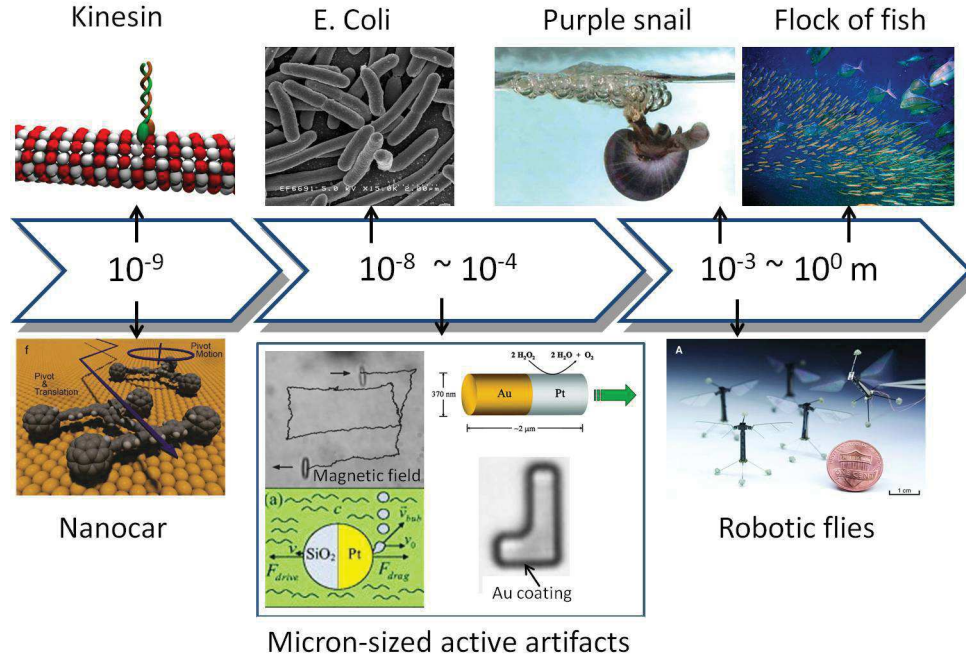


Figure 1.1 Living (top) and non-living (bottom) active matter at different scales. The living matter listed on top are: a kinesin on a microtubule ( $\sim 10\text{nm}$ ),<sup>19</sup> a swarm of *E. Coli* (a few  $\mu\text{m}$ ),<sup>20</sup> a purple snail (a few cm) swimming at water surface<sup>21</sup> and a flock of fish.<sup>22</sup> Non-living active matter shown at the bottom are: nanocars (a few nm) with C60 as wheels fabricated by Tour group,<sup>16</sup> autonomous moving catalytic microellipsoid guided by magnetic field,<sup>18</sup> nanorods,<sup>17</sup> spherical Janus colloid<sup>5</sup> and L-shaped self-propelled particle fabricated by Bechinger group<sup>23</sup> and robotic insects fabricated by Wood group.<sup>24</sup> Built refer to [2].

## 1.2 Motion of passive and active microscale particles

### 1.2.1 Motion of bacteria

For the wide amount of microorganisms living in fluids, locomotion and transport are essential aspects of life. Many bacteria like *E. coli*, Spermatozoa, and Paramecia use flagella or whip-like structures protruding from their bodies for the movement. The sizes of bacteria are typically of micrometers. The physics ruling the swimming on this micrometer scale is very different from that applying to swimming in the macro-world.<sup>25</sup> Swimming in microscale occurs at low Reynolds number where fluid friction and viscosity dominate over inertia. The Reynolds number is defined as,  $Re = \frac{\rho v L}{\eta}$  where  $\rho$  is density,  $L$  is the length,  $v$  is the particle velocity and  $\eta$  is the dynamic viscosity of the medium. The fluid flow is laminar for  $Re < 10^2$  and turbulent for  $Re > 10^3$ . In laminar flow, the viscous drag force always acts strongly on the particle moving

inside the flow. This is not the case for a man swimming in a swimming pool. Reynolds numbers of a swimming man are about  $10^4$  whereas that of bacteria is roughly  $10^{-4}$ . When we swim, a kick on feet can let us go for a while. However for microscale swimmer in laminar flow, a constant propelling force is needed to maintain the motion. Another main difference between the motion at low and high Reynold numbers is that the reciprocal motion, which is symmetric in the path of the back-and-forth movements, is non effective at low  $Re$ . This principle is stated as the scallop theorem.<sup>26</sup> A scallop in fact propel at high  $Re$  simply by opening and closing its shell fast. At low Reynolds numbers, this movement can't generate net motion.

Many bacteria achieve propulsion by rotating helical flagella and exploiting asymmetry in the drag forces they generate to achieve net motion. For example, *E. coli* uses flagella ( $\sim 10 \mu\text{m}$  long,  $\sim 20 \text{ nm}$  thick) that can form a bundle at one pole of the cell as shown in Figure 1.2 (A). Based on the sensing of the environment (chemicals or temperature), when these flagella rotate counterclockwise (CCW), the bacterium swims in a roughly straight line and “run” in the direction determined by its long axis. When one or more flagella reverse the rotational direction to clockwise (CW) and leave the bundle, a random reorientation of the bacterium occurs showing a “tumble”. This “tumble” is of a short duration and once all flagella start to rotate CCW again the bacterium starts a new run (Figure 1.2 (B)).

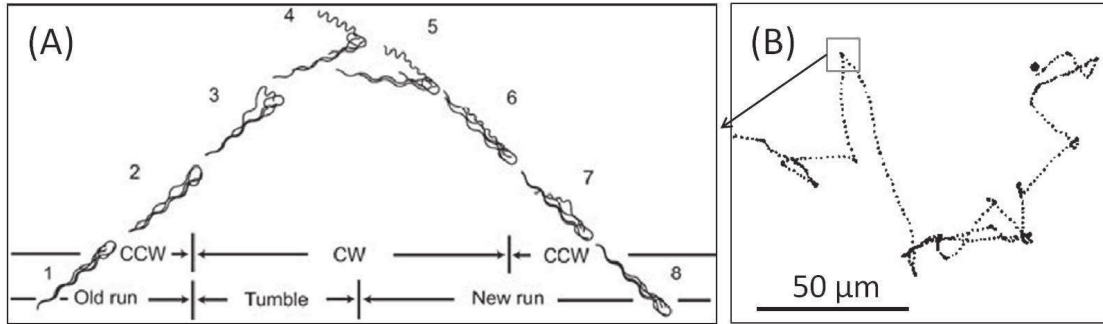


Figure 1.2 (A) Schematic bundle and rotation of flagella in run-and-tumble motion of *E. coli*.<sup>27</sup> (B) Digital plots of the displacement of a wild-type bacterium A W405.<sup>28</sup>

Mean squared displacement for “run-and-tumble” bacteria can be described as<sup>29</sup>

$$MSD(\Delta t) = \frac{2v^2}{\lambda_t^2} (\lambda_t \Delta t + e^{-\lambda_t \Delta t} - 1) \quad 1.1$$

Here  $\lambda_t$  is “tumbling rate”,  $\Delta t$  is the delay time and  $v$  is the speed of the straight motion. For times  $\Delta t \ll \lambda_t^{-1}$  (the mean run time), the motion is ballistic; for long times  $\Delta t \gg \lambda_t^{-1}$ , the motion is diffusive with the diffusion coefficient  $D_T = v^2/(2\lambda_t)$ .<sup>30</sup> For *E. Coli* the run speed is  $15 - 30 \mu\text{m s}^{-1}$ , the mean run time is  $\lambda_t^{-1} \sim 1 \text{ s}$  and the tumbling time  $\tau_t \sim 0.1 \text{ s}$ . During this short tumbling, the center of mass of the bacterium does not move and only the swimming direction changes.<sup>30</sup>

For swimmers at microscale in an aqueous medium, Brownian motion induced by collisions with water molecules also has significant interference to the directionality of their motion. However,

for bacteria such as *E. coli*, the Brownian motion has little effect given the high propulsion speed. The run-and-tumble model can serve as an idealized paradigm for non-Brownian diffusive motion and can be used to describe the motion of some artificial active particles.<sup>31,32</sup>

### 1.2.2 Brownian motion

Brownian motion of colloids is the manifestation of translational (and rotational) kinetic energy. In thermal equilibrium, the colloid experiences a dense swarm of molecules colliding with it at an extremely high frequency.<sup>33</sup> When viewing colloids through an optical microscopy, the zigzagging trajectory is observed (Figure 1.3). Plenty of physical investigations of Brownian motion have been done since the first observation of the erratic movement of pollen grains in water by Scottish botanist Robert Brown.

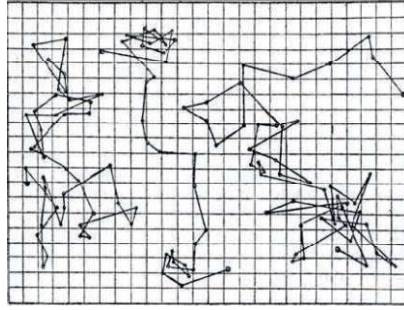


Figure 1.3 Hand-drawn particle trajectories obtained by J. Perrin in 1909.<sup>79</sup> The motion of microscopic latex particles immersed in water was observed by optical microscopy, and the image was projected on a paper sheet. The position was marked with a time interval of 30 seconds.

#### 1.2.2.1 Translational Brownian motion

A spherical colloid in a fluid phase collides with surrounding solvent molecules. The molecules hit the colloid with a quite high frequency and the colloid experiences a continuous fluid rather than a collection of discrete molecules. When the colloid starts to move, the interaction between the fluid and the colloid surface introduces a “boundary layer” near the solid surface. Within the boundary layer, because of velocity gradient, viscous stresses are produced. The viscous force on a spherical colloid inside a fluid is described as  $F_f = 6\pi\eta RV$ , where  $R$  is the particle radius,  $V$  is the velocity of moving particle and  $\eta$  is fluid viscosity. Here the Stokes friction is  $f = 6\pi\eta R$  for “no-slip” conditions.

The modified Stokes friction that accounts for a degree of slip is:<sup>33</sup>

$$f = 6\pi\eta R \frac{1+2(b/R)}{1+3(b/R)} \quad 1.2$$

where  $b$  is the slip length (see also section 1.4.1). If  $b/R = 0$ , then  $f = 6\pi\eta R$ ; whilst for  $b/R = \infty$ ,  $f = 4\pi\eta R$  (perfect slip condition).

Brownian motion equation can be derived by the Langevin equation. In the ballistic regime, the velocity of colloid has a dependence on the mass of the particle ( $m$ ). If the initial velocity of each step is always  $v$ , then the average velocity of the spherical particle is  $\langle v_s(\Delta t) \rangle = v e^{-\frac{f}{m}\Delta t}$ .

Hence, the velocity autocorrelation function ( $VACF$ ) can be written as:

$$\langle v_s(\Delta t) v_s(0) \rangle = \frac{\sigma^2}{2mf} e^{-\frac{f}{m}\Delta t}, \text{ where } \sigma^2 = 2kTf. \quad 1.3$$

The motion of a colloid is damped by viscous friction, which leads to a relaxation of the momentum. During this momentum relaxation process, the colloid travels a distance which can be related to a “ballistic” step. In this kinetic energy exchange between colloid and the surrounding solvent, a momentum relaxation time  $\tau_{mr}$  can be defined. It is the time needed to lose the momentum of the colloid due to viscous dissipation. For a spherical colloid with density  $\rho$  and radius  $R$  in a viscous fluid,  $\tau_{mr}$  is calculated as:<sup>33</sup>

$$\tau_{mr} = \frac{2}{9} \frac{\rho}{\eta} R^2 \quad 1.4$$

For example, for a standard sphere ( $\rho = 1 \text{ g cm}^{-3}$ ,  $R = 1 \mu\text{m}$ ) in water, the momentum relaxation time is  $\tau_{mr} \sim (2/9) 10^{-6} \text{ s}$ .<sup>33</sup>

After having experienced many “moment-exchanging” processes, the colloid starts to diffuse. In the diffusive regime, the net displacement of the colloid becomes independent of its mass. In reality, the momentum exchange with the solvent is a random process and the colloid steps towards each direction with the same probability. Therefore, the average displacement is zero but not the mean squared displacement. Mean squared displacement ( $MSD$ ) is proportional to:

$$MSD \sim \frac{kT}{f} \Delta t, \text{ for } \Delta t \gg \tau_{mr}, \quad 1.5$$

where  $kT$  is the thermal energy. This equation illustrates that in the diffusive time regime the mean squared displacement grows linearly in time. The proportionality constant is the translational diffusion coefficient  $D_T = \frac{kT}{f}$ . For a colloid diffusing in one dimension the mean squared displacement is  $MSD = 2 D_T \Delta t$  and in  $n$ -dimension  $MSD = 2 n D_T \Delta t$ .

The translational diffusion coefficient in  $n$ -dimension can be measured using the  $MSD$  analysis and also the velocity autocorrelation function:

$$D_T = \frac{1}{n} \int_0^\infty \langle v_s(\Delta t) v_s(0) \rangle dt = \frac{kT}{f} \quad 1.6.$$

### 1.2.2.2 Rotational Brownian motion

Besides the translational motion, colloids experience rotational kinetic energy exchange with surrounding solvent molecules. Angular momentum relaxation time ( $\tau_{ar}$ ) is on the same time scale as the translational momentum relaxation,  $\tau_{ar} = \frac{1}{15} \frac{\rho}{\eta} R^2$  (for a standard sphere  $\rho = 1 \text{ g/cm}^3$ ,  $R = 1 \mu\text{m}$  in water, the ballistic time is  $\tau_{ar} \sim (1/15) 10^{-6} \text{ s}$ ).

When  $\Delta t \gg \tau_{ar}$ , the spherical colloid enters in the diffusive regime, and its orientation changes significantly. A rotational diffusion time can be defined by:

$$\tau_R = \frac{1}{D_R}, \quad 1.7$$

where  $D_R = \frac{kT}{f_R} = \frac{kT}{8\pi\eta R^3}$  is the rotational diffusion coefficient and  $f_R = 8\pi\eta R^3$  is the rotational friction in no-slip condition. The modified rotational friction accounting for a degree of slip can be described as:  $f_R = \frac{8\pi\eta R^3}{1+3(b/R)}$ .

For delay time  $\Delta t$ ,  $\tau_{ar} \ll \Delta t \ll \tau_R$ , the mean squared angular displacement (*MSAD*) of a spherical colloid rotating about  $n$ -axis is:

$$MSAD = 2n D_R \Delta t, \text{ for } D_R \Delta t \ll 1 \quad 1.8.$$

### 1.2.3 Péclet number

In the previous two sections, we described two different kinds of motion: the “run-and-tumble” motion of bacteria and the Brownian motion of colloids. For bacteria as *E. coli* with high swimming speed (15-30  $\mu\text{m/s}$ ) the Brownian motion influence is quite small. However, for most artificial active particles possessing low speeds, active motion competes with Brownian motion. A way to describe this competition is to consider the Péclet number of the active particle.

Péclet number (Pe) is a dimensionless number defined as the ratio of the rate of advection and the rate of diffusion. By comparing advective and diffusive time scales, the Péclet number describes the noise for the dynamics of microswimmers. The self-advection time scale is  $R/V$ , where  $V$  and  $R$  are swimmer velocity and size, respectively. The diffusive time scale is  $R^2/D_T$ . Hence, here the Péclet number can be defined by:

$$Pe = VR/D_T \quad 1.9$$

Therefore, Péclet number can be used to characterize the activity of swimmers.<sup>34</sup> Active particles with Péclet numbers  $Pe < 1$  undergo strong Brownian motion which could eventually mask the directional motion. On the contrary, for active particles with high Péclet numbers  $Pe \gg 1$  the influence of random Brownian motion may become negligible.

### 1.2.4 Motion of active colloids

#### 1.2.4.1 Velocity autocorrelation function (VACF)

Motion of active colloids could be described in terms of velocity autocorrelation function as the sum of a Brownian motion contribution and an active propulsion contribution:<sup>31</sup>

$$\langle \mathbf{v}(\Delta t) \cdot \mathbf{v}(0) \rangle = \langle \mathbf{v}_s(\Delta t) \cdot \mathbf{v}_s(0) \rangle + \langle \mathbf{v}_a(\Delta t) \cdot \mathbf{v}_a(0) \rangle \quad 1.10$$

where  $\langle \mathbf{v}_s(\Delta t) \cdot \mathbf{v}_s(0) \rangle$  is the *VCAF* of Brownian motion and  $\langle \mathbf{v}_a(\Delta t) \cdot \mathbf{v}_a(0) \rangle$  is the active motion velocity contribution. As described in equation 1.6, the translational diffusion coefficient of Brownian motion in three-dimension is  $D_T = \frac{1}{3} \int_0^\infty \langle \mathbf{v}_s(\Delta t) \cdot \mathbf{v}_s(0) \rangle d\Delta t$ . The active term  $\langle \mathbf{v}_a(\Delta t) \cdot \mathbf{v}_a(0) \rangle$  could be described by:<sup>31</sup>

$$\langle \mathbf{v}_a(\Delta t) \cdot \mathbf{v}_a(0) \rangle = \begin{cases} V^2 (\tau_R - \Delta t) / \tau_R, & \text{for } \Delta t \leq \tau_R \\ 0, & \text{for } \Delta t > \tau_R \end{cases} \quad 1.11$$

The previous equation estimates the form of the correlation of the velocity as in an ideal “run-and-tumble” model. This correlation is completely lost after a long delay time ( $\Delta t > \tau_R$ ) since the



active particle changes its orientation and motion direction. During a “run”, instead the correlation of the velocity is proportional to  $(\tau_R - \Delta t)/\tau_R$ .

A slightly different form of the *VACF* is:<sup>32</sup>

$$\langle \mathbf{v}(\Delta t) \cdot \mathbf{v}(0) \rangle = 4D_T \delta(\Delta t) + V^2 e^{-\frac{\Delta t}{\tau_R}} \quad 1.12$$

In the latter equation, the active term relaxes exponentially with a characteristic time  $\tau_R$  rather than linearly as in equation 1.11.

#### 1.2.4.2 Mean squared displacement (*MSD*)

The corresponding mean squared displacement of a particle propelled with a velocity  $V$  in two dimensions is given by<sup>4,34</sup>

$$MSD = 4D_T \Delta t + \frac{V^2 \tau_R^2}{3} \left[ \frac{2\Delta t}{\tau_R} + e^{-2\Delta t/\tau_R} - 1 \right] \quad 1.13.$$

Active colloid exhibits ballistic motion at a short time while at the longer time exhibits a diffusive regime. This results from a competition between locomotive power induced swimming and angular randomization due to the thermal rotational Brownian motion. The transition between these two regimes occurs at the rotational diffusion time  $\tau_R = 1/D_R$ . Therefore the *MSD* in two dimensions can be described as:

$$MSD = \begin{cases} 4D_T \Delta t + V^2 \Delta t^2, & \text{for } \Delta t \ll \tau_R \\ (4D_T + V^2 \tau_R) \Delta t, & \text{for } \Delta t \gg \tau_R \end{cases} \quad 1.14.$$

Hence, an effective diffusion coefficient can be defined for  $\Delta t \gg \tau_R$ ,  $D_{eff} = D_T + \frac{1}{4}V^2 \tau_R$ .

#### 1.2.4.3 Active colloid as “hot” colloid

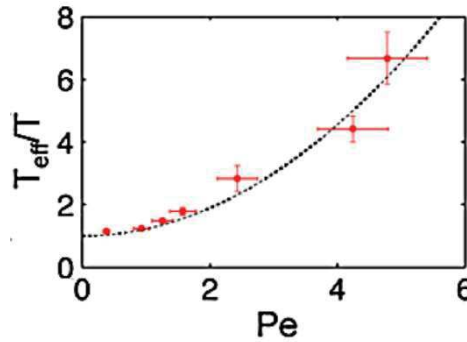


Figure 1.4 Plot of the effective temperature of active colloids normalized by ambient temperature versus the Péclet number from Ref. [34]. The dashed line is the theoretical prediction.

Different from Brownian particles which are in thermal equilibrium, microswimmers exhibit a wealth of intriguing non-equilibrium properties. As explained before, an effective diffusion

coefficient  $D_{eff}$  describing the Brownian and the active contributions can be introduced. Therefore, it's reasonable to assume that there is an effective temperature ( $T_{eff}$ ) for the active system. The theoretical expectation based on Smoluchowski diffusion-convection equation predicts:  $kT_{eff} = kT\left(1 + \frac{2}{9}Pe^2\right)$ .<sup>34</sup> In the right side of the equation, the thermal energy multiplies a term accounting the Péclet number, which represents contribution of the particle activity as described in Section 1.2.3. As reported by Palacci and coworkers, the active colloids behave as “hot” colloids, with an effective temperature much larger than the bare temperature (Figure 1.4).<sup>34</sup>

### 1.3 Microscale active artificial particles

Active artificial devices are potentially valuable in a diversity of fields like medicine, biology, material science, and environmental science. Major obstacles in the design and fabrication of artificial devices are sustainable energy sources, efficient energy conversion and motion control.<sup>2</sup>

At low Reynolds number, the system symmetry needs to be broken in order to generate motion in a persistent direction.<sup>26</sup> Current artificial devices are designed to break time-reversal symmetry, or symmetry in the particle composition, shape or surface reactions. Commonly self-generated gradients are used by these microscale active devices as a mean of breaking symmetry to achieve autonomous motion.<sup>2</sup>

Similar to that of bacteria, autonomous swimmers move as if they have their own idea of destinations. To achieve autonomous movement, usually it requires the swimmer can locally convert energy (chemical energy, light, sound, etc.) into propulsion.

#### 1.3.1 Catalytic swimmers

Chemical energy is commonly used to power biological active particles, such as the hydrolysis of ATP. The artificial microscale swimmers, as shown in Table 1.1(A), themselves behave like tiny engines which can catalyze fuels converting chemical energy into work and propulsion. One of the first swimmers powered by asymmetrical chemical reactions can be dated back to 2002 when Whitesides and co-workers fabricated millimeter scale chemically powered surface swimmers.<sup>35</sup> Until now, a large variety of such catalytic swimmers have been fabricated, including granular rods, colloidal and nanoscale particles and also complex polymer systems. Examples of microscale swimmers are shown in Table 1.1 sorted by shape and composition.

##### 1.3.1.1 Bi-metallic rods and tubes

The solid bi-metallic rods are the first reported microscale swimmers.<sup>2</sup> Normally they are constructed by an active catalytic segment and an inert part, such as platinum-gold (Pt-Au)<sup>36</sup> rod and nickel-gold rod<sup>37</sup>. Active motions of these rods in aqueous medium have been widely investigated. As shown in Table 1.1 (A1), Paxton and coworkers explored the Pt-Au rods (diameter: 370 nm; length: 2  $\mu$ m) suspended in hydrogen peroxide ( $H_2O_2$ , fuel) solution.<sup>36</sup> They found the electrochemical  $H_2O_2$  decomposition gave rise to an enhanced translation along the long axis of the rod with a translational diffusion coefficient of 23.7  $\mu$ m<sup>2</sup>/s while the speed could reach up to 6.6  $\mu$ m/s.<sup>36</sup> It was also found that metallic rods displayed an increase in directionality



along with an increase of the propulsion velocity, which pointed to a slowing down of the rotational diffusion due to the propulsion.<sup>38</sup>

To improve the efficiency of converting chemical energy into propulsion, Wang group tuned the bi-metallic rod compositions by incorporating carbon nanotubes into Pt segment (Table 1.1 (A2)).<sup>39</sup> The designed Au/Pt-CNT show a dramatically increased average speeds (50-60  $\mu\text{m/s}$ ) approaching those of natural biomolecular active particles. By adding hydrazine to the fuel, some active particles can even swim in velocity above 200  $\mu\text{m/s}$ . Furthermore, the experimental results implied that an increasing  $\text{H}_2\text{O}_2$  concentration from 0 to 15 wt% resulted in *ca.* 2 and 15-fold speed acceleration of the Au/Pt and Au/Pt-CNT active particles, respectively.<sup>39</sup>

Other studies were focused on developing the use of these self-propelled rods. Sanchez and co-workers designed a tubular microrod composed of rolled-up functional nanomembranes consisting of Fe/Pt bilayers (Table 1.1 (A3)).<sup>40</sup> The inner Pt catalyzed  $\text{H}_2\text{O}_2$  decomposition gave propulsion while the outer Fe for the generation of ferrous ions boosting the remediation of contaminated water. The velocity of this rod could reach 538  $\mu\text{m/s}$ .<sup>40</sup> The ability of these catalytically self-propelled micro active particles to improve intermixing in liquids resulted in the removal of organic pollutants *ca.* 12 times faster than the case when the Fenton oxidation process was carried out without catalytically active particles.

### 1.3.1.2 Spherical Janus colloids

Systems like metal capped spherical Janus colloids were developed and their active motions have been observed. The active Janus colloids were commonly fabricated by depositing a layer of metal (catalyst) onto spherical particles such as polystyrene and silica beads (Table 1.1 (A 4-6)).<sup>4,5,41</sup> Howse and coworkers investigated the motion of Pt-coated polystyrene Janus colloids in  $\text{H}_2\text{O}_2$  solutions.<sup>4</sup> The active colloid obtained a maximal 3  $\mu\text{m s}^{-1}$  speed and the rotational diffusion time<sup>34</sup> was found to decrease from the theoretical value of  $\sim 5.2$  s to  $\sim 3.5$  s when the fuel concentration was increased until 10%.

Pt-coated silica beads ( $\text{Pt-SiO}_2$ ) in  $\text{H}_2\text{O}_2$  solution were studied by Gibbs and Zhao (Table 1.1 (A 5)).<sup>5</sup> They showed that the propulsion velocity was dependent on the surface tension of the solution and the fuel concentration. The moving velocity had a maximal value about 6  $\mu\text{m s}^{-1}$  and the adding of surfactant led to an apparent decrease in velocity. It was also proposed a bubble detachment model to explain the scaling of the speed along with the surface tension and fuel concentration.

The motion of spherical magnesium-platinum (Mg-Pt) Janus particles (diameter: 20  $\mu\text{m}$ ) in water was investigated by Guan and coworkers.<sup>42</sup> Propulsion occurs because of the formation of hydrogen bubbles from the decomposition of water catalyzed by Mg.<sup>42</sup> This artificial particle obtained a maximal velocity of 75.7  $\mu\text{m/s}$ . The system was also biocompatible having potential applications in drug delivery and cell separation. Comparing with the bimetallic rods, the active Janus colloids showed lower propulsion speeds.

Wilson and coworkers developed a bowl-shaped polymer stomatocytes decomposed by active Pt nanoparticles.<sup>43</sup> This device is about 150 nm in dimension but could achieve the speed of 23  $\mu\text{m/s}$ . Its directional movement was generated by the rapid discharge of dioxygen produced

inside the loaded stomatocytes and the asymmetric distribution of decomposition products in a local concentration gradient.

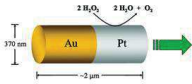
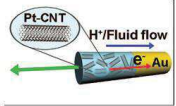
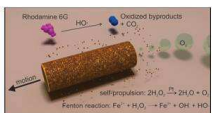
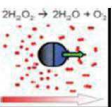
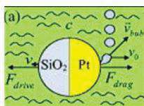

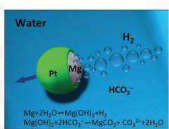
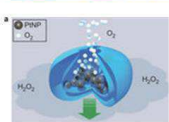
| Authors                     | Schematic Micrograph  | Dimensions                             | Components / Fuel   | Swim in:                                  | Motional Parameters   |
|-----------------------------|---|--|---|---|---|
| (A1) Sen and co-workers     |    | Diameter: 370 nm<br>Length: 2 μm       | Pt–Au / H <sub>2</sub> O <sub>2</sub>                                       | Settled near boundary in aqueous solution | Velocity: 6.6 μm s <sup>-1</sup><br>Diffusion coefficient: 23.7 μm <sup>2</sup> s <sup>-1</sup>                                   |
| (A2) Wang and co-workers    |    | Diameter: 20–81 nm<br>Length: 0.5–5 μm | Pt (CNT)–Au / H <sub>2</sub> O <sub>2</sub> + N <sub>2</sub> H <sub>4</sub> | Settled near boundary in aqueous solution | Velocity: >200 μm s <sup>-1</sup>   |
| (A3) Sanchez and co-workers |    | Diameter: 120 μm<br>Length: 500 μm     | Pt–Fe / H <sub>2</sub> O <sub>2</sub>                                       | Settled near boundary in aqueous solution | Velocity: 538 μm s <sup>-1</sup>  |
| (A4) Howse and co-workers   |    | Diameter: 1.62 μm                      | Ps–Pt / H <sub>2</sub> O <sub>2</sub>                                       | Free aqueous solution                     | Velocity: 3 μm s <sup>-1</sup><br>Diffusion coefficient: 0.31 μm <sup>2</sup> s <sup>-1</sup><br>Rotational diffusion time: 5.2 s |
| (A5) Gibbs and Zhao         |   | Diameter: 2 μm                         | SiO <sub>2</sub> –Pt / H <sub>2</sub> O <sub>2</sub>                        | Free aqueous solution                     | Velocity: 6 μm s <sup>-1</sup>  |
| (A6) Sen and co-workers     |  | Diameter: 0.96 μm                      | Au–SiO <sub>2</sub> (Grubbs ROMP catalyst) / 1,1,1-trichloroethane          | Free monomer solution                     | Velocity: 0.31 μm s <sup>-1</sup><br>Diffusion coefficient: 0.49 μm <sup>2</sup> s <sup>-1</sup>                                  |
| (A7) Guan and co-workers    |  | Diameter: 20 μm                        | Mg–Pt / H <sub>2</sub> O  | Free aqueous solution                     | Velocity: 75.7 μm s <sup>-1</sup>   |
| (A8) Wilson and co-workers  |  | Diameter: 152 ± 50 nm                  | Polymer–Pt (loaded) / H <sub>2</sub> O <sub>2</sub>                         | Free aqueous solution                     | Velocity: 23 μm s <sup>-1</sup>   |

Table 1.1 Summary of microscale catalytic swimmers. Built from Ref. [3].

### 1.3.1.3 Asymmetric Janus colloids

In many potential applications of microscale active particles such as the drug delivery, the linear propulsive motion is highly requested. However, it's clear that there are additional application areas and fundamental investigations that require the ability to produce swimming devices with well-defined spiraling and spinning trajectories. For example, micron-sized spinning colloids have been shown to influence the directional growth of neurons *in vitro*, indicating a potential use for rotating devices.<sup>44</sup> One approach to achieving rotational movement is to utilize shape asymmetry. For example, L-shape swimming devices were found to be able to generate asymmetric velocity dependent torque, resulting in constant circular trajectories (Figure 1.5

(A)).<sup>23</sup> It was also shown that effective forces and torques could be used to model the self-propulsion of microswimmers.<sup>45</sup> To explore how the movement of active particles was influenced by their own geometric asymmetry, Gibbs and coworkers fabricated catalytic (Pt coated) active particles with silica microbead heads and TiO<sub>2</sub> arms of different length (0.86-3.0  $\mu\text{m}$ ) (Figure 1.5 (B)).<sup>46,47</sup> They found that the trajectories were roughly circular and the radii of curvature became smaller along with the arm length increase. They also observed a roughly constant velocity for each arm length which indicated that the applied force and torque were exactly counter-balanced by the forces and torques resulting from hydrodynamic drag and frictional forces with the substrate. They showed that interestingly the curvature of trajectory remains roughly constant as the speed was increased in the case of the symmetric structure.

These kinds of geometrically asymmetric active devices are relatively difficult to manufacture and also their rapid sediment prevented them from exhibiting motion throughout bulk solutions.<sup>44</sup> Very recently, Ebbens *et al.* reported a simple glancing angle metal deposition method to break the symmetry of the active cap of Janus catalytic devices.<sup>44</sup> Two samples are shown in Figure 1.5 (C). For the normal catalytic half-coated Janus colloids (Figure 1.5 (C), left, glancing angle 90°), the trajectories resembled that reported previously for similar sized Janus swimmer colloids showing linear run following direction change which was subjected to Brownian rotational diffusion. However, as the glancing angle decreased (e.g. Figure 1.5 (C), right, glancing angle 0°), a dramatic change in trajectory character and increasingly tight spiraling were observed. This suggested that the higher asymmetry introduced resulted in increasing amounts of angular propulsive velocity while still maintaining a translational propulsive thrust.

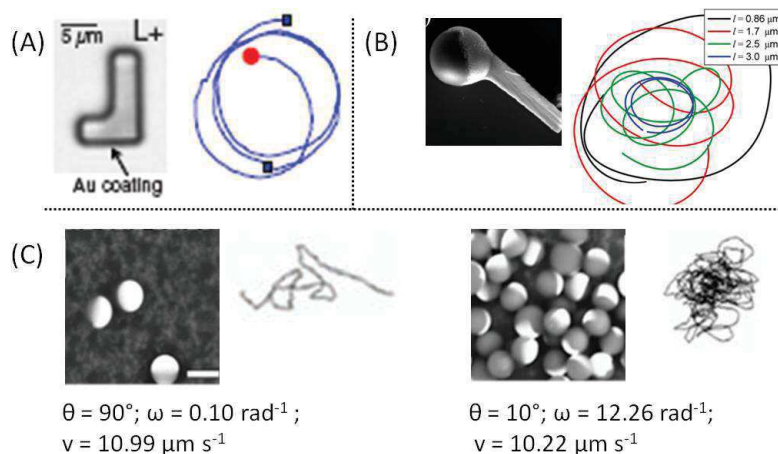


Figure 1.5 Catalytic microscale devices of asymmetric shapes. (A) L-shaped self-propelling particles moving in circular.<sup>23</sup> (B) Geometrically asymmetric catalytic active particles designed by Gibbs and coworkers performing length dependent circular motions.<sup>46,47</sup> (C) Left, Pt half-coated Janus colloids and corresponding trajectory; right, partial Pt-coated colloids by glancing angle deposition and the trajectory.<sup>44</sup>

### 1.3.2 Active colloids powered by external fields

Polarized light, magnetic field and electric field can be used to propel microscale particles. Examples are shown in Table 1.2 (B). Bechinger and coworkers fabricated gold-silica Janus colloid with a radius of  $2.13\text{ }\mu\text{m}$  (Table 1.2 (B1)).<sup>48</sup> When illuminated by a green defocused laser beam, the gold was heated. Therefore, the surrounding solvent (a mixture of water and 2,6-lutidine) de-mixed which leads to the propulsion through a self-generated local concentration gradient. The speed of colloids depended on incident light intensity. Under the maximal light intensity ( $161\text{ nW}/\mu\text{m}^2$ ) the colloids had velocity about  $0.36\text{ }\mu\text{m/s}$ .

Another common used external actuation is the magnetic field. Ghosh and Fischer reported chiral colloidal propellers that could swim in water with micrometer-level precision using homogeneous magnetic fields (Table 1.2 (B2)).<sup>49</sup> These active particles (200-300 nm in width and 1-2  $\mu\text{m}$  long) were fabricated by first depositing glass helices onto silica beads through a glancing angle deposition to form the chiral shape and following the deposition of cobalt onto their half surfaces. A coupling of translational and rotational motion was visualized for a single chiral colloid and its speed could reach  $40\text{ }\mu\text{m/s}$ . One of the advantages of active colloids working with an external energy source is that the motion direction can be also controlled simply by tuning the field.

Finally, a combination of the use of an external field on catalytic active colloids was shown by Tierno and coworkers.<sup>18</sup> They constructed autonomously moving catalytic microellipsoids which could also be guided by external magnetic fields (Table 1.2 (B3)). They found that compared with spherical active colloids the ellipsoids displayed more linear trajectories that always developed normally to their long axis. Further application of an external magnetic field allowed control of the direction of motion.

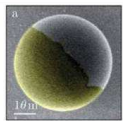
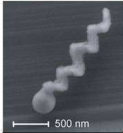
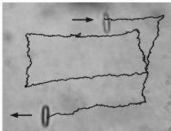
| Authors                    | Schematic Micrograph  | Dimensions  | Power          | Swim in:                                  | Velocity                       |
|----------------------------|---|---|----------------|---|--------------------------------|
| (B1) Volpe and co-workers  |  | Diameter: $4.26\text{ }\mu\text{m}$                             | Laser beam     | Mixture of water and 2,6-lutidine         | Maximal $360\text{ nm s}^{-1}$ |
| (B2) Ghosh and Fischer     |  | Diameter: $1 - 2\text{ }\mu\text{m}$                            | Magnetic field | Settled near boundary in aqueous solution | $40\text{ }\mu\text{m s}^{-1}$ |
| (B3) Tierno and co-workers |  | Aspect ratio: $6.6\text{ }\mu\text{m} : 1.6\text{ }\mu\text{m}$ | Magnetic field | Settled near boundary in aqueous solution | $4\text{ }\mu\text{m s}^{-1}$  |

Table 1.2 Summary of some microscale swimmers powered by the external field.<sup>18,48,49</sup>

## 1.4 Self-propulsion Mechanisms

### 1.4.1 Slip condition

As presented in Section 1.2.2, the translational friction in Brownian motion depends on the boundary condition. In “no-slip” condition, the relative velocity between the colloid surface and the fluid layer at its surface is zero and the viscous friction force on spherical colloid is  $F_f = 6\pi\eta RV$ . Slip boundary condition for the fluid flow along a solid wall accounts for a “slip velocity” on the solid surface (Figure 1.6).<sup>50</sup> As explained in Figure 1.6, the extrapolation length  $b$  (the Navier length or slip length) is used to characterize the amount of slip. The shear stress ( $\bar{\sigma}$ ) induces a slip velocity  $v_{slip}$  at the wall surface. The shear stress is  $\bar{\sigma} = \eta \frac{dv(z)}{dz}$ , where  $\eta$  is the fluid viscosity,  $v(z)$  is the fluid velocity and  $z$  is its distance from the wall. At the surface boundary,  $\bar{\sigma} = \frac{\eta}{b} v_{slip}$  where the slip length  $b$  is related to the surface friction coefficient ( $\tilde{\beta}$ ) by  $b = \eta/\tilde{\beta}$ .

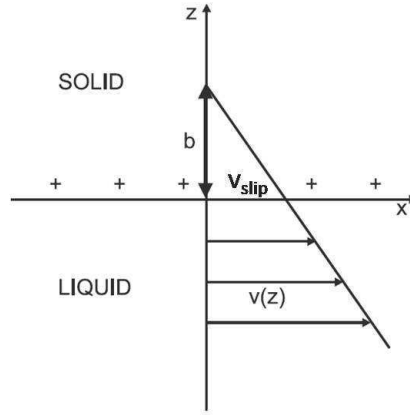


Figure 1.6 Slip condition for simple shear flow near a solid surface from Ref. [50].  $b$  is the slip length,  $v_{slip}$  is the fluid velocity at surface and  $v(z)$  is the fluid bulk velocity.

In the study of active colloids moving in aqueous media, the fluid flow close to the surface of the solid particle plays a central role in the self-phoretic mechanism. Classical phoretic transport of particles is usually induced by the interaction between the surface of each particle and the applied field. The gradient of the latter field can be generated by an electrical potential, by a temperature gradient or by concentration gradients of molecular solutes in the fluid. The speed of the particle  $V$  under the field gradient can be written as:

$$V = \mu_Y \nabla Y, \quad 1.15$$

where  $\nabla Y$  is the gradient of the field variable and  $\mu_Y$  is the slip-velocity coefficient describing the underlying phoretic mechanism. Examples of phoretic transport driven by different fields and their slip-velocity coefficients are listed in Table 1.3.<sup>51</sup>

| $V = \mu_Y \nabla Y$ ( $\nabla Y$ is a gradient of field variable, $\mu_Y$ is slip-velocity coefficient and $V$ is particle velocity) |   |   |   |
|---|---|---|---|
| Name  | Field variable $Y$                              | $\mu_Y$   | Remarks   |
| Electrophoresis   | Electrical potential                            | $-\frac{\epsilon \zeta}{4\pi\eta}$  | $\zeta$ is zeta potential of particle surface;<br>$\eta$ is fluid viscosity;<br>$\epsilon$ is the fluid dielectric constant.  |
| Diffusiophoresis  | Concentrations of a chemical species (nonionic) | $\frac{kT}{\eta} KL^*$  | $K$ is the adsorption length;<br>$L^*$ represents solute distribution.  |
| Diffusiophoresis  | Concentrations of a chemical species (ionic)    | $4 \frac{kT}{\eta} \kappa^{-2} \left[ \frac{\bar{\zeta}}{2} \beta - \ln(1 - \xi^2) \right]$ | $\bar{\zeta} = Ze\zeta/kT$ $\xi = \tanh(Ze\zeta/4kT)$<br>$Z$ is the valence of the supporting electrolyte;<br>$e$ is the charge of an electron;<br>$\kappa^{-1}$ is the Debye screening length of the solution.<br>$\beta = (D_+ - D_-)/(D_+ + D_-)$<br>$D$ are the diffusion coefficients of tow ions. |
| Thermophoresis  | Temperature                                     | $\frac{2}{\eta T} \int_0^\infty z \hbar dz$   | $\hbar$ is the local specific enthalpy increment at distance $z$ from the solid surface.  |

Table 1.3 Transport of solid colloidal particles by the phoretic process in liquids, re-built from Ref. [51].

### 1.4.2 Self-diffusiophoresis

Diffusiophoresis describes the transport of particles driven by a concentration gradient of solutes. Diffusiophoresis can be classified into two categories: ionic and nonionic diffusiophoresis, in which the molecules contributing to the gradient are charged or uncharged, respectively.<sup>51</sup> Chemical reactions taking place at the surface consume reactants and generate products, leading to concentration gradients that in turn power the motion of synthetic active particles. In these cases, the term self-diffusiophoresis has been suggested as the propulsion mechanism is generated by the active particle themselves. Asymmetry in particle composition, morphology, or reaction rate leads to an asymmetric distribution of chemical species, which breaks the symmetry of the pressure distribution and leads to directional motion of particles. The movement of particles depending on nonionic static concentration gradients has been experimentally demonstrated by Staffeld and Quinn.<sup>52</sup>

Models have been built to investigate self-diffusiophoresis mechanism for catalytic swimmers.<sup>53</sup> Considering a spherical particle of radius  $R$  with a single catalytic site on its surface, as sketched in Figure 1.7, the catalyst breaks up an available reactive substrate into product particles (diameter,  $a$ ). The catalytic site locates at  $\mathbf{r}_S = -\hat{\mathbf{z}}R$ . The resulting distribution of product particles around the sphere is asymmetric and the first moment is described as  $\rho_1(t) = \int_0^\pi \sin \theta d\theta \cos \theta \rho(r = R, \theta, t)$ , which is nonzero, leading to a phoretic motion of the sphere.<sup>53</sup> Accordingly, the spherical particle moves under this field gradient accounting for slip-velocity coefficient.<sup>51</sup> Here the gradient of products is locally generated by particle itself. The velocity of propulsion in  $z$ -axis can be expressed as:<sup>53</sup>

$$V = -\frac{kT}{\eta} \frac{\tilde{\lambda}^2}{R} \rho_1 \quad 1.16$$



Here the length scale  $\tilde{\lambda}$  represents the range of interaction between the solute and the particle. It depends on the phoretic mechanism and it is related to the effective slip length shown in the previous table 1.3.<sup>53</sup>

When the product particles are released uniformly and the reaction rate is  $k_r$ , the stationary velocity of particle is given as:

$$V = -\ell k_r, \text{ where } \ell = a \left( \frac{3\tilde{\lambda}^2}{4R^2} \right) \quad 1.17.$$

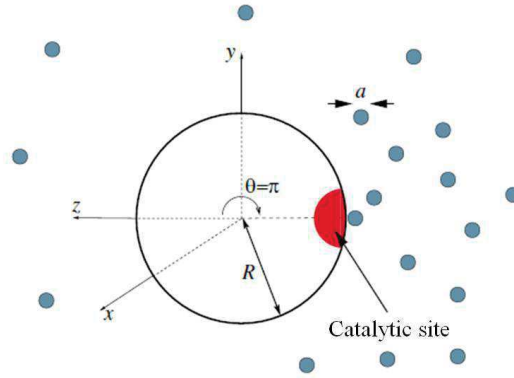


Figure 1.7 A spherical particle with a reaction site, from Ref. [53].

For an active catalytic half-coated particle, the propulsion velocity can be evaluated by<sup>4,54</sup>

$$V = \frac{3\pi}{2} k_r a \tilde{\lambda}^2 \quad 1.18$$

$k_r$  is the chemical reaction rate per unit area.

Successful prediction of how fuel concentration (e.g.  $\text{H}_2\text{O}_2$ )<sup>4</sup> and particle radius control propulsion speed support these pictures.<sup>55</sup> Nevertheless, there is also some evidence showing that this simple propulsion model cannot tell the whole story of self-propelled catalytic particles swimming in a liquid. For example, catalytic Janus swimmers have been observed moving both towards their catalytic and their non-catalytic face; and salt and anionic surfactants have both been found to reduce the swimming speed of Janus swimmers.<sup>56</sup>

### 1.4.3 Bubble detachment

For some catalytic swimmers which can generate gas bubbles through a chemical reaction, the bubble detachment mechanism determines the propulsion. For example, tubular micro-engines decompose  $\text{H}_2\text{O}_2$  into  $\text{O}_2$  and water inside the tubes leading to the formation of nano- and micro-bubbles. By spontaneous symmetry breaking, the bubbles leave the tube on one side; this implies a jet-like propulsion.<sup>57,58,59</sup> Some spherical Janus colloids can also release numerous gas bubbles<sup>42</sup> or micro-sized single bubble<sup>60</sup> to generate the propulsion.

As sketched in Figure 1.8, considering a spherical Janus colloid of radius  $R$  with one hemisphere being able to generate gas bubble through a chemical reaction, the bubble detachment mechanism suggests that the bubbles first grow at the particle surface and then bubbles eventually detach from the surface imparting momentum to the particle as they leave the particle with a finite speed ( $u_{bub}$ ).<sup>5</sup> The horizontal speed component of bubble detaching is  $u_0$ . Then the propulsion force is given as:<sup>5</sup>

$$F_p = N \frac{\Delta m}{\Delta t} (u_0 - V) \quad 1.19$$

Here  $N$  is the number of bubbles detached from the surface,  $\Delta m$  is the mass change induced by a single bubble,  $\Delta t$  is the average bubble growth time until detachment and  $V$  is particle velocity. In steady state the propulsion force is balanced by the viscous friction force  $F_f = 6\pi\eta RV$ . Therefore the particle velocity is:<sup>5</sup>

$$V \approx N \frac{\Delta m}{\Delta t} \frac{u_0}{6\pi\eta R} \quad 1.20$$

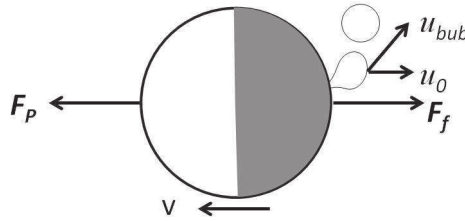


Figure 1.8 Force and velocity schematic of a spherical colloid.<sup>5</sup>

In the following, the term  $N \frac{\Delta m}{\Delta t}$  is evaluated following the Gibbs and Zhao's approach.<sup>5</sup> Assuming that the gas inside a bubble is ideal (gas density  $\rho_G$ ),  $PV' = n_m R_g T$ , where  $P$  is pressure inside bubble,  $V'$  is bubble volume,  $R_g$  is the universal gas constant,  $T$  is temperature, and  $n_m$  is the molar number. The nucleation and growth of bubble are depending on the surface tension ( $\gamma$ ) and the catalytic reaction rate  $k_r$ .  $k_r$  is determined by the adsorption of reactive substrate at catalytic surface and the chemical reaction rate constant ( $k'$ ),  $k_r = \frac{k'\alpha_L c}{1+\alpha_L c}$  ( $\alpha_L$  is Langmuir adsorption constant and  $c$  is reactive substrate concentration). The bubble size at the moment of its detachment is proportional to the surface tension ( $R_d \sim \gamma$ ). Finally, the propulsion speed of the particle can be expressed in terms of reactive substrate concentration  $c$  and surface tension  $\gamma$ .<sup>5</sup>

$$V \sim N \frac{R_g T \rho_G u_0}{\eta R P} \gamma^2 \frac{k' \alpha_L c}{1 + \alpha_L c} \quad 1.21$$

This mechanism has been proposed to explain the propulsion of catalytic Janus colloids where the detaching bubbles are assumed to be in the nano-scale.<sup>61,62</sup> This model is supported by experiments showing that the swimming velocity of the Pt-SiO<sub>2</sub> Janus particles increases along with fuel concentration and the surface tension, which could be varied using a surfactant.<sup>5</sup>



### 1.4.4 Self-electrophoresis

Following the discovery of the autonomously moving Au-Pt<sup>36</sup> and Au-Ni nanorods<sup>37</sup>, many researchers have been carried out to understand the mechanism of their catalytic energy conversion.<sup>3</sup> Experimental evidence and simulation results strongly suggested that self-electrophoresis is the dominant mechanism for catalytic active bimetallic rods. For example in the case of the Au-Pt bimetallic nano rods,<sup>36</sup> the oxidation of H<sub>2</sub>O<sub>2</sub> preferentially occurs at the anode (Pt) end and the reduction of H<sub>2</sub>O<sub>2</sub> (and O<sub>2</sub>) at the cathode (Au) end. This bipolar electrochemical reaction leads to a higher concentration of protons near the Pt end and a lower concentration near the Au end. Hence, the asymmetric distribution results in an electric field pointing from the Pt end to the Au end. The negatively charged nanorod, therefore, moves in the electric field under self-electrophoresis.<sup>6</sup>

As sketched in Figure 1.9, the charged microparticle moves in a self-generated electric field  $E_F$  as a result of an asymmetric distribution of ions at the surface.<sup>6</sup> The particle has an electrophoretic mobility of  $\mu_E = \zeta\epsilon/\eta$ , where  $\zeta$  is zeta potential of particle surface,  $\eta$  is fluid viscosity and  $\epsilon$  is the fluid dielectric constant. The particle speed is given as  $V = \mu_E E_F$ . The electric field scales as  $E_F \sim j/K$ , where  $j$  is the current density and  $K$  the conductivity of the solution. Therefore it gives a scaling relationship for the speed of:<sup>6</sup>

$$V \sim \frac{j\zeta\epsilon}{\eta K} \quad 1.22.$$

Note the analogy between the latter equation and the expression of the particle velocity in table 1.3.

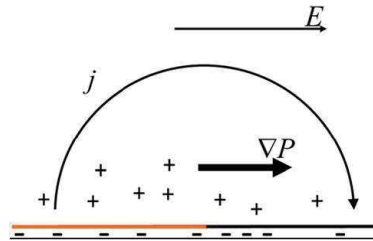


Figure 1.9 Sketch of self-electrophoresis mechanism.<sup>6</sup> An electric field  $E$  is generated at solid surface as a result of an asymmetric distribution of ions

This model was also used to explain some experimental results obtained for spherical polystyrene-Pt Janus colloids.<sup>6</sup> It was found that the particle speed could be reduced by adding salt to the fluid and the moving direction could be inverted by adding a surfactant. These results couldn't be explained by nonionic self-diffusiophoresis, at the same time the ions produced were not enough to generate a propulsion speed observed, which excluded the ionic self-diffusiophoresis mechanism. However, it supported the existence of an ionic current passing between the pole and equator of the Pt particle, as that for bimetallic swimmers, which followed self-electrophoresis mechanism.<sup>6</sup>

## 1.5 Passive and active motion of colloid at the fluid interface

### 1.5.1 Boundary effect

As we presented in the previous sections, boundary effects play a central role in the self-propulsion mechanism and the drag forces (see Section 1.4.1). As a matter of fact, self-diffusiophoresis and self-electrophoresis rely on the interactions and distributions of molecular and ionic species within boundary layers. Moreover in bubble propulsion, nucleation, growth and detachment of bubbles on the colloid surface are controlled by the wetting properties and interactions at the boundary between particle and liquid.

The motion of a particle will be also affected if the particle displacement occurs close to a liquid-solid or liquid-fluid planar interface. Hydrodynamic translational frictions of particles moving close to such interfaces differ from the bulk frictions and different drags exist both in the directions parallel and perpendicular to the interface.<sup>63,64</sup> By using the reciprocal theorem approach of Lorentz, the point force near a plane interface can be calculated and the hydrodynamic drag ratios perpendicular and parallel to the interface are:<sup>64</sup>

$$\frac{f_{T,\perp}}{6\pi\eta_2 R} = 1 + \frac{3}{8} \frac{R}{h} \frac{2+3\lambda_\eta}{1+\lambda_\eta} + \left( \frac{3}{8} \frac{R}{h} \frac{2+3\lambda_\eta}{1+\lambda_\eta} \right)^2, \quad 1.23$$

$$\frac{f_{T,\parallel}}{6\pi\eta_2 R} = 1 - \frac{3}{16} \frac{R}{h} \frac{2-3\lambda_\eta}{1+\lambda_\eta} + \left( \frac{3}{16} \frac{R}{h} \frac{2-3\lambda_\eta}{1+\lambda_\eta} \right)^2, \quad 1.24$$

where  $h$  is the distance between the particle center and the interface and  $\lambda_\eta = \eta_1/\eta_2$  is the viscosity ratio (see Figure 1.10).<sup>64</sup>

From equation 1.24, if the medium 2 is water, comparing with the friction for particles far away from interface that the friction perpendicular to the interface is higher for both of the cases: (i) close to a water-solid (solid viscosity  $\eta_1 \rightarrow \infty$ ) interface and (ii) to a water-gas (air viscosity  $\eta_1 = 1.8 \cdot 10^{-5}$  Pa s) interface. Note the  $f_{T,\perp}$  tends to be infinite for water-solid interface. Whereas, compared with that in bulk, the translational friction parallel to the interface  $f_{T,\parallel}$  near a water-solid interface is higher while near a water-gas interface is lower.

For particles straddling at the water-gas interfaces, some models have been developed to describe the drag force experienced during the translational motion. In this geometry, the drag depends significantly on the contact angle  $\alpha$  of the particle<sup>65</sup> (see Figure 1.10). Slip or no-slip boundary conditions also affect dramatically the rotational motion of particles close to or trapped at the interface. As for the translational drag, the rotational drag coefficient becomes anisotropic at the interface. A discussion on the rotational frictions for partially wetted particles will be presented in the next Section 1.5.2.

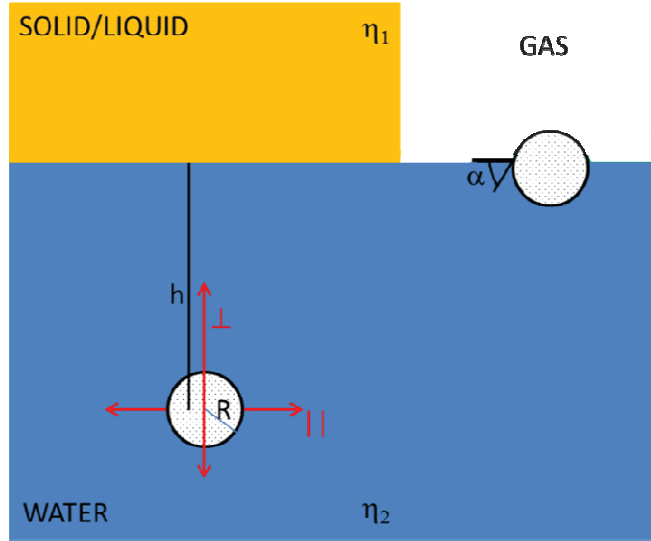


Figure 1.10 Sketch of a particle of size  $R$  (white circle), at a distance  $h$  from an interface between two media of different viscosity  $\eta$ .  $\alpha$  is the contact angle of a colloid adsorbed onto the interface.

Even if the translational drag experienced by a particle moving parallel to a solid interface is higher than the one experienced in the bulk, the coupling of the boundary effects given by the solid interface and a phoretic transport mechanism is not trivial.<sup>51</sup> In fact, it was demonstrated that the existence of a solid surface could result in higher phoretic velocity. The enhancement of the driving force could be greater than the viscous retardation, and the velocity of a particle moving parallel to a flat wall could be actually greater when it is very close to the wall than far away.<sup>66</sup>

Recently, theoretical investigations reported predictions of scenarios that could occur when an active colloid moves close to a liquid-solid interface.<sup>67</sup> A very rich scenario is expected for catalytic active colloid close to a solid wall. Reflection from the wall, motion at a steady-state orientation and height above the wall and steady “hovering” states are predicted as a function of the geometrical parameters of the Janus colloid and the hydrodynamic interactions.

In the following, we will focus on some aspects of the boundary effects given by the partial wetting of colloids at the liquid surface (e.g. air-water interface).

## 1.5.2 Partial wetting of colloids at the liquid surface

### 1.5.2.1 Young's equation

Generally, when a liquid drop is put onto a flat solid surface, at least two situations may result. If the contact angle  $\alpha$  lays between 0 and 180°, this state is called partial wetting and represented in Figure 1.11 (A) and (B) (left column). If the contact angle is zero, liquid spreads on the solid in a complete wetting state (Figure 1.11 (C), left column).

A micron-sized solid particle at the gas-liquid surface could be described as a special case of wetting, in which the solid substrate has a spherical geometry instead of being planar.

Consequently, its wettability can be described in a similar way. As sketched in Figure 1.11 (right column), when the contact angle  $0 < \alpha < 180^\circ$ , the particle straddles the liquid surface; while at  $\alpha = 0$  the particle detaches from the liquid-gas interface and it is fully wetted by the liquid.<sup>68</sup>

Considering a liquid drop on a solid substrate, three phases are present. Therefore, there are three tensions acting on the three-phase contact line: solid-liquid ( $\gamma_{S-L}$ ), liquid-gas ( $\gamma_{L-G}$ ) and solid-gas ( $\gamma_{S-G}$ ) interfacial tensions (Figure 1.12). Young's equation relates the equilibrium contact angle  $\alpha_{eq}$  to the three interfacial tensions as  $\gamma_{S-G} = \gamma_{S-L} + \gamma_{L-G} \cos \alpha_{eq}$ .<sup>69</sup>

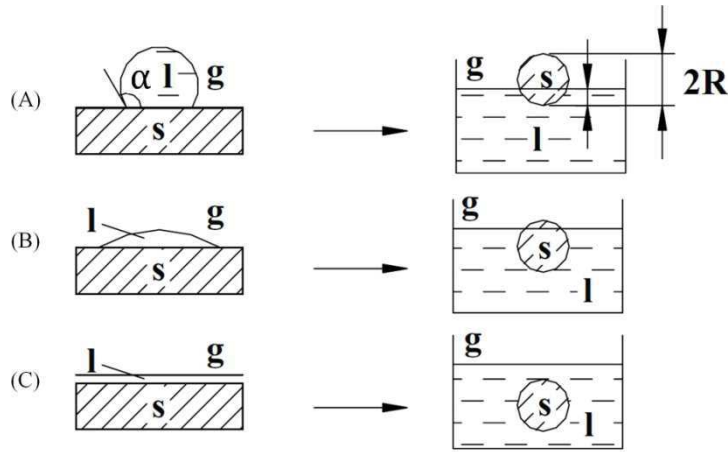


Figure 1.11 Partial wetting states for contact angle  $\alpha$ : (A)  $0 < \alpha < 90^\circ$  and (B)  $90^\circ < \alpha < 180^\circ$ . (C) Complete wetting state, i.e.  $\alpha = 0$ . Left column: a sessile drop onto a solid surface. Right column: equilibrium states of a micron-sized solid particle at the liquid-gas interface (from Ref [68]).

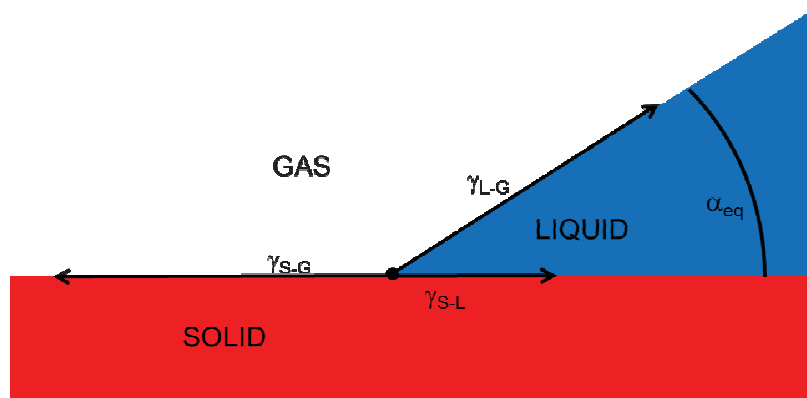


Figure 1.12 Sketch of a partial wetting state.  $\gamma_i$  represents the surface tension and  $\alpha_{eq}$  is the equilibrium contact angle.

### 1.5.2.2 Free energy of solid sphere at the gas-liquid interface

For a solid spherical particle at the liquid-gas interface, an equilibrium contact angle  $\alpha_{eq}$  can be also defined (see Figure 1.13).

Pieranski reported the calculation of the free energy of a spherical particle of radius  $R$  as a function of the relative position of the particle with respect to the interface. Assuming that the interface remains flat, the energy of the system can be calculated from the following contributions:<sup>70</sup>

- (i) the energy of the solid-gas interface,  $E_{S-G} = \gamma_{S-G} \cdot 2\pi R^2 \left(1 - \frac{z}{R}\right)$
- (ii) the energy of the solid-liquid interface,  $E_{S-L} = \gamma_{S-L} \cdot 2\pi R^2 \left(1 + \frac{z}{R}\right)$
- (iii) the energy of the missing liquid-gas interface,  $E_{L-G} = -\gamma_{L-G} \cdot \pi R^2 \left(1 - \left(\frac{z}{R}\right)^2\right)$

where  $z$  is the distance between the center of colloid and the air-water interface, with  $z$ -axis pointing towards the gas phase. Then the total energy can be written as:

$$\tilde{E} = E/\pi R^2 \gamma_{L-G} = \left(\frac{z}{R}\right)^2 - 2\frac{z}{R} \left(\frac{\gamma_{S-G} - \gamma_{S-L}}{\gamma_{L-G}}\right) + 2 \left(\frac{\gamma_{S-G} + \gamma_{S-L}}{\gamma_{L-G}}\right) - 1 \quad 1.25$$

In Figure 1.13 (B), the energy profile for a polystyrene particle ( $R = 0.12 \mu\text{m}$ ) at the water surface is reported. Plateau values correspond to the particle fully immersed in the liquid or gas phases. Adsorption energy can be calculated by the difference of the plateau value in water and the energy minimum corresponding to the equilibrium position. For polystyrene particles the adsorption energy is about  $10^6 kT$ , which indicates that the particle is irreversibly trapped at the water-gas interface.<sup>70</sup>

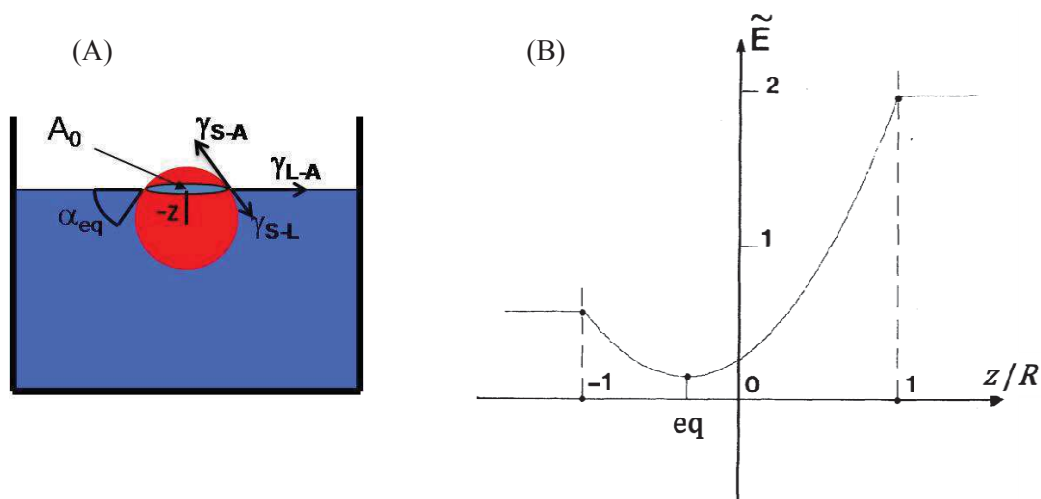


Figure 1.13 (A) Sketch of a spherical particle at the liquid-gas interface and (B) estimated surface energy well (reproduced from Ref. [70]).

### 1.5.2.3 Contact angle hysteresis

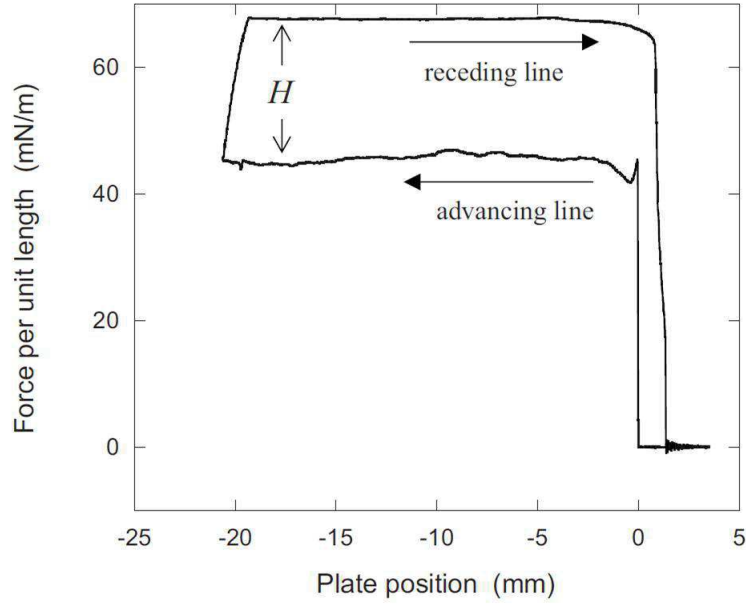


Figure 1.14 Force per unit length exerted on a plate that is immersed in a liquid and then withdrawn. From Ref. [71].

In the previous sections, we always assume that the interface is smooth and homogenous. In reality, most solid surfaces are not homogeneous. Physical (e.g. roughness) or chemical (e.g. composition) heterogeneities affect strongly the wetting behavior of a solid. Even a small heterogeneity of the solid substrate (or particle) may lead to a significant hysteresis of the contact angle. This is due to the pinning of the contact line on the defects of the substrate. Even if the size of the defects is nanometric, their effect is still visible macroscopically as a hysteresis of the contact line.<sup>69</sup> In practice, two different contact angles exist: an advancing angle  $\alpha_A$  measured by advancing the liquid meniscus on the solid; and a receding contact angle  $\alpha_R$  measured by receding the liquid meniscus.

Moulinet and co-workers described the magnitude of the hysteresis in terms of the force exerted during the motion of the contact line.<sup>71</sup> As shown in Figure 1.14, the hysteresis force (per unit length) is  $H \equiv \gamma_{L-G}(\cos \alpha_R - \cos \alpha_A)$  and can be measured directly by measuring the force exerted on a plate that is immersed in a liquid and then withdrawn.<sup>71</sup> This force and the corresponding energy can be very high and comparable to the whole surface energy of the system.

### 1.5.2.4 Dissipation in partial wetting

In partial wetting, before reaching the equilibrium contact angle the solid and the fluid move with respect to each other. This dynamics can be fast or very slow depending on the frictions and dissipations at play in the system. This applies to the cases of a drop wetting a solid substrate or a solid particle adsorbing or rotating at a fluid interface. Two main approaches have been discussed

in the literature.<sup>69,72</sup> The first one assumes that hydrodynamic shear flows in the liquid wedge of angle  $\alpha$  are the main source of dissipation in the system (see Figure 1.15). In contrast, the second approach attributes to the contact line fluctuations to be the main source of dissipation. Note that different length scales and contact angles are considered in these two approaches.

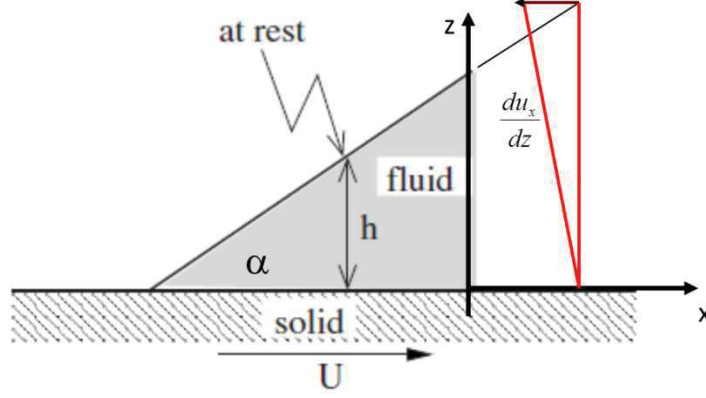


Figure 1.15 Scheme of an advancing contact line. In a frame of reference in which the contact line is stationary the solid moves with velocity  $U$  to the right. Reproduced from Ref. [69].

(i) Hydrodynamic approach: As pointed out by Huh and Scriven's paradox,<sup>73</sup> in no-slip condition, zero velocity on the solid wall implies that "not even Herakles could sink a solid" because the dissipation is infinitely large. This could be demonstrated by calculating the dissipation in the geometry shown in Figure 1.15. The solid substrate is moving from right to left with a velocity  $U$ . Hence, in a good approximation the liquid will start to move on the opposite direction with a linear gradient  $du_x/dz = U / h(x)$ , where  $h(x)$  is the height as a function of the horizontal coordinate  $x$ ,  $h(x) = x \tan(\alpha)$ . For small  $\alpha$ ,  $h(x) \approx x \alpha$ . The viscous dissipation per unit volume scales as  $\sim h \, du_x/dz$  and the dissipation rate  $\sim h \, (du_x/dz)^2$ . Hence by integrating over the wedge, the total dissipation can be calculated as<sup>69</sup>

$$\eta \int_L^{L_{out}} \left( \frac{U}{h(x)} \right)^2 h(x) dx = \eta \int_L^{L_{out}} \left( \frac{U}{x\alpha} \right)^2 x \alpha dx = \eta \frac{U^2}{\alpha} \ln(L_{out}/L) \quad 1.26$$

where  $L_{out}$  is the size of the drop and  $L$  in the equation should be equal to zero. Thus assuming a no-slip condition at the wall, i.e. zero velocity at  $L=0$ , implies that the dissipation is infinite. To overcome this paradox, one considers that  $L$  is not zero and it is a cut-off length related to a finite slip length. Doing so, one may find a very high but finite dissipation.

(ii) Contact line fluctuations: This approach considers all dissipations occurring in the immediate vicinity of the contact line at the nanoscale. As shown in Figure 1.16, the idea is that along with the contact line movement the fluid molecules jump over the corrugations. The attachment and detachment of fluid particles to or from the solid surface, which present physical or chemical heterogeneities at the nanoscale, result in dissipation at the three-phase contact line.<sup>69,74</sup>

In this model, dissipation occurs at the molecular scales but the effects are observed at the macroscopic scale. It is also assumed that the microscopic contact angle  $\alpha_m$  (at which the dissipation occurs) is identical with the experimentally observed angle, i.e.  $\alpha_m = \alpha_{eq}$ .<sup>72</sup>

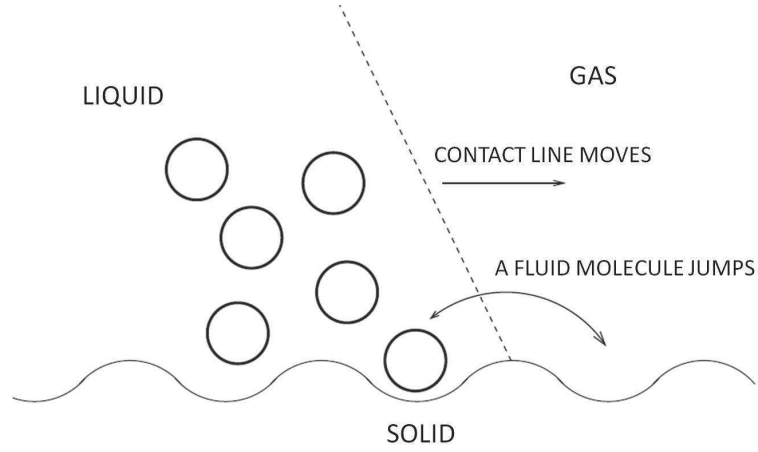


Figure 1.16 Scheme of the theory by Blake and Haynes,<sup>74</sup> associating contact line motion with the hopping of molecules between the potential wells provided by the substrate.

### 1.5.3 Brownian motion at the water interface

#### 1.5.3.1 Translational motion: Hydrodynamic prediction

As previously introduced in Section 1.5.1, the drag force experienced by particles straddling at the gas-liquid interface is dramatically dependent on the contact angle. Considering a spherical particle of radius  $R$  straddling at air-water interface with contact  $\alpha$ , as sketched in the inserted schematic in Figure 1.17, Fischer reported that the translational friction  $f = k_T^{(0)} \eta R$ , where  $k_T^{(0)}$  is a friction factor. For the friction factor at the air-liquid interface, one can consider the viscosity of air negligible and account only for the viscosity of the liquid ( $\eta$ ).  $k_T^{(0)}$  as a function of the immersion depth:<sup>65</sup>

$$k_T^{(0)} \approx 6\pi\sqrt{\tanh[32(1 - z/R)/(9\pi^2)]} \quad 1.27$$

where  $z$  is the distance between the center of colloid and the air-liquid interface.

Here the contact angle is  $\alpha = \arccos(-\frac{z}{R})$ . The translational diffusion coefficient for a particle far away from interface (in bulk) is  $f_B = 6\pi\eta R$  and the one at interface is  $f = k_T^{(0)} \eta R$ .<sup>65</sup> As shown in Figure 1.17, the ratio of  $f/f_B$  is plotted as a function of contact angle. It indicates that interfacial friction is always smaller than that in the bulk liquid ( $f < f_B$ ) and the translational diffusion for particles at the air-water interface ( $D_T = \frac{kT}{f}$ ) increases when the contact angle increases.



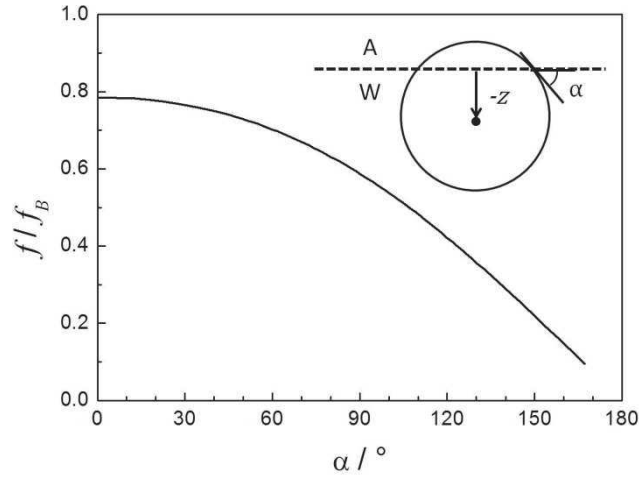


Figure 1.17 The ratio between translational friction of a particle at the interface ( $f$ ) and that of a particle in bulk ( $f_B$ ) as a function of the contact angle  $\alpha$ .

### 1.5.3.2 Translational motion: Recent experiments

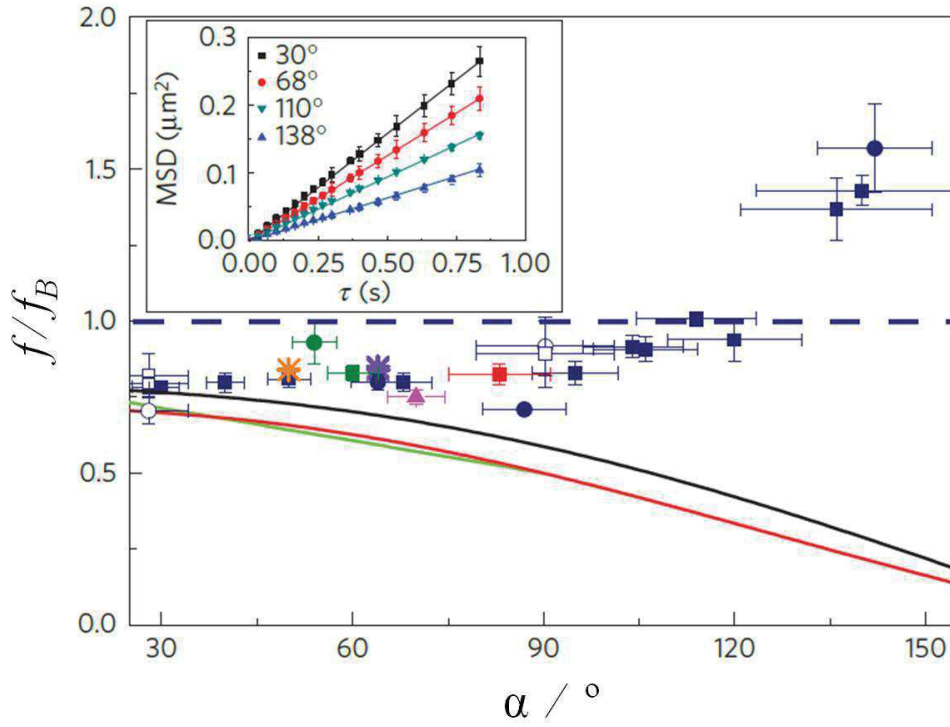


Figure 1.18 Ratio of interfacial viscous friction and that in bulk ( $f/f_B$ ) as a function of contact angle  $\alpha$ . Points represent different particles (silica (blue points), polystyrene (green points) and poly(methyl methacrylate) beads (magenta point)). Open points correspond to couples of silica beads sharing the same interface; the red point corresponds to silica beads at an air-hexanol interface. The solid lines are predictions from different hydrodynamic theories for a free air-water interface,<sup>75</sup> especially the black line is the same as that in Figure 1.17. Inserted graph is the  $MSD$  versus interval time for particles with different contact angles ( $\alpha = 30^\circ, 68^\circ, 110^\circ, 138^\circ$ ). Reproduced from Ref. [75].

Very recently Boniello and coworkers reported a full characterization of the lateral translational diffusion of micrometric spherical particles straddling an air-water interface as a function of the contact angle.<sup>75</sup> Counter-intuitively, particles diffused more slowly when the contact angle increased. Ratio of interfacial viscous friction and that in bulk ( $f/f_B$ ) increased when decreasing the immersion in water, as shown by Figure 1.18.<sup>75</sup> The interfacial friction became equal or even higher than in the bulk  $f > f_B$  for high contact angles values.

A new theoretical paradigm was developed beyond hydrodynamics to explain these results.<sup>75</sup> The thermally activated deformations of the interface at the triple line drove the system out of mechanical equilibrium and gave rise to extra random forces on the particle. Through the fluctuation-dissipation theorem, these fluctuating forces were associated with an extra viscous friction on the particle that led to the measured diffusion slowing down.<sup>75</sup> More in detail, an interface deformation occurring over a triple-line segment induced a force on the particle which added to the friction force due to the molecular collisions of the surrounding fluids. This extra dissipation could be well modeled in two limits: of a moving line, according to molecular kinetic theory (similar to the dissipation occurring in partial wetting, see Figure 1.16), and of a pinned line, taking into account capillary fluctuations of the interface.<sup>75</sup>

### 1.5.3.3 Rotational motion: Hydrodynamic prediction

Very few theoretical predictions on the rotational motion of spherical particles partially immersed in a liquid can be found in the literature.

O'Neill and coworker theoretically investigated the rotational and translational frictions for the special system of a spherical particle half-submerged in water (contact angle  $\alpha = 90^\circ$ ).<sup>76</sup> One can distinguish two rotational diffusion coefficients:  $D_{R,\parallel}$  describing the rotation about an axis parallel to the interface normal, and  $D_{R,\perp}$  describing the rotation about an axis perpendicular to the interface normal, see Figure 1.19 (Top). The latter rotation  $D_{R,\perp}$  is related to the hydrodynamic dissipation described before in partial wetting (Eqn. 1.26). In fact, the rotation about an axis perpendicular to the interface normal leads to a motion of the contact line and a relative movement between the liquid and the solid, as sketched in Figure 1.19 (Top). In this case, a no-slip condition would lead to an infinite dissipation. A non-dimensional sliding friction coefficient (defined as  $\tilde{\beta}R/\eta = R/b$ ,  $\eta$  is liquid viscosity and  $b$  is the slip length) has been introduced by O'Neill and coworker to evaluate the rotational friction about an axis perpendicular to the interface normal. The case  $R/b = \infty$  corresponds to the no-slip condition, whereas  $R/b = 0$  corresponds to the perfect slip condition.  $D_{R,\perp} = k_B T / f_{R,\perp}$  and  $f_{R,\perp} = k_{\perp}^r \eta R^3$ .<sup>76</sup>

The expression of the friction factor  $k_{\perp}^r$  is rather complex. A plot of  $k_{\perp}^r$  as a function of the sliding friction coefficient is shown below. It changes from zero in perfect slip condition to infinite in no-slip condition.

The case of  $D_{R,\parallel}$  describing the rotation about an axis parallel to the interface normal is easier to calculate given the symmetry of the problem, i.e. the spherical particle is half-submerged (contact angle  $\alpha = 90^\circ$ ). In no-slip,  $D_{R,\parallel} = \frac{kT}{4\pi\eta R^3}$  is simply the half of the bulk value  $D_R = \frac{kT}{8\pi\eta R^3}$  and for perfect slip condition,  $D_{R,\parallel} = D_R = \infty$ . In general,  $D_{R,\parallel} = \frac{kT}{k_{\parallel}^r \eta R^3}$ , where the friction factor  $k_{\parallel}^r$  is:

$$k_{\parallel}^r = 4\pi[1/(1 + 3b/R)]$$

1.28

Note that the latter friction is simply the half of the bulk rotational friction described in Section 1.2.2.2.

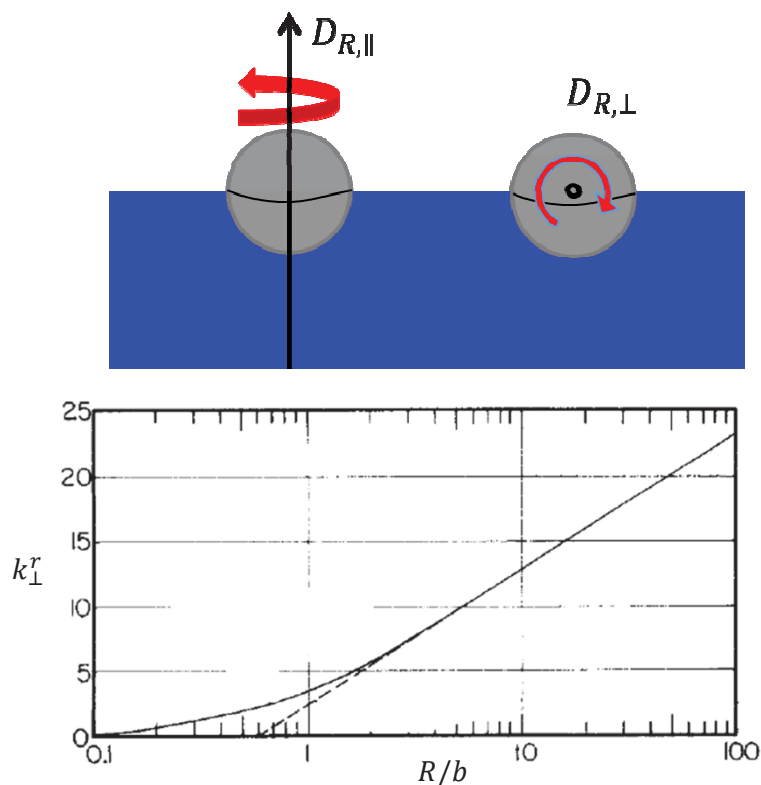


Figure 1.19 (Top) Sketch of the two rotational diffusion coefficients for a sphere half immersed inside a liquid. (Bottom) Friction factor  $k_{\perp}^r$  as a function of sliding friction coefficient  $R/b$ .

### 1.5.4 Active motion at the interface

Until now, very few experimental investigations on the motion of active colloids at liquid interfaces have been conducted.

As shown in Figure 1.20 (A), Mano and Heller reported that a carbon fiber (7  $\mu\text{m}$  in thickness and 0.5-1 cm in length) built with a terminal glucose oxidizing microanode and oxygen reducing microcathode was able to move at the water-air interface. The speed was as high as 1-0.1 cm/s due to the fast flow of current through fiber and the small viscous drag at the interface.<sup>77</sup> The propulsion was attributed to a bioelectrochemical reaction with half-reactions: one occurred at the anode functionalized with glucose oxidase (GOx) and another at the cathode functionalized with bilirubin oxidase (BOD). The proton gradients formed by the half reactions were ultimately responsible for the motion through the self-electrophoresis mechanism. They found that when the

GOx/BOD ratio was balanced for approximately similar reaction rates at the two fiber ends, the trajectory of the moving fibers was linear. However, when a small excess of GOx was applied the trajectory was spiral while for a large excess of GOx the fibers rotated around their anode.

To the best of our knowledge, only one article in literature reports on the motion of active microscale particles at the liquid-liquid interface. Sen and co-workers studied the motion of Pt-Au nanorods at the decane-water interface (Figure 1.20 (B)).<sup>78</sup> The catalytic activity of the rods on an  $\text{H}_2\text{O}_2$  aqueous subphase gave rise to anomalous translational and rotational diffusion. The rods performed a superdiffusive motion that could be decomposed into thermal orientation fluctuations and an active motion of the rods with a constant velocity along their long axis. They also proposed the autonomous nanorods for precise measurements of surface shear viscosities.

Recently, Pinchasik and co-workers studied the motion of active Janus spherical colloids close to a solid-liquid and a liquid-gas interface (Figure 1.20 C).<sup>60</sup> They fabricated spherical Ag-SiO<sub>2</sub> Janus particles and investigated the influence of interface hydrophobicity on the propulsion. A bubble formed by the decomposition of hydrogen  $\text{H}_2\text{O}_2$  split into water and oxygen on the catalytically active Ag. Particle propulsion occurred spontaneously upon bubble detachment. Changing the hydrophobicity of the supporting interface was proved to be efficient in directing and localizing particle-bubble complexes. Propelled particles adhered to hydrophobic interfaces, but detached from hydrophilic surfaces and floated in the aqueous medium until they reached the air-water interface.

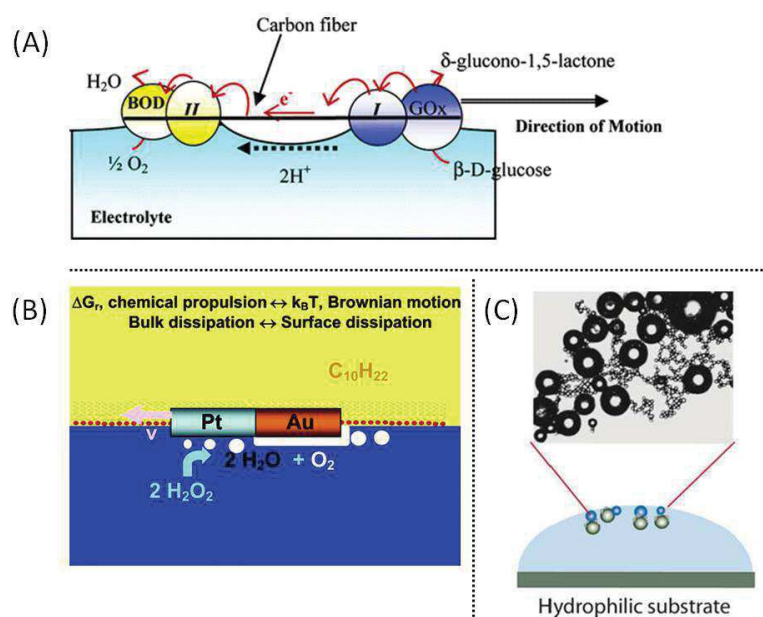


Figure 1.20 Active devices moving at interfaces. (A) Functionalized carbon fibers move at the air-water interface through self-electrophoresis.<sup>77</sup> (B) Catalytic metallic rod swimming at water-oil interface.<sup>78</sup> (C) Active colloid moving close to a water surface.<sup>60</sup>

## 1.6 Motivation and aim of the thesis

As described throughout the first chapter, asymmetry is an essential feature for the realization of active movement. The breaking of the symmetry appears in the friction coefficients of the bacteria flagellum, in the distribution of molecules and charges in self-phoretic transports and in the shape design of artificial microscale active particles.

Boundary effects govern friction and transport mechanisms. Rotational and translational frictions differ strongly when a moving particle approaches an interface. For active colloids, the rotational friction is a key parameter, which sets the time scale of the persistence of the motion. Introducing partial wetting, we discussed the asymmetric rotational frictions that colloidal particles experience at the gas-liquid interfacial plane.

This Ph.D. thesis aims at investigating experimentally the motion of catalytic Janus particles at the water surface in order to elucidate the coupling between partial wetting dynamics and the active motion. As stated before, we expect a dramatic change in terms of frictions and rotational diffusion times. Moreover, interfacial interactions may also affect the self-propulsion mechanism as it is predicted for the motion of active colloids close to a solid wall.<sup>67</sup>

## References

1. Golestanian, R. & Ramaswamy, S. Active matter. *Eur. Phys. J. E* **36**, 2012–2013 (2013).
2. Wang, W., Duan, W., Ahmed, S., Mallouk, T. E. & Sen, A. Small power: Autonomous nano- and micromotors propelled by self-generated gradients. *Nano Today* **8**, 531–534 (2013).
3. Ebbens, S. J. & Howse, J. R. In pursuit of propulsion at the nanoscale. *Soft Matter* **6**, 726 (2010).
4. Howse, J. R., Jones, R. A. L., Ryan, A. J., Gough, T., Vafabakhsh, R. & Golestanian, R. Self-Motile Colloidal Particles: From Directed Propulsion to Random Walk. *Phys. Rev. Lett.* **99**, 048102 (2007).
5. Gibbs, J. G. & Zhao, Y.-P. Autonomously motile catalytic nanomotors by bubble propulsion. *Appl. Phys. Lett.* **94**, 163104 (2009).
6. Brown, A. & Poon, W. Ionic effects in self-propelled Pt-coated Janus swimmers. *Soft Matter* **10**, 12 (2014).
7. Sumino, Y., Magome, N., Hamada, T. & Yoshikawa, K. Self-running droplet: Emergence of regular motion from nonequilibrium noise. *Phys. Rev. Lett.* **94**, 1–4 (2005).
8. Yao, X. *et al.* Running droplet of interfacial chemical reaction flow. *Soft Matter* **8**, 5988 (2012).
9. Lauga, E. & Davis, A. M. J. Viscous Marangoni propulsion. *J. Fluid Mech.* **705**, 120–133 (2011).

10. Pimienta, V. & Antoine, C. Self-propulsion on liquid surfaces. *Curr. Opin. Colloid Interface Sci.* **19**, 290–299 (2014).
11. De Magistris, G. & Marenduzzo, D. An introduction to the physics of active matter. *Phys. A Stat. Mech. Its Appl.* **418**, 65–77 (2015).
12. Hatwalne, Y., Ramaswamy, S., Rao, M. & Simha, R. A. Rheology of Active-Particle Suspensions. *Phys. Rev. Lett.* **92**, 118101–1 (2004).
13. Ramaswamy, S. The Mechanics and Statistics of Active Matter. *Condensed Matter Physics*, **1**, 323–345 (2010).
14. Cates, M. E. & MacKintosh, F. C. Soft active matter. *Soft Matter* **7**, 3050 (2012).
15. Schweitzer, F. Brownian Agents and Active Particles. *Springer Series in Synergetics* (2003).
16. Shirai, Y., Osgood, A. J., Zhao, Y., Kelly, K. F. & Tour, J. M. Directional Control in Thermally Driven Single-Molecule Nanaocars. *Nano Letters* **5**, 2331–2334 (2005).
17. Paxton, W. F. *et al.* Catalytic nanomotors: autonomous movement of striped nanorods. *J. Am. Chem. Soc.* **126**, 13424–31 (2004).
18. Tierno, P., Albalat, R. & Sagues, F. Autonomously moving catalytic microellipsoids dynamically guided by external magnetic fields. *Small* **6**, 1749 (2010).
19. Kebes. Kinesin cartoon. <http://en.wikipedia.org/wiki/>
20. Bact. EscherichiaColi NIAID. [http://en.wikipedia.org/wiki/File:EscherichiaColi\\_NIAID.jpg/](http://en.wikipedia.org/wiki/File:EscherichiaColi_NIAID.jpg/)
21. Purple snail. <http://life-sea.blogspot.fr/2011/10/life-of-sea-common-purple-snail.html>.
22. Bruno de Giusti. Schooling of fish. [https://en.wikipedia.org/wiki/Shoaling\\_and\\_schooling#/media/File:Moofushi\\_Kandu\\_fish.jpg](https://en.wikipedia.org/wiki/Shoaling_and_schooling#/media/File:Moofushi_Kandu_fish.jpg)
23. Kümmel, F. *et al.* Circular Motion of Asymmetric Self-Propelling Particles. *Phys. Rev. Lett.* **110**, 198302 (2013).
24. Buck, M. *et al.* Controlled Flight of a Biologically Inspired, Insect-Scale Robot. *Science* **340**, 603–607 (2013).
25. Elgeti, J., Winkler, R. G. & Gompper, G. Physics of microswimmers--single particle motion and collective behavior: a review. *Rep. Prog. Phys.* **78**, 056601 (2015).
26. Purcell, E. M.. Life at Low Reynolds Number. *American Journal of Physics*, **45**, 3–11 (1977).
27. Darnton, N. C., Turner, L., Rojevsky, S. & Berg, H. C. On torque and tumbling in swimming Escherichia coli. *J. Bacteriol.* **189**, 1756–64 (2007).

28. Berg, H. C. & Brown, D. a. Chemotaxis in Escherichia coli analyzed by three-dimensional tracking. *Nature* **239**, 500–504 (1972).
29. Angelani, L. Averaged run-and-tumble walks. *Europhysics Lett.* **102**, 20004 (2013).
30. Taktikos, J. Modeling the random walk and chemotaxis of bacteria : Aspects of biofilm formation. *Thesis* (2012).
31. Wang, Z., Chen, H. Y., Sheng, Y. J. & Tsao, H. K. Diffusion, sedimentation equilibrium, and harmonic trapping of run-and-tumble nanoswimmers. *Soft Matter* **10**, 3209–3217 (2014).
32. Ebbens, S., Jones, R. A. L., Ryan, A. J., Golestanian, R. & Howse, J. R. Self-assembled autonomous runners and tumblers. *Phys. Rev. E.* **82**, 015304 (2010).
33. Philipse, A. P. Notes on Brownian Motion. (2011).
34. Palacci, J., Cottin-Bizonne, C., Ybert, C. & Bocquet, L. Sedimentation and Effective Temperature of Active Colloidal Suspensions. *Phys. Rev. Lett.* **105**, 088304 (2010).
35. Ismagilov, R. F., Schwartz, A., Bowden, N. & Whitesides, G. M. Autonomous movement and self-assembly. *Angew. Chemie - Int. Ed.* **41**, 652–654 (2002).
36. Paxton, W. F., Sen, A. & Mallouk, T. E. Motility of catalytic nanoparticles through self-generated forces. *Chem. - A Eur. J.* **11**, 6462–6470 (2005).
37. Fournier-Bidoz, S., Arsenault, A. C., Manners, I. & Ozin, G. a. Synthetic self-propelled nanorotors. *Chem. Commun.* 441–443 (2005).
38. Paxton, W. F. Catalytic Nanomotors Autonomous Movement of Striped.pdf. *J. Am. Chem. Soc.* **126**, 13424 (2004).
39. Laocharoensuk, R., Burdick, J. & Wang, J. Carbon-nanotube-induced acceleration of catalytic nanomotors. *ACS Nano* **2**, 1069–1075 (2008).
40. Soler, L., Magdanz, V., Fomin, V. M., Sanchez, S. & Schmidt, O. G. Self-propelled micromotors for cleaning polluted water. *ACS Nano* **7**, 9611–20 (2013).
41. Pavlick, R. a., Sengupta, S., McFadden, T., Zhang, H. & Sen, A. A polymerization-powered motor. *Angew. Chemie - Int. Ed.* **50**, 9374–9377 (2011).
42. Mou, F. *et al.* Self-propelled micromotors driven by the magnesium-water reaction and their hemolytic properties. *Angew Chem Int Ed Engl* **52**, 7208–7212 (2013).
43. Wilson, D. A., Nolte, R. J. M. & van Hest, J. C. M. Autonomous movement of platinum-loaded stomatocytes. *Nat. Chem.* **4**, 268–274 (2012).
44. Archer, R. J., Campbell, a. I. & Ebbens, S. J. Glancing angle metal evaporation synthesis of catalytic swimming Janus colloids with well defined angular velocity. *Soft Matter* **11**, 6872–6880 (2015).



45. Hagen, B. *et al.* Gravitaxis of asymmetric self-propelled colloidal particles. *Nature Communications* **5**:4829 (2014).
46. Gibbs, J. G. & Zhao, Y. P. Design and characterization of rotational multicomponent catalytic nanomotors. *Small* **5**, 2304–2308 (2009).
47. Gibbs, J. G., Kothari, S., Saintillan, D. & Zhao, Y.-P. Geometrically designing the kinematic behavior of catalytic nanomotors. *Nano Lett.* **11**, 2543–50 (2011).
48. Volpe, G., Buttinoni, I., Vogt, D., Kümmerer, H.-J. & Bechinger, C. Microswimmers in patterned environments. *Soft Matter* **7**, 8810–8815 (2011).
49. Ghost, A. & Fischer, P. Controlled propulsion of artificial magnetic nanostructured propellers. *Nano Lett.* **9**, 2243–2245 (2009).
50. De Gennes, P. G. On Fluid/Wall Slippage. *Langmuir* **18**, 3413–3414 (2002).
51. Anderson, J. Colloid Transport By Interfacial Forces. *Annu. Rev. Fluid Mech.* **21**, 61–99 (1989).
52. Staffeld, P. O. & Quinn, J. a. Diffusion-induced banding of colloid particles via diffusiophoresis. *J. Colloid Interface Sci.* **130**, 88–100 (1989).
53. Golestanian, R., Liverpool, T. & Ajdari, A. Propulsion of a Molecular Machine by Asymmetric Distribution of Reaction Products. *Phys. Rev. Lett.* **94**, 1–4 (2005).
54. Golestanian, R., Liverpool, T. B. & Ajdari, a. Designing phoretic micro- and nano-swimmers. *New J. Phys.* **9**, 1–8 (2007).
55. Ebbens, S., Tu, M.-H., Howse, J. & Golestanian, R. Size dependence of the propulsion velocity for catalytic Janus-sphere swimmers. *Phys. Rev. E* **85**, 020401 (2012).
56. Brown Poon W., A. Ionic effects in self-propelled Pt-coated Janus swimmers. *Soft Matter* **10**, 4016–4027 (2014).
57. Sánchez, S. & Pumera, M. Nanorobots: The Ultimate Wireless Self-Propelled Sensing and Actuating Devices. *Chem. - An Asian J.* **4**, 1402–1410 (2009).
58. Mei, Y., Solovev, A. a., Sanchez, S. & Schmidt, O. G. Rolled-up nanotech on polymers: from basic perception to self-propelled catalytic microengines. *Chem. Soc. Rev.* **40**, 2109–2119 (2011).
59. Sanchez, S. *et al.* The smallest man-made jet engine. *Chem. Rec.* **11**, 367–370 (2011).
60. Pinchasik, B. E., Mohwald, H. & Skirtach, A. G. Mimicking bubble use in nature: propulsion of Janus particles due to hydrophobic-hydrophilic interactions. *Small* **10**, 2670–2677 (2014).
61. Craig, V. S. J. Very small bubbles at surfaces—the nanobubble puzzle. *Soft Matter* **7**, 40–48 (2011).



62. Lohse, D. & Zhang, X. Surface nanobubbles and nanodroplets. *Rev. Mod. Phys.* **87**, 981–1035 (2015).
63. Lee, S. H. & Leal, L. G. Motion of a sphere in the presence of a plane interface. Part 2. An exact solution in bipolar co-ordinates. *J. Fluid Mech.* **93**, 705–726 (1979).
64. Lee, B. S. H., Chadwick, R. S. & Leal, L. G. Motion of a sphere in the presence of a plane interface. Part 1. An approximate solution by generalization of the method of Lorentz. *J. Fluid Mech.* **93**, 705–726 (1979).
65. Fischer, T. M., Dhar, P. & Heinig, P. The viscous drag of spheres and filaments moving in membranes or monolayers. *J. Fluid Mech.* **558**, 451–475 (2006).
66. Keh, H. J. & Chen, S. B. Electrophoresis of a colloidal sphere parallel to a dielectric plane. *J. Fluid Mech.* **194**, 377–390 (1988).
67. Uspal, W. E., Popescu, M. N., Dietrich, S. & Tasinkevych, M. Self-propulsion of a catalytically active particle near a planar wall: from reflection to sliding and hovering. *Soft Matter* **1**, 1–15 (2014).
68. Kaptay, G. Interfacial criteria for stabilization of liquid foams by solid particles. *Colloids Surfaces A Physicochem. Eng. Asp.* **230**, 67–80 (2003).
69. Bonn, D., Eggers, J., Indekeu, J., Meunier, J. & Rolley, E. Wetting and spreading. *Rev. Mod. Phys.* **81**, 739–805 (2009).
70. Pieranski, P. Two-dimensional interfacial colloidal crystals. *Phys. Rev. Lett.* **45**, 569–572 (1980).
71. Moulinet, S., Guthmann, C. & Rolley, E. Dissipation in the dynamics of a moving contact line: effect of the substrate disorder. *Eur. Phys. J. B - Condens. Matter* **37**, 127–136 (2004).
72. Blake, T. D. The physics of moving wetting lines. *J. Colloid Interface Sci.* **299**, 1–13 (2006).
73. Huh, C. & Scriven, L.. Hydrodynamic model of steady movement of a solid/liquid/fluid contact line. *J. Colloid Interface Sci.* **35**, 85–101 (1971).
74. Blake, T. & Haynes, J. Kinetics of liquid/liquid displacement. *J. Colloid Interface Sci.* **80**, 1–3 (1969).
75. Boniello, G. *et al.* Brownian diffusion of a partially wetted colloid. *Nat. Mater.* **14**, 908–911 (2015).
76. O'Neill, M. E., Ranger, K. B. & Brenner, H. Slip at the surface of a translating–rotating sphere bisected by a free surface bounding a semi-infinite viscous fluid: Removal of the contact-line singularity. *Phys. Fluids* **29**, 913–924 (1986).
77. Mano, N. & Heller, A. Bioelectrochemical propulsion. *J. Am. Chem. Soc.* **127**, 11574–5 (2005).

78. Dhar, P. *et al.* Autonomously moving nanorods at a viscous interface. *Nano Lett.* **6**, 66–72 (2006).
79. J. Perrin. Mouvement brownien et réalité moléculaire. *Annales de Chimie et de Physique*, **18**, 5–104 (1909).



## Chapter 2

## 2 Fabrication of Platinum-Silica Janus colloids and experimental methods

### Introduction

As described in the first chapter, catalytic Janus colloids have been widely studied as promising active systems. However, their behavior at liquid surfaces did not receive much attention yet. From an experimental point of view, the need of trapping Janus colloids at the liquid surface precluded the use of bi-metallic colloids which are more difficult to be trapped at the interface due to their high density.<sup>1,2</sup> For this reason, the polymer systems<sup>3,4</sup> or silica ( $\text{SiO}_2$ )<sup>5,6</sup> beads half-coated by thin metallic films of gold (Au), platinum (Pt) drew our attention. Moreover, considering the fact that the fuel will be only present in the subphase, we were interested in Janus colloids having both of their faces hydrophilic. Therefore, we chose the Pt- $\text{SiO}_2$  Janus colloids for our detailed investigation.

We employed two methods to prepare Pt- $\text{SiO}_2$  Janus colloids. We first used the metal sputtering deposition method which is a well-developed industrial technique for depositing a thin solid film onto a substrate<sup>7</sup> and has been previously applied to the preparation of spherical Janus colloids.<sup>8</sup> We also tried a chemical method of modifying the bare surface<sup>9,10,11,12,16</sup> of colloidal particles embedded in wax drops as in Pickering emulsions.<sup>13–15,16,17</sup> To monitor the different steps of Janus colloids preparation, optical microscopy and scanning electronic microscopy (SEM) were used.

For the measurement of the particle immersion depth at the water surface, we used two protocols: an in situ measurement by optical microscopy and an indirect method based on SEM after trapping the particle in gelled-water. Contact angles of some liquids with silica and Pt planar substrates were measured by imaging the drop profile. Protocols are described here and results will be present in the next chapter.

In addition to that, we used an airbrush setup to spray the colloidal water suspension to trap particles on the air-water interface. In this way, we avoided introducing any possible contaminants from the spreading solvents. The tracking of particles was achieved by video microscopy. Other tools such as image treatments and motion trajectory analysis will be also described in this chapter.

### 2.1 Preparation of Janus colloids

#### 2.1.1 Physical deposition

##### 2.1.1.1 Protocol

The fabrication process of Pt- $\text{SiO}_2$  Janus colloids following the procedure by Love et al.<sup>8</sup> is shown in Figure 2.1. Silica beads (purchased from Microparticles GmbH, radius  $R = 1.06 \pm 0.03$   $\mu\text{m}$ , zeta potential =  $-13$  mV) were cleaned by centrifugation/dilution cycles using Millipore

water. This deionized water was produced by a Millipore Milli-Q filtration system with a resistivity of 18 M $\Omega$ ·cm.

First, a monolayer of silica beads was prepared on a silicon wafer (diameter 10 cm) by drop-casting: drops of particle suspension at a concentration of 0.1 mg/mL were regularly deposited with a syringe (needle size, 0.40  $\times$  20 mm) onto silicon wafer to reach an average coverage of about 10%. Observation of the deposited particles (Figure 2.1 (A)) shows that the particles rather than being homogeneously dispersed are clusters of 4 to 30 particles. This is possibly due to the capillary forces during the evaporation of water.

Afterward, by using plasma bombarded metal sputtering (ALCATEL SCM 400 system), 10 nm thickness of Titanium and 20 nm Platinum were deposited onto the surface. Figure 2.1 (B) shows the same sample of particles on silicon wafer just after Pt deposition. The Pt-covered beads appear darker than bare silica beads (in Figure 2.1 (A)). Pt coated silica beads were freed from the silica wafer into Millipore water by 30 minutes' sonication. These Pt-SiO<sub>2</sub> Janus colloids were then cleaned and collected by centrifugation/dilution cycles using Millipore water. Figure 2.1 (C) shows the Janus colloids deposited on a glass slide. They display non-uniform gray levels which reveal the randomness of their orientation once deposited on the glass slide.

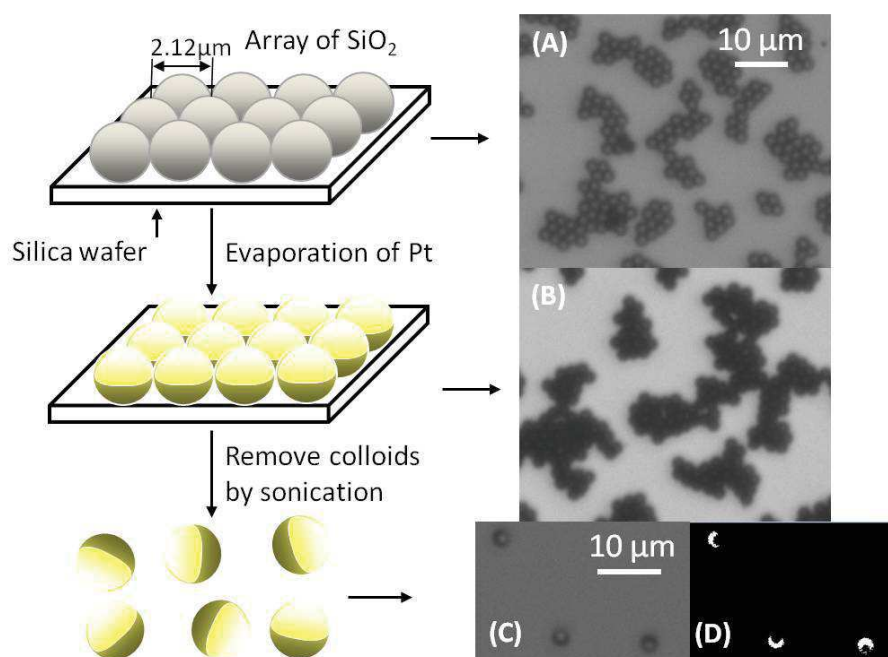


Figure 2.1 Left column: scheme showing fabrication of Janus colloids (yellow parts represent Pt). Right column: optical microscopy images of (A) SiO<sub>2</sub> beads, (B) Beads after Pt deposition and (C) Pt-SiO<sub>2</sub> Janus colloids (dark parts are Pt-coated) and (D) thresholded image corresponding to (C) with white crescents representing Pt-coated parts. The sample for (C) and (D) was prepared by depositing the Janus colloidal suspension onto a glass slide and then dried.

The difference of brightness between bare silica and the Pt-coated area is due to the different refractive indexes of platinum and silica. This difference will be exploited to characterize the orientation of the Janus colloid at the air-water interface. The image presented in Figure 2.1(D) has been obtained after a thresholding procedure which consists in replacing each pixel in an image with a black pixel if the gray level of the pixel is less than some threshold value, or a white pixel if the gray level of the pixel is greater than the threshold. This has been achieved by using *Image J* software. We also managed to use *IDL* software by implementing a routine in it. The use of microscopy and thresholding process provides a simple way to identify Pt-coated surface and further help to justify the orientation of Pt-cap during particle movement (see Section 2.3.4).

### 2.1.1.2 SEM and energy dispersive X-ray spectroscopy (EDXS) analysis of Janus particles

To get finer details on the deposited Pt layer, scanning electronic microscopy (SEM, FEI Quanta 200F) was used. In Figure 2.2, the Janus colloids show two distinct regions (Figure 2.2 (B, C)), compared to pure  $\text{SiO}_2$  beads (Figure 2.2 (A)). The bright parts correspond to Pt-covered regions. This is due to the fact that the SEM image is built from secondary electrons emitted by atoms which are excited by the electron beam and the intensity of secondary electron emission is higher for the material of higher atomic number.

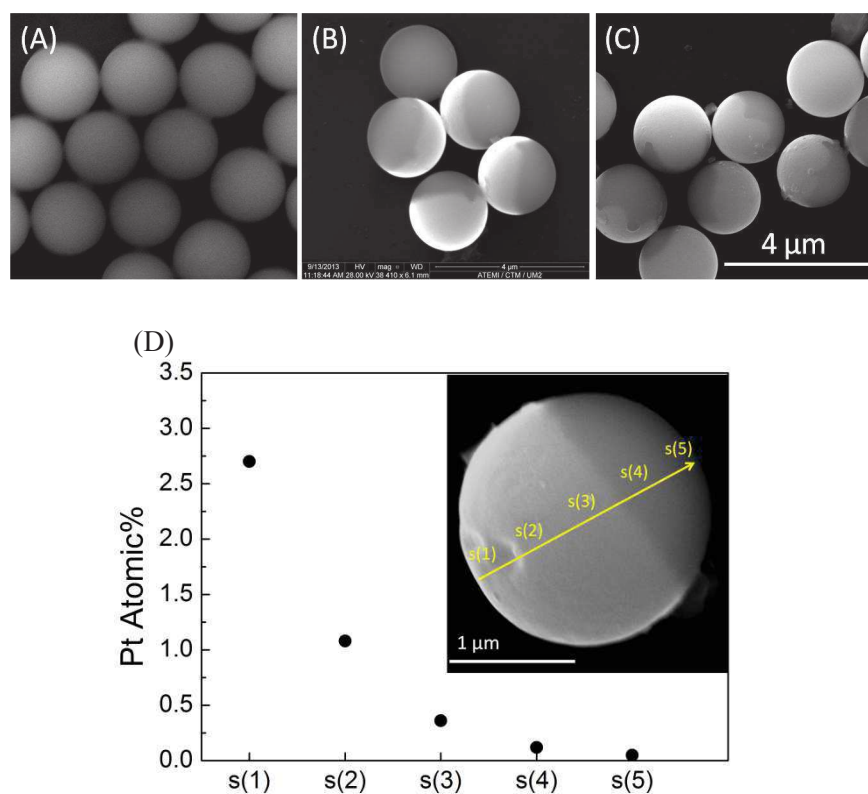


Figure 2.2 SEM images of (A)  $\text{SiO}_2$  beads, (B) and (C) Pt- $\text{SiO}_2$  Janus colloids with different Pt cap geometries and (D) Platinum atomic percentage measured by EDX spectroscopy on five different spots s(i) on the Janus colloid.

The Pt-coated region has been directly distinguished by EDXS (energy dispersive X-ray spectroscopy) which can analyze the elemental compositions of a specimen over a volume of  $1\mu\text{m}^3$  (cube). As shown by the inserted image in Figure 2.2 (D), we chose 5 different points along one meridian on the particle for chemical analysis. We see from Figure 2.2 (D) that the platinum content progressively decreased from 2.7% at s(1) to 0 at s(5). Negligible values are measured far from the white face of the colloid.

Looking into SEM images in Figure 2.2 (B) and Figure 2.2 (C), the Janus boundary where Pt-coated face and the bared silica face meet can be along the “latitude line” of the bead (see Figure 2.2 (B), (D)) or even can be “wavelike” (Figure 2.2 (C) and Figure 2.3 (A)). The morphology of Pt-coated surface exhibited in Figure 2.3 shows a grain size at about 10 nm scales which indicates significant surface nanoroughness. When metal atoms are deposited through electron beam sputtering onto a substrate which is rugged, the atoms do not arrive at the same time uniformly at the surface. This random fluctuation, which is inherent to the process, may create the surface roughness. It was also reported that in sputtered Au films, a peak in surface roughness of about 10 nm thickness has been observed<sup>18</sup>.

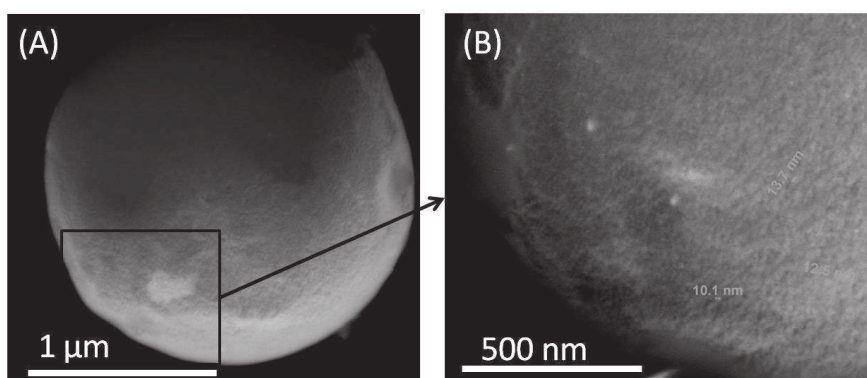


Figure 2.3 (A) SEM image of a Janus colloid with curved Pt surface boundary. (B) SEM image of a part of the Pt-coated surface showing Pt grains ( $\sim 10$  nm).

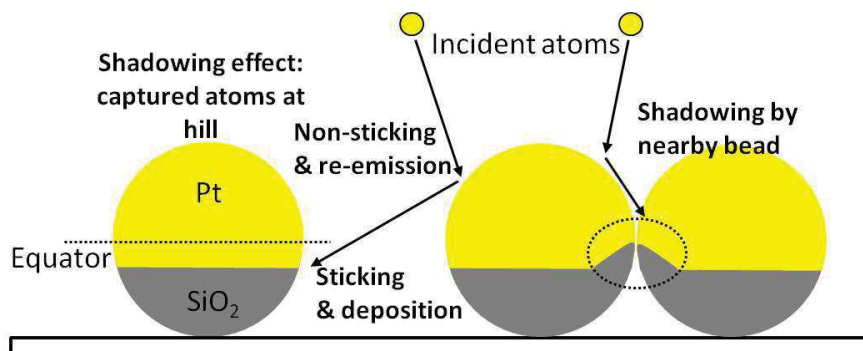


Figure 2.4 Proposed mechanism for the formation of the irregular Pt-coated surface.

The appearance of the wavelike Pt-cap boundary can be attributed to the shadowing, re-emission and additional nearby particle shadowing effects during the deposition of Pt. Shadowing can originate from obliquely incident Pt atoms being preferentially deposited on “hills” of the surface, which leads to a long range geometrical effect.<sup>19</sup> At the same time the bouncing non-sticking atoms can bounce off from hills and deposit on “valley”, and it is called re-emission effect.<sup>19</sup> As shown in Figure 2.4, when a bead is isolated the shadowing and re-emission effects introduce gradient of Pt layer thickness and also a more than half-coated Pt surface (Figure 2.2 (D)). In our experimental drop-casting process, the evaporation of water leads to aggregation of beads (“coffee ring” effect). When beads are close packed, the nearby bead will act as a “shield” preventing atoms from depositing to “valley” leading to the curved Pt-cap boundary (Figure 2.4).

## 2.1.2 Chemical deposition of Pt nanoparticles

### 2.1.2.1 From Pickering emulsions to colloidosomes

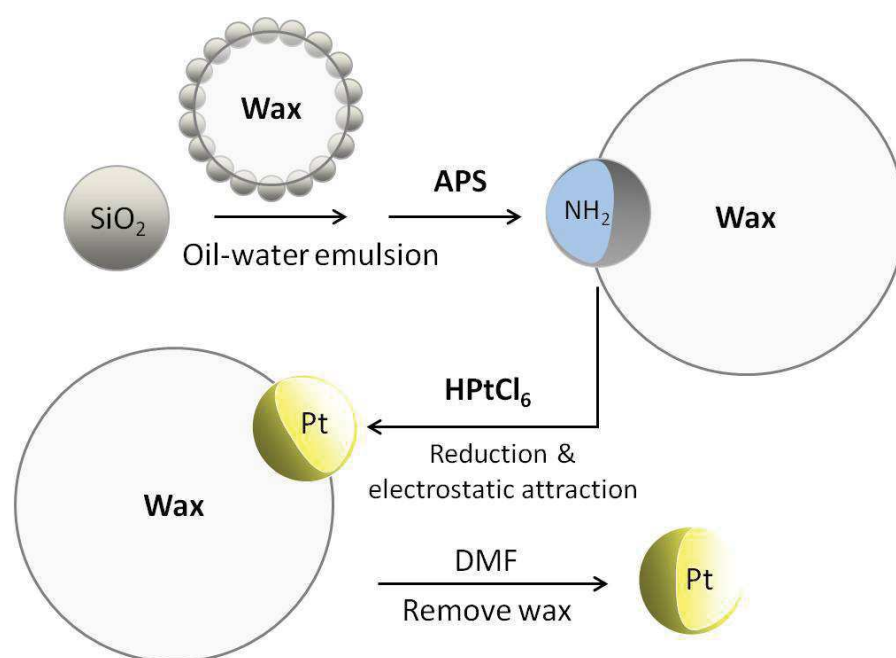


Figure 2.5 Schematic illustration of the fabrication of Pt-coated colloid.

The principle of Janus colloid preparation by metal vapor deposition relies on self-shadowing effect which allows protection of the face opposite from the metal electron beam. Another possibility is to protect a fraction of the particle area by embedding the particles into another medium before covering them with metal on the bared surfaces. One approach has been proposed by Granick et al. to produce Janus particles by a Pickering emulsion technique.<sup>13,16,17</sup> We further tried to develop a chemical way of preparing Pt- $\text{SiO}_2$  Janus particles, as schemed in Figure 2.5. The protocol relies on the formation of oil-water emulsions stabilized by the silica particles and subsequently chemical deposition of Pt onto the surface. The oil phase of the emulsion is the molten paraffin wax. The emulsion is fabricated at a temperature above the melting temperature



of the wax so that after cooling down the beads are “locked” and do not rotate during the chemical surface modification step. This ensures the formation of the asymmetric surface chemical composition of the particle.

Silica particles were cleaned by centrifugation/dilution cycles. The melting point of the paraffin wax ranges between 53°C ~ 57°C. The mass ratio of SiO<sub>2</sub>: paraffin is 1:17 expecting oil-in-water drops in the range of several hundred micrometers, assuming all the silica beads are trapped and close-packed at the wax interface

First the mixture of dried silica particles and paraffin wax was heated to 75°C and stirred for 15 minutes to achieve dispersion. Then hot Millipore water was added and continuously stirred (magnetic stirrer) at 1250 rpm/s for 2 hours to produce oil-water emulsions. The system was then quenched into a cold water bath to solidify the oil in water droplets. The solid wax particle decorated by silica particles is referred as “colloidosome” hereafter.

The colloidosomes suspension was washed several times with Millipore water to remove unattached beads. Colloidosomes floated at the water surface due to their large sizes and the lower density of paraffin wax while free particles settled down. After filtering, the colloidosomes were collected, then cleaned by anhydrous ethyl alcohol and finally dried in vacuum at room temperature.

We observed the colloidosome by optical microscopy (Figure 2.6) and SEM (Figure 2.7). From the optical microscope image of Figure 2.6 (A), we found the diameter of the colloidosomes range from 25 to 1800 μm. The large polydispersity may be due to the inhomogeneous stirring of the solution. Magnetic stirring was used with the rotating magnon at the bottom of the emulsions while the lighter melted wax tended to concentrate at the top, leading to non-homogenous stirring in the vial. The stirring speed near the surface of the solution was lower, resulting in larger emulsion size.

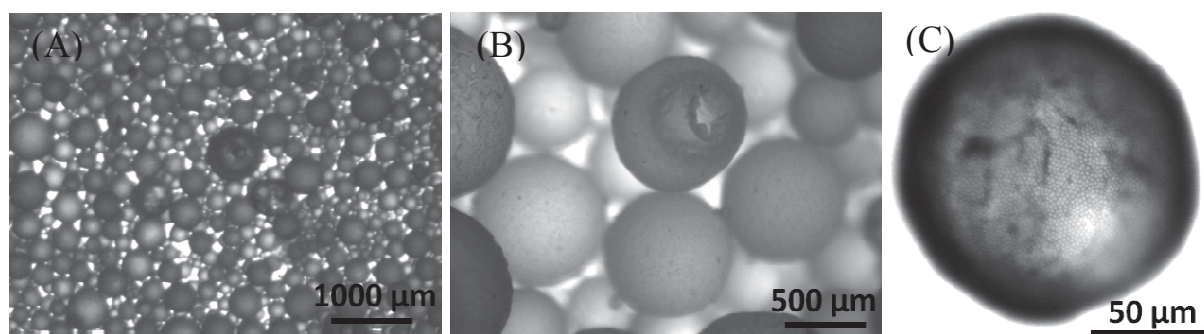


Figure 2.6 Images of SiO<sub>2</sub> embedded colloidosome: (A) macro photographic image and (B) microscopic image and (C) microscopic image showing embedded SiO<sub>2</sub> beads at the colloidosome surface.

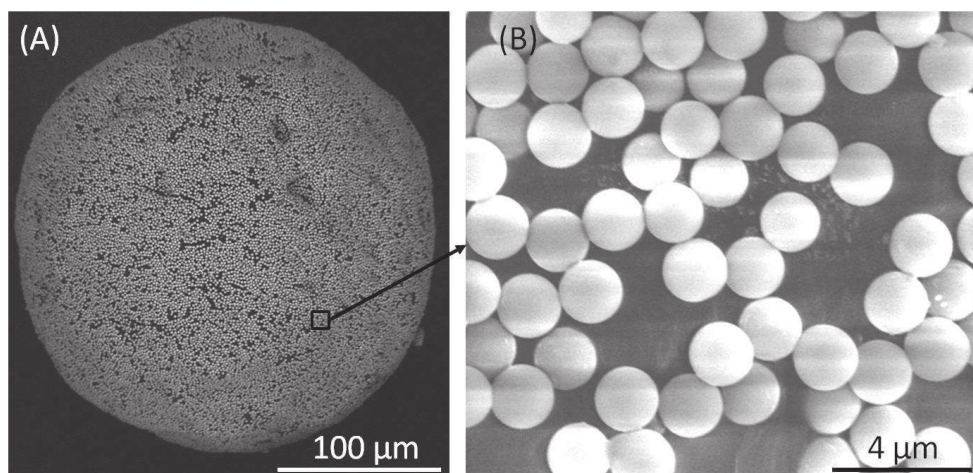


Figure 2.7 SEM images of colloidosome and particles embedded onto the wax surface. The striped particles in (B) result from image effect.

The optical microscopy image in Figure 2.6 (C) suggests a high coverage of the beads at the colloidosome surface, which is also confirmed by SEM analysis displayed in Figure 2.7. The colloidosome surface had a rough geometry with many dimples and the particles were embedded at different depths (Figure 2.7 (B)). This can be due to the overlay between nearby particles when the emulsion volume shrinks during solidification of paraffin wax. At the colloidosome surface, we didn't observe any "cave" formed by the leave of bead and the bead coverage keeps high. This indicates the absorption of beads onto the wax surface is quite stable which stands many times of washing and will be able to stand further chemical modification.

#### 2.1.2.2 Platinum loading

Platinum loading proceeds in two steps: first the silica surface exposed to the solvent is functionalized by amino groups which are known to be strong ligands for Pt. Then Pt seeds, prepared by reduction of chloroplatinic acid, are chemisorbed onto the functionalized silica surface.

The exposed surfaces of silica particles partially embedded at the colloidosome surface were reacted with 3-Aminopropyl trimethoxysilane (APS 99%, Sigma-Aldrich) in anhydrous ethyl alcohol for half an hour at room temperature. Triethylamine (>99%, Sigma-Aldrich) was added to speed up the reaction. The chemical reaction is shown in Figure 2.8. In this condition, the colloidosome is still solid and the beads are stuck in wax, therefore only exposed silica surface can be chemically modified. The reaction solution was then washed with anhydrous ethanol to remove the excess of silane.

The nanoparticles of Pt were synthesized first by citrate-reduction of  $\text{H}_2\text{PtCl}_6$ .  $\text{H}_2\text{PtCl}_6$  (chloroplatinic acid hexahydrate, ACS reagent >37.5% Pt basis, Sigma-Aldrich) water solution was refluxed in an oil bath heating at  $125^\circ\text{C}$  and then sodium citrate dehydrate ( $\geq 99\%$ , Sigma-Aldrich) was added. The molar ratio  $\text{H}_2\text{PtCl}_6$ : sodium citrate was 1:40. After reaction for 2 hours, the system was cooled down to room temperature to stop the reaction. The color of this solution turned from yellow to brown which illustrated the formation of Pt nanoparticles.

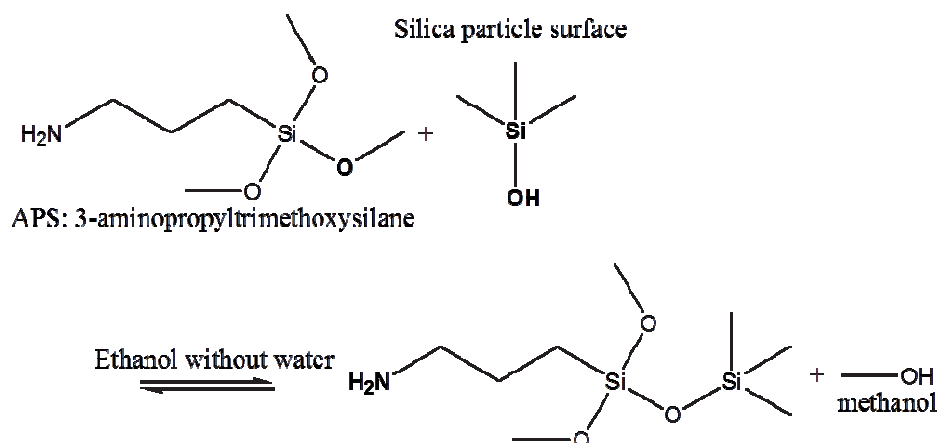


Figure 2.8 Chemical reaction between 3-Aminopropyl trimethoxysilane (APS) and exposed silica particle surface.

The suspension of nanoparticles of Pt was mixed with the colloidosomes and the temperature was increased up to 70°C to melt the colloidosomes for the purpose of better mixing with the seeds solution. Afterward, the system was stirred at 700 rpm/s for 1 hour. The system was then cooled down to room temperature and the paraffin wax solidified forming again the colloidosomes. The colloidosomes were washed using plenty of Millipore water to remove extra reactants and then collected and dried under vacuum at room temperature.

The presence of Pt at the surface of the colloidosome was demonstrated in the presence of  $\text{H}_2\text{O}_2$ . Many visible bubbles were produced at the surface of colloidosome (Figure 2.9) suggesting the catalytic activity of the colloidosome.

### 2.1.2.3 Colloidosomes at the air- $\text{H}_2\text{O}_2$ water solution interface

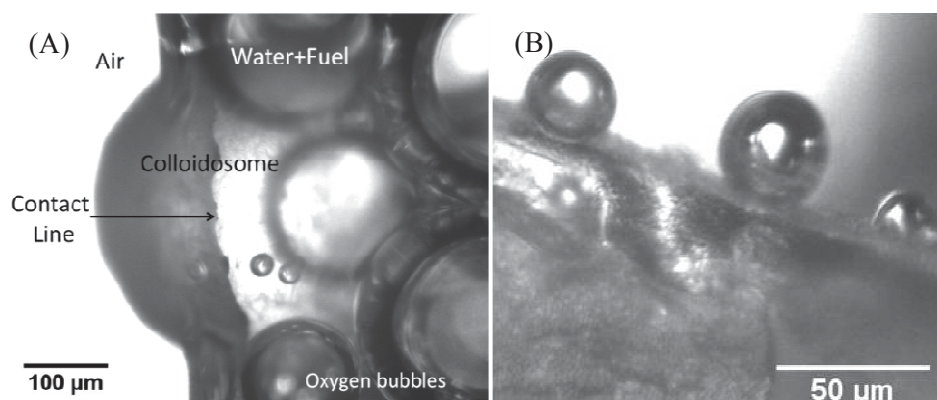


Figure 2.9 (A) Side view of Pt-topped colloidosome at air- $\text{H}_2\text{O}_2$  water solution interface ( $[\text{H}_2\text{O}_2]_v=28\%$ ). (B) Top view of the formation of oxygen bubbles at the surface of colloidosome.

To check the existence of Pt at the colloidosome surface, we deposited the colloidosome onto the surface of  $\text{H}_2\text{O}_2$  water solution. In the presence of Pt, the  $\text{H}_2\text{O}_2$  can be decomposed into water and oxygen (forming bubbles). Due to the lower density of colloidosome, it rested on the surface of the solution. Viewed by an optical microscopy, as shown in Figure 2.9 (A) (side view), many bubbles formed on the colloidosome surface immersed in the solution. Seen from the top (Figure 2.9 (B)), we found small bubbles of  $\sim 30\ \mu\text{m}$  in diameter at the three-phase contact line, which is  $\sim 15$  times large of the embedded bead (diameter  $2\ \mu\text{m}$ ). The formation of bubbles proves that Pt has been attached to the colloidosome surface.

#### 2.1.2.4 Unprotection: Release of beads from colloidosomes

Colloidosomes were dispersed in dimethylformamide (DMF) to remove paraffin wax. Released beads were cleaned by centrifugation/dilution cycles with Millipore water.

Pt loaded beads once released from the colloidosome were characterized by SEM and EDXS (Figure 2.10 (A)) in the same way as the Janus colloids prepared by monolayer sputtering (see Figure 2.2). A first important difference between Figure 2.2 and Figure 2.10 (A) is the absence of the white regions corresponding to the Pt-coated area. EDXS analysis (Figure 2.10 (B)) detects a relatively high percentage of Pt when it is in the form of a distinct particle: sampled area s(1) presents a nanometric particle and the atomic percentage of Pt is 3.11%. In all other sampled areas no significant amount of Pt could be detected by EDXS which meant that if any platinum is present it is in the form of a very thin layer.

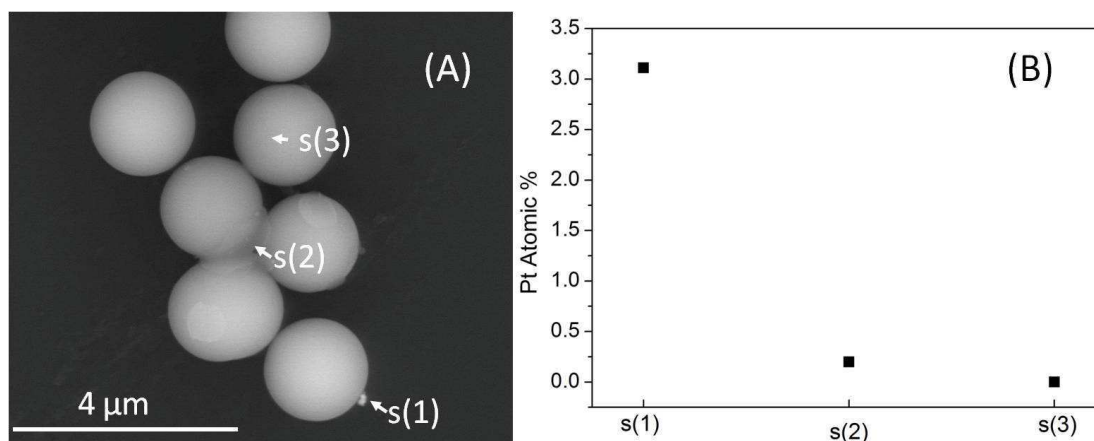


Figure 2.10 (A) SEM images of as fabricated Pt-SiO<sub>2</sub> beads at silicon wafer and (B) corresponding element atomic percentages at three points (each point analyzes  $1\ \mu\text{m}^2$  area).

We put the as-prepared Janus particles into  $\text{H}_2\text{O}_2$  water solutions and tracked the motion by optical video-microscopy, searching for self-propelled motion. However, there was no tendency for active motion even in the presence of high concentrations of  $\text{H}_2\text{O}_2$  and only Brownian motion was detected. This meant that the Pt layer fabricated by this chemical protocol is not able to produce enough propulsion.

On the basis of the former investigations, we can conclude that the colloidosome surface which bears the beads has been successfully loaded by Pt. Moreover, by cleaning with plenty of water, we believe there's no Pt seed stick to the free solid paraffin wax surface in between embedded beads except those doped inside. In addition to that, there's strong electrostatic attraction between Pt and the amino groups that have been anchored to silica bead surface: Pt nanoparticles have a preference to stick to the beads.

On the other hand, the failure of Pt detection by SEM and lack of active motion in the presence of  $\text{H}_2\text{O}_2$  fuel for isolated Janus colloids indicates that this chemical protocol should be further improved in the future. Hence, for the rest of the study, we have used the Janus particle prepared by physical sputtering deposition.

## 2.2 Characterization of the wetting properties

### 2.2.1 Contact angle measurements

#### 2.2.1.1 In situ measurement by optical microscope

For the study of particles at the liquid surface, it is important to know their wettability. The immersion of colloids at air-water interface was measured by an in situ method as described by Hórvölgyi *et al.*<sup>20</sup> A suspension of colloids in water was placed in between two parallel optical microscopic slides (Figure 2.11). The slides were spaced by large beads (silica beads of diameter  $4\ \mu\text{m}$ , purchased from Microparticles GmbH). Some of the targeted colloids were attached to the interface through capillary force. The sample cell was placed under an inverted microscope (equipped with Leica objective of  $\times 32$  magnification). Then the interfacial particles were focused and imaged from the bottom, as shown in Figure 2.11.

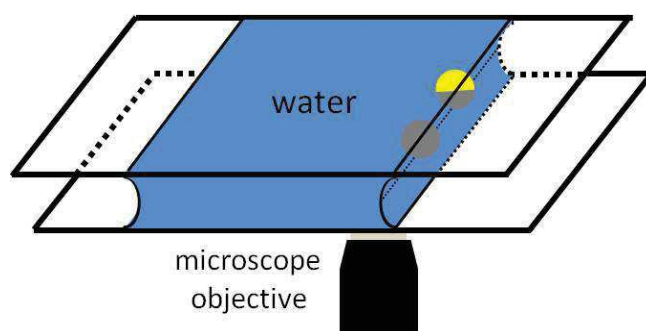


Figure 2.11 Homemade cell constructed by spaced glass slides for the measurement of the contact angle of beads at the air-water interface.

A representative image of a particle at the air-water interface is shown in Figure 2.12 (A). To get a clear feature of the particle, we adjusted brightness/contrast parameters and the improved image was presented in Figure 2.12 (B). We evaluated the contact angle  $\alpha$  of the particle from the image by using the “Contact Angle” plug-in in *Image J*.<sup>21</sup>



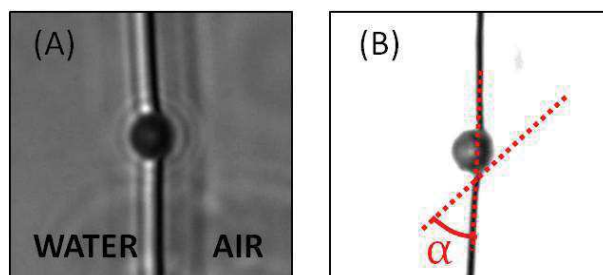


Figure 2.12 Measurement of contact angle from the image by using *Image J*. (A) Original image of a bead straddling the air-water interface. (B) Improved image after adjusting brightness/contrast. Contact angle  $\alpha$  is determined by using plug-in “Contact Angle” in *Image J*. The focal plane was chosen when the contact line and the particle profile were both focused the best.

### 2.2.1.2 Gel trapping method

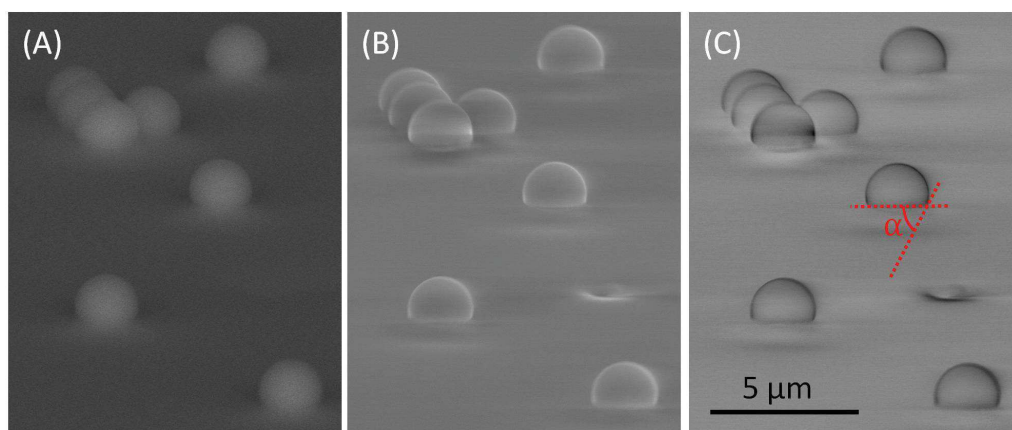


Figure 2.13 (A) SEM image of beads trapped in polymerized NOA81 layer, obtained by Backscattered Electron Detector. The visible parts of beads were previously immersed in gelled water. (B) SEM image obtained by Large Field Detector. (C) “Invert” treatment of image in (B) by *Image J* to improve the image profile of trapped beads for the following measurement of contact angle.

Another indirect contact angle measurement of colloids at the water surface is through a gel trapping method.<sup>22</sup> A 2 wt % Gellan (Phytigel, Sigma-Aldrich) solution in Millipore water was prepared by heating at 90°C under magnetic stirring. After cooling down to room temperature the gel was formed (gel point  $T = 27\text{--}32^\circ\text{C}$ ). Beads were spread at the gel surface and again heated at 90°C to be trapped at the interface. Immersion depth of beads at gelled water surface is expected to be very similar to the one at liquid water surface since the two interfaces have the same surface tension (72.8 mN/m).

To get a replica of the gel interface with the beads, Norland Optical Adhesive 81 (NOA81) was poured over the gelled water surface and then photopolymerized by ultraviolet light for 2

minutes. The solidified NOA81 layer was peeled off taking particles at complementary positions with respect to that at air-gelled water interface. These samples were finally observed by both optical microscopy and Scanning Electron Microscopy.

In the SEM images shown in Figure 2.13, the visible part of the beads was previously trapped in gelled water. Figure 2.13 (A) is an SEM image obtained by Backscattered Electron Detector while Figure 2.13 (B) is by Large Field Detector. We treated the SEM image in Figure 2.13 (B) by using the “Invert” process in *Image J* to get clear profiles of visible beads for the following contact angle measurement. The contact angle  $\alpha$  between the particle and water can be calculated using the plug-in “Contact Angle” in *Image J*.

### 2.2.2 Contact angle of liquid at planar surface and interfacial tension measurement

Characterization of the wetting properties of the Janus colloids has been completed by contact angle measurements of various liquids with silica and Pt planar substrates using a profile analyzer tensiometer (PAT, Sinterface, Germany). The same setup was used to measure surface tensions.

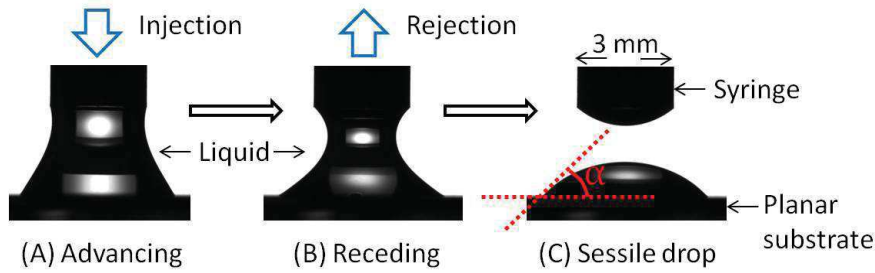


Figure 2.14 Schematic measurement of dynamic contact angles between liquid and a planar substrate. (A) Advancing contact angle measurement during liquid injection. (B) Receding contact angle measurement during pumping back liquid by syringe. (C) Residual drop formed after liquid rejection.

Static advancing and receding contact angles between a liquid drop and planar substrates have been measured during a liquid “injection-rejection” process, as presented in Figure 2.14 (A) and (B). The liquid was injected into or rejected from the drop step by step (liquid volume of each injection/rejection  $\sim 0.03 \mu\text{L}$ ) through an automatically controlled micro syringe ( $100 \mu\text{L}$ ). Each image of the drop was recorded by a camera between two injection or rejection steps. During injection, the contact line advanced leading to an advancing contact angle  $\alpha_A$  (Figure 1.4 (A)). When the liquid was pumped back to the syringe, the drop withdrew giving a receding contact angle  $\alpha_R$ . Further rejecting liquid the drop broke at the neck and a residual drop remained on the substrate (Figure 2.14 (C)). After recording the image, we can further measure the contact angle using *Image J*.

Liquid interfacial tensions have been measured by the same setup (PAT, Sinterface, Germany). As sketched by the image in Figure 2.15, a pendant drop is formed by injecting liquid from the top using a syringe. By detecting and analyzing the drop profile, interfacial tensions can be

measured. The software calculates the drop curvatures from the image profile and calculates the interfacial tension in the Laplace equation accounting for the gravity force. Figure 2.15 shows the air-water (Millipore water) interfacial tension as a function of time after the formation of pendant drop. The interfacial tension gives an average value of  $72.8 \pm 0.2$  mN/m. Note that there's a decay of surface tension in the time scale of measurement (2.8 hours) but it is very small (0.5 mN/m).

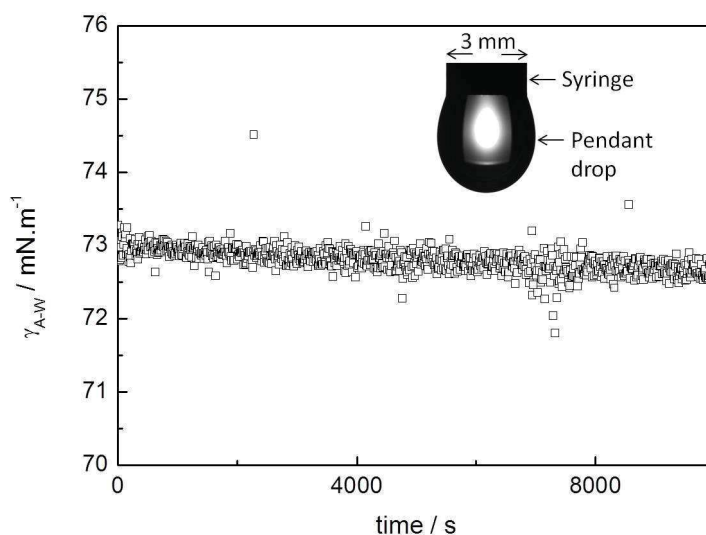


Figure 2.15 Air-water interfacial tension as a function of time. The inset image shows the pendant drop analyzed by PAT tensiometer.

## 2.3 Studying the motion of colloids at the air-water interface

### 2.3.1 Trapping of colloids at the water surface

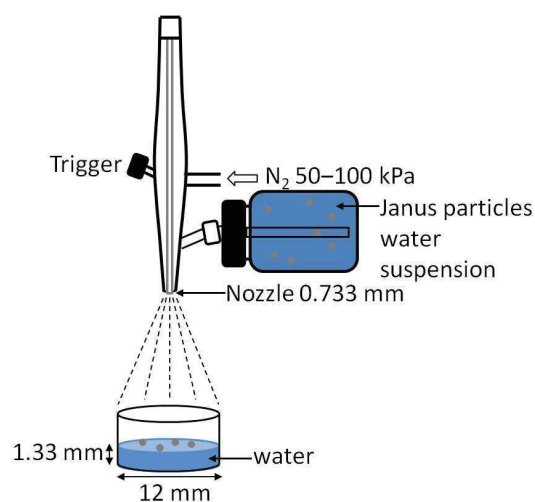


Figure 2.16 Scheme for depositing particles onto air-water interface by airbrush spraying.



Figure 2.16 displays the deposition of Pt-coated Janus colloids onto the air-water interface by using an airbrush. A water suspension of Janus particles was sprayed from about 70 cm distance onto the water surface in a small glass container (1.1 cm<sup>2</sup> area) by using an airbrush with a 0.733 mm nozzle operating at a pressure of 50-100 kPa. By using a colloid suspension in water the possible surface contamination of organic spreading solvent is avoided. The depth of the water subphase was set at 1.3 mm to minimize the drift at the water surface due to convection. We aimed at getting isolated particles at the interface and an approximate density of 50 particles mm<sup>-2</sup> (surface coverage 0.016%) was obtained. This interfacial density corresponds to a very dilute regime where interactions between colloids can be neglected.

### 2.3.2 Particle tracking methods

Tracking of isolated particles was achieved by using a Basler Scout CCD camera equipped Leica inverted microscope mounted on a Melles Griot optical table and two Leica objectives ( $\times 10$  and  $\times 32$ ). Two types of videos (1024  $\times$  768 pixels) with different fields of view approximately 477  $\mu\text{m} \times 358 \mu\text{m}$  and 125  $\mu\text{m} \times 94 \mu\text{m}$  were recorded at a rate of 30 frames per second. Videos obtained with the large field of view help to improve the statistics of the data analysis. Whereas, videos obtained at higher magnification brings details on the orientation and rotation of the Janus particles.

The tracking was performed under Labview (National Instruments) using an image correlation-based approach in order to obtain particle position over time [time  $t$  (s),  $x$  ( $\mu\text{m}$ ),  $y$  ( $\mu\text{m}$ )]. The software “Stat Tracker St. Andrews” developed by Graham Milne on LabView<sup>23</sup> was used to determine the position of the particles in each frame of the video at a subpixel resolution. At low magnification ( $\times 10$ ), the size of a pixel is 0.466  $\mu\text{m}$  and the position of 2  $\mu\text{m}$  diameter bead can be determined within 50 nm.

Particles were tracked first in the absence of H<sub>2</sub>O<sub>2</sub>. Only when particles underwent typical thermal Brownian motion showing negligible drift, we continued the experiments. Afterward, hydrogen peroxide solution was added to water using a microsyringe (10  $\mu\text{L}$ ) up to the desired H<sub>2</sub>O<sub>2</sub> concentration. Video recording started about 40 minutes after fuel injection. We used an aqueous solution of H<sub>2</sub>O<sub>2</sub> (30 wt%, Sigma- Aldrich) and added the solution drop by drop into the system by using a microsyringe at different places. A cover is also used to close the container and limit exchange with the atmosphere. Under this condition, H<sub>2</sub>O<sub>2</sub> is well dissolved in the liquid phase given the high self-diffusion coefficient<sup>24</sup> of H<sub>2</sub>O<sub>2</sub> and the relatively high concentration given by the addition of the H<sub>2</sub>O<sub>2</sub> solution. To rule out any possible effect of the inhomogeneous distribution of H<sub>2</sub>O<sub>2</sub>, we also performed a few experiments where we first prepared the solution at a given H<sub>2</sub>O<sub>2</sub> concentration and then sprayed the particles. Those results agreed with the ones obtained by adding H<sub>2</sub>O<sub>2</sub> solution drop by drop after spraying of the particles.

We monitored the motion of the Janus colloids over time. The motion keeps the same during the recording of videos in 3 hours. In fact, the concentration of H<sub>2</sub>O<sub>2</sub> is hardly affected during the measurement. This is due to the fact that the interfacial regimes are extremely diluted with few particles populating the interface and the amount of particles in the bulk are negligible, resulting in a small consumption of H<sub>2</sub>O<sub>2</sub>.

### 2.3.3 Pt-cap orientation from image treatments

By performing image analysis, the Pt-cap of some swimming Janus colloids at water surface can also be detected, as represented in Figure 2.17. As for the images of Janus particles on solid substrates (see Figure 2.1), the Pt-cap at the air-water interface can be detected after inputting a threshold to the raw image sequences using *IDL* program. In Figure 2.17 (B), Pt-cap is represented by the crescents of white pixels.

We are able to detect the Pt-cap from image analysis, and then its orientation can be characterized, as schematized in Figure 2.17 (C). Here  $(x_0, y_0)$  in the Cartesian is the center of the colloid while  $(x_1, y_1)$  is the center of detected Pt-cap (yellow semicircle). The orientation of Pt surface can be described by an angle  $\varphi$  which is given by  $\varphi = \arctan \frac{y_0 - y_1}{x_0 - x_1}$ . Here  $\varphi$  represent the angle between Pt-cap orientation (red dotted arrow in Figure 2.17 (B) and (C)) and the  $x$ -axis in the laboratory coordinate system. In this way we can calculate and follow the orientation during particle movement.

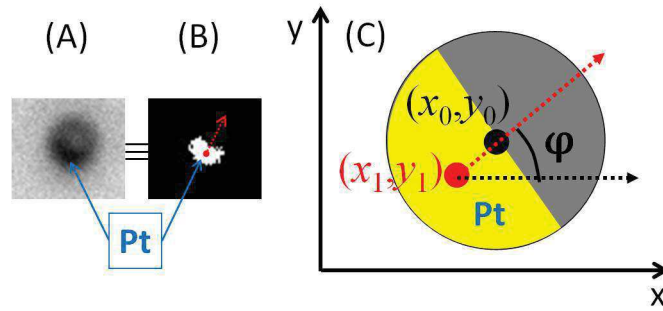


Figure 2.17 (A) Raw image of Janus colloid from which the position  $(x_0, y_0)$  of the center of the whole particle is determined. (B) Thresholded image from which the position  $(x_1, y_1)$  of the center of the platinum coated area is determined. (C) Orientation of the Janus particle is expressed by the angle  $\varphi = \arctan \left( \frac{y_0 - y_1}{x_0 - x_1} \right)$ .

### 2.3.4 Trajectory analysis

The motion of active Janus colloids was studied by single particle tracking method. Numerous observations of the motion of the individual particles must be analyzed statistically to get the appropriate time-averaged properties of the motion.

The translational motion has been characterized by the mean squared displacement (*MSD*) and the velocity autocorrelation function (*VACF*).<sup>25</sup> The *VACF* is half of the second time derivative of the *MSD*.<sup>25</sup> They both contain the same information regarding the motion of the particle. The characteristic parameters of the motion such as the active velocity and the diffusion coefficient are obtained by fitting *MSD* and *VACF* to the relation established from the models (see Chapter 1, Equation 1.12 and 1.13) so that an estimate of statistical accuracy for *MSD* and *VACF* is important.

Independent on the precision of the measurements for the particle position, both *MSD* and *VACF* have statistical variances that are inversely related to the number of observations made. Particle positions are recorded as time sequences  $\mathbf{r}_i = (x_i, y_i)$ , where  $0 \leq i \leq N - 1$ .  $N$  is the number of frames in the video. From the time sequences of positions, we deduce the mean displacement or the mean square displacements over lag times  $\Delta t = n\delta t$  (where  $\delta t$  is the lag time between two consecutive frames):

$$\langle \Delta \mathbf{r}(\Delta t) \rangle = \frac{1}{N-n} \sum_{i=0}^{N-1-n} (\mathbf{r}_{n+i} - \mathbf{r}_n) \quad 2.1$$

$$MSD = \langle \Delta^2 \mathbf{r}(\Delta t) \rangle = \frac{1}{N-n} \sum_{i=0}^{N-1-n} (\mathbf{r}_{n+i} - \mathbf{r}_n)^2 \quad 2.2$$

From the time sequences of positions, we also deduced a time sequence of velocity vectors

$$\mathbf{v}_i = \frac{\Delta \mathbf{r}_i(\delta t)}{\delta t} = \frac{\mathbf{r}_{i+1} - \mathbf{r}_i}{\delta t} \quad 2.3$$

$$[v_{xi}, v_{yi}] = \left[ \frac{(x_{i+1} - x_i)}{\delta t}, \frac{(y_{i+1} - y_i)}{\delta t} \right] \quad 2.4$$

The modulus of the velocity vector is the average speed over the image acquisition time  $\delta t$ .

From the time sequence of velocity vector the *VACF* is computed:

$$VACF = \langle \mathbf{v}(\Delta t) \cdot \mathbf{v}(0) \rangle = \frac{1}{N-1-n} \sum_{i=0}^{N-2-n} \mathbf{v}_{n+i} \cdot \mathbf{v}_i \quad 2.5$$

$$VACF = \frac{1}{N-1-n} \sum_i \langle v_{x\ n+i} \cdot v_{x\ i} \rangle + \langle v_{y\ n+i} \cdot v_{y\ i} \rangle \quad 2.6$$

To get an idea of the statistical errors made on *MSD* and *VACF* we carried out simulations of active particles of  $R=1.06 \mu\text{m}$  straddling at the water surface under the influence of an effective force of  $0.4 \text{ pN}$  and at room temperature. The translational diffusion coefficient is  $D_T = 0.218 \mu\text{m}^2/\text{s}$  and the rotational one is  $D_R = 0.164 \text{ s}^{-1}$ . The active speed is  $V = 21.2 \mu\text{m}/\text{s}$ . The lag time between consecutively recorded positions is  $1/30 \text{ s}$  and the short simulations correspond to the total time of  $33\text{s}$ .

Five simulations have been carried out with 1000 positions. *MSD* and *VACF* obtained from these simulations are plotted versus lag time  $\Delta t$  in Figure 2.18. The *MSD* and *VACF* obtained from the simulation are compared to the theoretically expected *MSD* and *VACF* (in black) calculated from Equation 1.12 in Chapter 1.

The statistical error made on estimating *MSD* has been calculated according to ref. [25] and is represented in Figure 2.18 as gray error bars around the expected value. The *MSD* values obtained from the simulations fall within the expected intervals. The calculation of the statistical error made on the *VACF* is more involved, but a grasp of the variability of the experimental result is given by the *VACFs* computed from the simulations. The simulated *VACFs* have been fitted to equation 1.12 (see Chapter 1) in order to extract the mean square active velocity  $\langle V^2 \rangle$  and the rotational diffusion coefficient  $D_R$ . Figure 2.19 shows the average of the values (black symbols) as well as their standard deviation (red error bars) of the fitting parameters, as a function of the maximum lag time considered.

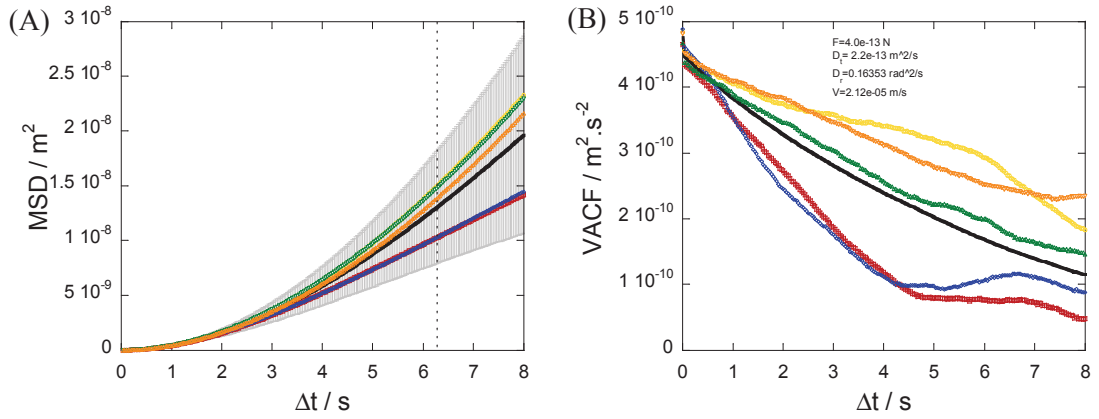


Figure 2.18 Statistical analysis of simulations of the active particle. (A) Mean squared displacement (B) Velocity autocorrelation function. Five independent simulations (colored symbols) for an active particle have been carried out with  $N=1000$  recorded positions.

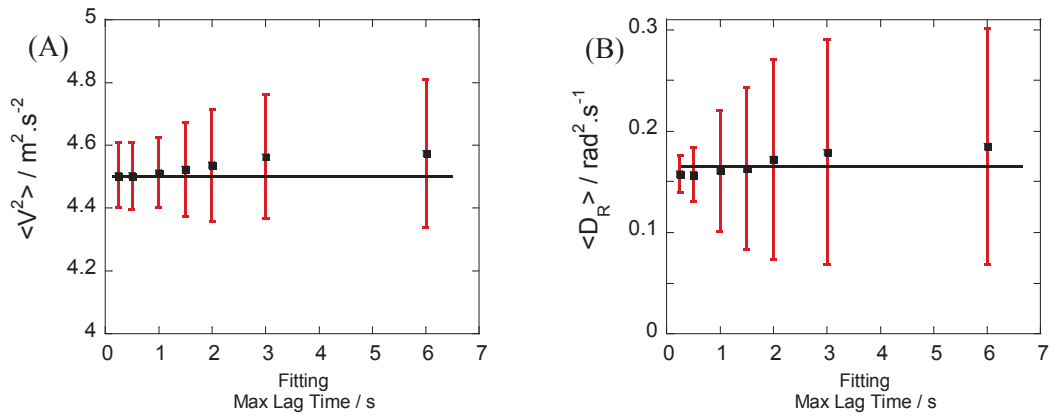


Figure 2.19 Average and standard deviation of the fitting parameters of the *VACF* of Figure 2.18 as a function of the maximum lag time considered. The black line is the true value. Black filled squares are the average values of the parameters and red bars are the standard deviation.

Figure 2.19 (A) and (B) show that the standard deviation increases as the maximum lag time increases. This means that the statistical error made on the characteristic parameters of the motion are lower when using few points from *MSD* and *VACF*. This statement has probably to be tempered by considering the error of measurement itself. But in any case, it is important to recall that the statistical accuracy cannot be judged by the smoothness of *MSD* and *VACF* and to keep in mind how fast the statistical error on the *MSD* and the *VACF* increases as the number of observations decreases.

## 2.4 Conclusions

In this chapter, we first reported two techniques of fabricating Pt-SiO<sub>2</sub> colloids. By using metal deposition, Pt-SiO<sub>2</sub> Janus colloids were successfully prepared. However, due to the shadowing and re-emission effects during Pt atom deposition, the prepared Pt-SiO<sub>2</sub> colloids appeared to have non-homogeneous Pt coated surface. More than a half of the particle surface area can be coated by Pt and the Janus boundary is often not straight but rather wavy. These effects should be taken into account in the following studies of active motion. Another Pickering emulsion technique was proposed. Unfortunately, we did not obtain a clear indication of successful fabrication. However, in the presence of fuel, colloidosomes showed catalytic property of releasing oxygen bubbles. This encouraged us to further improve our chemical preparation of Pt-SiO<sub>2</sub> colloids in the future. In this case, we used the Janus colloids prepared by the metal deposition method for the investigations.

The wetting and orientation of Janus colloids are crucial for the study of their active motions at the water surface. Contact angles of particles were measured by two methods: an in situ method by using microscopy and a gel trapping method using SEM. Interfacial surface tensions and contact angles between liquid and planar surfaces were obtained by a profile analyzer tensiometer. The detailed techniques were described in this chapter. In the next Chapter 3, these results will be presented and the energy landscapes of Janus colloids at the air-water interface will be also estimated.

## References

1. Kline, R. T., Paxton, F. W., Mallouk T. E. & Sen. A.. Catalytic nanomotors: Remote-controlled autonomous movement of striped metallic nanorods. *Angew. Chemie-International Ed.* **44**, 744–746 (2005).
2. Lluís, S., Vladimir M. F., Samuel S., & Oliver G. S.. Self-Propelled Micromotors for Cleaning Polluted Water. *ACS Nano* **7**, 9611–9620 (2013).
3. Howse, J. *et al.* Self-Motile Colloidal Particles: From Directed Propulsion to Random Walk. *Phys. Rev. Lett.* **99**, 048102 (2007).
4. Archer, R. J., Campbell, a. I. & Ebbens, S. J. Glancing angle metal evaporation synthesis of catalytic swimming Janus colloids with well defined angular velocity. *Soft Matter* **11**, 6872–6880 (2015).
5. Pavlick, R. A., Sengupta, S., McFadden, T., Zhang, H. & Sen, A.. A polymerization-powered motor. *Angew. Chemie - Int. Ed.* **50**, 9374–9377 (2011).
6. Gibbs, J. G. & Zhao, Y. P. Design and characterization of rotational multicomponent catalytic nanomotors. *Small* **5**, 2304–2308 (2009).
7. Vossen, J. L., Kern, W., E. Thin Film Processes II. *Acad. Press San Diego, CA* (1991).
8. Christopher L. J., Daniel B. Wolfe, Kateri E. Paul, George M. Whitesides, B. D. G. Fabrication and Wetting Properties of Metallic Half-Shells with Submicron Diameters. *Nano Lettres* **2**, 891 (2002).

9. Blaaderen, A. van, Imhof, A., Hage, W. & Vrij, A. Three-Dimensional Imaging of Submicrometer Colloidal Particles in Concentrated Suspension Using Confocal Scanning Laser Microscopy. *Langmuir* **8**, 1514–1517 (1992).
10. Jena, K. B. & Raj, C. R. Electrocatalytic Applications of Nanosized Pt Particles Self-Assembled on Sol-Gel-Derived Three-Dimensional Silicate Network. *J. Phys. Chem. C* **112**, 3496–3502 (2006).
11. Liu, J., Raveendran, P., Qin, G. & Ikushima, Y. Self-assembly of beta-D glucose-stabilized Pt nanocrystals into nanowire-like structures. *Chem Commun* 2972–2974 (2005).
12. Kim, M. R., Kim, J.-Y., Kim, S. J. & Jang, D.-J. Laser-induced fabrication of platinum nanoshells having enhanced catalytic and Raman properties. *Appl. Catal. A Gen.* **393**, 317–322 (2011).
13. Jiang, S., Schultz, M. J., Chen, Q., Moore, J. S. & Granick, S. Solvent-free synthesis of Janus colloidal particles. *Langmuir* **24**, 10073–10077 (2008).
14. Brun, M., Delample, M., Harte, E., Lecomte, S. & Leal-Calderon, F. Stabilization of air bubbles in oil by surfactant crystals: A route to produce air-in-oil foams and air-in-oil-in-water emulsions. *Food Res. Int.* **67**, 366–375 (2015).
15. Ichikawa, T. & Miura, M. Modified model of alkali-silica reaction. *Cem. Concr. Res.* **37**, 1291–1297 (2007).
16. Jiang, S. & Granick, S. Janus balance of amphiphilic colloidal particles. *J. Chem. Phys.* **127**, 161102(4) (2007).
17. Hong, L., Jiang, S. & Granick, S. Simple method to produce Janus colloidal particles in large quantity. *Langmuir* **22**, 9495–9499 (2006).
18. Kemmenoe, B. H. & Bullock, G. R. Structure analysis of sputter-coated and ion-beam sputter-coated films: a comparative study. *J. Microsc.* **132**, 153–163 (1983).
19. Karabacak, T. Thin-film growth dynamics with shadowing and re-emission effects. *J. Nanophotonics* **5**, 052501 (2011).
20. Z. Hórvölgyi J. H. Fendler, S. N. Spreading of silica beads at water-air interface. *Colloids Surf. A Physicochem. Eng. Asp.* **71**, 327 (1993).
21. Brugnara, M. Contact Angle. *Image J* (2006). <http://imagej.nih.gov/ij/plugins/contact-angle.html>
22. Paunov, V. N. Novel Method for Determining the Three-Phase Contact Angle of Colloid Particles Adsorbed at Air - Water and Oil - Water Interfaces. *Langmuir* **19**, 7970–7976 (2003).
23. Milne, G. Optical Sorting and Manipulation of Microscopic Particles Graham Milne Particles. *Thesis Ph.D.*, 1–184 (2007).

24. Van Stroe-Biezen, S. A. M., Everaerts, F. M., Janssen, L. J. J. & Tacke, R. a. Diffusion coefficients of oxygen, hydrogen peroxide and glucose in a hydrogel. *Anal. Chim. Acta* **273**, 553–560 (1993).
25. Qian, H., Sheetz, M. P. & Elson, E. L. Single particle tracking. Analysis of diffusion and flow in two-dimensional systems. *Biophys. J.* **60**, 910–921 (1991).

## Chapter 3

### 3 Wetting and orientation of Janus colloids at the surface of water

#### Introduction

Wetting plays a central role in the ability of a colloidal particle to carry out active motion at the water surface. First, the colloids must be partially immersed in the aqueous phase. Second, they must orient their catalytic face to be in contact with the fuel: no active motion would occur if the catalytic face was completely out of the fuel aqueous solution. Third, the Janus boundary must not lay parallel to the air-water interfacial plane in order to produce an effective propulsion force. Therefore, active motion can be carried out by Janus colloids at the interface, only in a particular range of orientation. The design of a double hydrophilic Janus colloid is requested to allow the catalytic face to react with the fuel and to permit some rotational freedom of the Janus colloid.

In this chapter, we consider the thermodynamics of the immersion depth and orientation of a Janus colloid at the surface of water. The dependence of the free energy of a colloid-interface system on the contact angle and on the orientation is derived. We also present contact angle measurements, observations of particle orientation at the interface and a quantitative analysis of the surface properties of the two distinct faces (silica and platinum) of the Janus colloid.

#### 3.1 Wetting property of colloids at the interface

##### 3.1.1 Theoretical description of a colloid trapped at the interface

###### 3.1.1.1 Bare colloid

We first consider a bare colloid with a uniform surface. When the surface of a colloid is in contact with both water and air simultaneously three phases are involved and this corresponds to partial wetting. Similar to a liquid drop at a planar solid substrate, an equilibrium contact angle ( $\alpha_{eq}$ ) can be defined. The Young-Laplace equation reads:<sup>1</sup>

$$\cos\alpha_{eq} = (\gamma_{S-A} - \gamma_{S-L}) / \gamma_{L-A} \quad 3.1$$

where  $\gamma_{S-L}$  (solid-liquid),  $\gamma_{L-A}$  (liquid-air) and  $\gamma_{S-A}$  (solid-air) are three different interfacial tensions acting on the triple line (where the three phases meet). At the equilibrium, the triple line does not move and the force on the line is zero due to the equilibrium of interfacial tensions. The Young Laplace equation describes this force balance tangential to the particle surface, see Figure 3.1.

The free energy associated with this equilibrium position can be calculated considering the free energy of the planar air-liquid interface and the surface energy of the bare colloid. If the colloid is immersed in the liquid, the free energy of the system in this state is:<sup>2</sup>

$$E_0 = A_S \gamma_{S-L} + A \gamma_{L-A} \quad 3.2$$

where  $A_S = 4\pi R^2$  is the area of the colloid and  $A$  is the area of the planar interface.



If the colloid is trapped at the interface at an equilibrium position  $-z = R \cos \alpha_{eq}$  ( $z = 0$  corresponds to the center of mass of the colloid and the  $z$ -axis is oriented from water to air, see Figure 3.1), the free energy becomes:

$$E_I = A_L \gamma_{S-L} + A_A \gamma_{S-A} + (A - A_0) \gamma_{L-A} \quad 3.3$$

where  $A_L = 2\pi R^2(1+\cos \alpha_{eq})$  is the area immersed of the particle in contact with the liquid,  $A_A = 2\pi R^2(1-\cos \alpha_{eq})$  is the area in the air and  $A_0 = \pi(R \sin \alpha_{eq})^2$  is the area of the cross-section of colloid at the air-water interface. The negative term  $-A_0 \gamma_{L-A}$  represents the energy loss associated with the reduction of the air-liquid interface area.

The work done by the capillary force that brings the colloid to its equilibrium position at interfaces is given by  $E_0 - E_I = \pi R^2 \gamma_{L-A} (1 - \cos \alpha_{eq})^2$  and the trapping of colloid at the air-water interface results in a reduction of the interfacial energy of the particle-interface system. This energy decrease depends on the contact angle and scales with  $R^2$ . For typical values:  $R = 1 \mu\text{m}$ ,  $\gamma_{L-A} = 72 \text{ mN/m}$  and  $\alpha_{eq} = 60^\circ$ , the energy is  $E_0 - E_I = 14 \times 10^6 kT$ . Once attached to the interface, a micron-sized colloid could not be displaced from the interface by thermal agitation energy<sup>2</sup> as  $kT \ll E_0 - E_I$ .

The contact angle dependence of the energy of the system that will be called thereafter the energy profile, reads:

$$E(\alpha) = E_I - A \gamma_{L-A} = 2\pi R^2 \left[ \gamma_{S-L}(1 + \cos \alpha) + \gamma_{S-A}(1 - \cos \alpha) - \frac{1}{2} \gamma_{L-A} \sin^2 \alpha \right] \quad 3.4$$

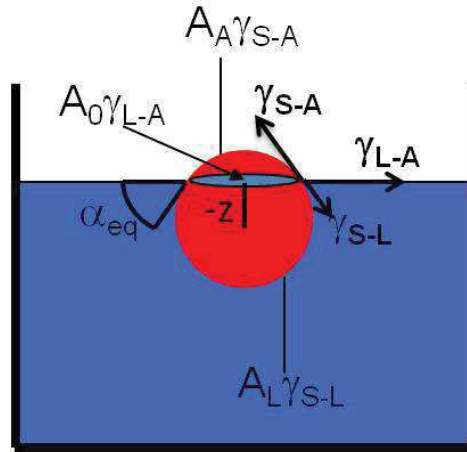


Figure 3.1 Sketch of a colloid at the air-liquid interface, partially immersed with a contact angle of  $\alpha_{eq}$ .  $z$  is the distance from the center of the colloid to the air-liquid interface. Three different interfacial tensions act on the contact line: solid-liquid ( $\gamma_{S-L}$ ), liquid-air ( $\gamma_{L-A}$ ) and solid-air ( $\gamma_{S-A}$ ).  $A_A$  is the area of colloid in air;  $A_0$  is area of the cross section of colloid at the interface and  $A_L$  is the area of colloid immersed in the liquid.

### 3.1.1.2 Janus colloid

Now we consider a Janus colloid at the interface, it can be anticipated that the contact angle dependence of the interfacial energy  $E(\alpha)$  will be modified because the two faces of the Janus particle possess different surface energies. The energy of an amphiphilic Janus particle at the fluid surface has been described by Ondaçuhu et al.,<sup>3</sup> under the assumptions that the interface is flat and the Janus boundary is parallel to the interfacial plane. The Janus boundary is the line where the two faces of the Janus colloid meet. Here we consider the case of Janus colloid with two distinct faces of equal area ( $2\pi R^2$ ) staying at the air-water (A-W) interface. The two faces are denoted as the hydrophilic face (HL) and the hydrophobic one (HB).

If  $\alpha > 90^\circ$ ,

$$E(\alpha) = 2\pi R^2 \left[ \gamma_{HB-A} + \gamma_{HL-A}(-\cos\alpha) + \gamma_{HL-W}(1 + \cos\alpha) - \frac{1}{2}\gamma_{W-A}\sin^2\alpha \right] \quad 3.5$$

If  $\alpha < 90^\circ$ ,

$$E(\alpha) = 2\pi R^2 \left[ \gamma_{HL-W} + \gamma_{HB-W}(\cos\alpha) + \gamma_{HB-A}(1 - \cos\alpha) - \frac{1}{2}\gamma_{W-A}\sin^2\alpha \right] \quad 3.6$$

The most stable configuration for a Janus particle at an hydrophilic-hydrophobic interface has been discussed by Casagrande *et al.*<sup>11</sup> They considered amphiphilic Janus particles with both faces of equal area possessing very distinct contact angles: the hydrophilic face (HL)  $\alpha_{HL} < 90^\circ$  and the hydrophobic one (HB)  $\alpha_{HB} > 90^\circ$ . In this configuration, the hydrophobic face is immersed in the hydrophobic medium, the hydrophilic face is immersed in the hydrophilic medium and the expected equilibrium contact angle is  $\alpha^* = 90^\circ$ . However, experimentally a distribution of contact angles was observed lying in between  $\alpha_{HL}$  to  $\alpha_{HB}$ .<sup>11</sup>

In the case of the platinum-silica Janus colloids at the air-water interface we investigate here, both faces prefer to be in contact with water. Contact angles of silica and platinum surfaces at air-water interface are smaller than  $90^\circ$  and such Janus colloid can be considered as a double hydrophilic Janus colloid. It will now be shown that double-hydrophilic Janus colloids at interface behave similarly as bare colloids. The energy profile  $E(\alpha)$  can be established once all the interfacial energy terms  $\gamma_i$  being determined.

## 3.1.2 Determination of the interfacial energy terms

The interfacial energy  $E(\alpha)$  involves terms of solid surface energies which are difficult to measure. It is generally determined indirectly from contact angle values and from Young-Laplace equation. This section reports on the contact angle values measured as described in Chapter 2, Section 2.2.1.

### 3.1.2.1 Contact angle of colloid at the water surface

*In situ contact angle measurement by optical microscopy*

The contact angle of Pt-SiO<sub>2</sub> Janus colloids at the air-water interface was first measured by optical microscopy. Representative images are shown in Figure 3.2. We measured 7 particles and calculated for each particle three times the contact angle from the water side and obtained the contact angle  $\alpha = 57.8 \pm 9.1^\circ$ . The dispersion of values is due to experimental error but might also be due to the contact angle hysteresis of the Janus particle (see Chapter 1, Section 1.5.2). To

limit the experimental error due to optical diffraction phenomena sensitive to focus we also used electron microscopy, but this required special conditioning of the sample.

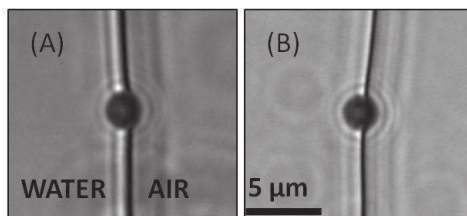


Figure 3.2 Representative microscopic images showing Janus colloids trapped at the air-water interface.

#### *Contact angle measured by electron microscopy after gel trapping*

As presented in Chapter 2, Section 2.2.1, a gel trapping method was used to measure the contact angles of bare silica beads and Janus colloids at the surface of the water. The resulting SEM images are shown in Figure 3.3. Note that the parts of beads visible were previously immersed in gelled water. We determined the contact angle from the images, averaging more than 20 beads and obtained  $\alpha = 70.9 \pm 3.6^\circ$  for bare silica colloids and  $\alpha = 63.6 \pm 2.2^\circ$  for Janus colloids. The latter value is higher than the contact angle value measured by optical microscopy (see Table 3.1), but both are consistent within experimental error. This difference may be due to the slightly different properties of gelled water (from water), the deposition protocol and the temperature at which the trapping occurs (see Chapter 2, Section 2.2.1).

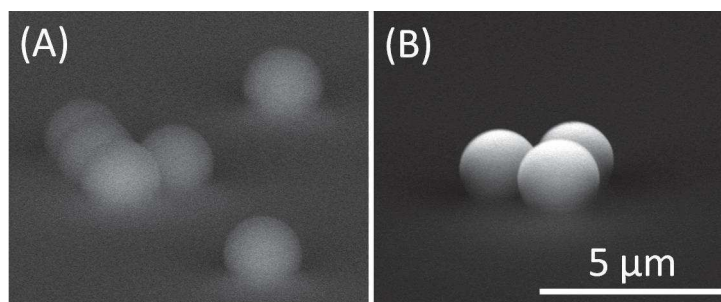


Figure 3.3 SEM images of (A) SiO<sub>2</sub> beads, (B) Janus Pt-SiO<sub>2</sub> beads trapped in polymerized NOA81 layers. The parts visible of the beads were previously immersed in gelled water.

#### **3.1.2.2 Liquid drop on planar solid substrate**

##### *Water drop contact angle*

We measured the contact angles of water drops on the planar silica and Pt-coated surfaces (see Chapter 1, Section 2.2.2). The Pt-coated planar surface was prepared the same way as that for

Janus colloids by using metal deposition method (see Chapter 2, Section 2.1.1). First 10 nm of titanium was deposited onto the silica wafer and then 20 nm platinum was deposited. Results are listed in Table 3.1. It shows that the advancing angle of water with the Pt-coated surface is slightly higher ( $59.1 \pm 1.3^\circ$ ) than with silica surface ( $56.9 \pm 1.0^\circ$ ) while the receding angles show the opposite trend.

| Contact angle     | Advancing ( $\alpha_A$ ) | Receding ( $\alpha_R$ ) | Gel-trapping         | Optical microscopy |
|-------------------|--------------------------|-------------------------|----------------------|--------------------|
| <b>Water-</b>     |                          |                         |                      |                    |
| Silica surface    | $56.9 \pm 1.0^\circ$     | $44.3 \pm 0.2^\circ$    | $70.9 \pm 3.6^\circ$ | --                 |
| Pt-coated surface | $59.1 \pm 1.3^\circ$     | $40.1 \pm 0.4^\circ$    | --                   | --                 |
| Janus colloid     | --                       | --                      | $63.6 \pm 2.2^\circ$ | $57.8 \pm 9^\circ$ |

Table 3.1 Contact angles of a water drop with silica surface and Pt-coated surface.

#### *Influence of $H_2O_2$ on the contact angle and surface tension*

In order to study the effects of the  $H_2O_2$  fuel concentration on the wetting property, we also measured the contact angle of 6%  $H_2O_2$  aqueous solution drops (the maximum volume percentage used in our experiments) on a planar silica surface. The contact angle  $48.73 \pm 3.45^\circ$  was measured, consistent with the average contact angle obtained with pure water (see Table 3.1).

The contact angle of 1%  $H_2O_2$  aqueous solution drop on the Pt-coated surface was also studied. Images are shown in Figure 3.4. The Pt layer catalyzes the decomposition of  $H_2O_2$  producing water and oxygen bubble inside the drop (Figure 3.4 (A)). The contact angle measured in this non-equilibrium condition is  $\alpha \approx 58.6^\circ$  which is close to the advancing contact angles of water on Pt surface (see Table 3.1). Once  $H_2O_2$  decomposition ended up (Figure 3.4 (B)), the remaining water drop shows a contact angle of  $\alpha \approx 39.5^\circ$  which is comparable to the receding contact angle of a water drop at Pt- surface ( $\alpha_R = 40.1 \pm 0.4^\circ$ , see Table 3.1).

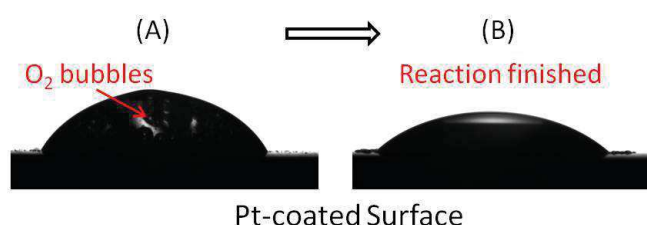


Figure 3.4 (A) A drop of 1%  $H_2O_2$  aqueous solution on the Pt-coated surface. Inside the drop, there are many oxygen bubbles (pointed by red arrow) formed from the decomposition of  $H_2O_2$  catalyzed by Pt layer. (B) The same drop after exhaustion of  $H_2O_2$ .

The surface tensions of the Millipore water ( $\gamma_{W-A}$ ) and the 6%  $H_2O_2$  aqueous solution ( $\gamma_{H_2O_2-A}$ ) were also measured to check the purity of the liquids, as described in Chapter 2, Section 2.2.2.  $\gamma_{W-A} = 72.80 \pm 0.19$  mN/m which agrees with the literature<sup>4</sup> and  $\gamma_{H_2O_2-A} = 70.77 \pm 0.39$  mN/m which is, somewhat, slightly smaller than the literature value.<sup>4</sup>

Hence, there is only a little difference in terms of wetting between pure water and low concentration  $H_2O_2$  solutions given the similar surface tension and contact angle results.

#### *Oil drop contact angle*

We also studied the wetting properties of heptane drops on silica and Pt-coated surfaces, in order to evaluate the surface energy of silica and platinum. Heptane drops wet completely both the silica and Pt-coated surfaces, see Figure 3.5. When the heptane drop touches the substrate, it immediately spreads ( $< 1$  s) leading to a contact angle  $\approx 0^\circ$  (see Figure 3.5).

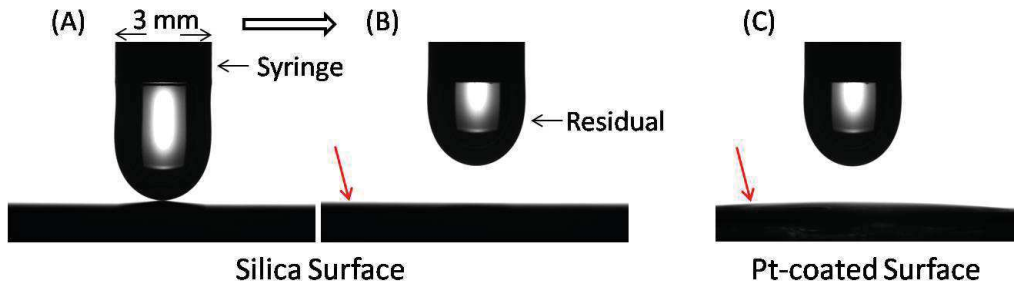


Figure 3.5 Complete wetting of heptane drops on silica and Pt-coated surfaces (arrows point to the spread drops).

### 3.1.3 Surface energy calculation of Platinum and Silica

From the contact angles measured, from the Young-Laplace equation and from some well-established empirical relations between dispersive and polar contributions to the solid surface energy, it is now possible to estimate the four different interfacial energy terms that appear in Equation 3.6 and to establish the energy profile  $E(\alpha)$  of Pt-SiO<sub>2</sub> Janus particle at the air-water interface. The results are summarized in Table 3.2.

The approach is the following and is applied first to the silica interfaces. From the Young-Laplace equation, we get the following relation between  $\gamma_{Si-A}$  and  $\gamma_{Si-W}$ :

$$\gamma_{Si-A} = \gamma_{Si-W} + \gamma_{W-A} \cos(\alpha_{Si,A-W}) \quad 3.7$$

The second relation is provided by the empirical geometric mean combining rules that relate the interfacial energy between two materials to the surface energy (when surface is in contact with vacuum) of each material and its various contributions:<sup>5</sup>

$$\gamma_{Si-W} = \gamma_{Si} + \gamma_W - 2\sqrt{\gamma_{Si}^d \gamma_W^d} - 2\sqrt{\gamma_{Si}^p \gamma_W^p} \quad 3.8$$

where  $\gamma_{Si}$  and  $\gamma_W$  are the surface energies of silica and water respectively. Recall that the surface energy of any material ( $i = \text{SiO}_2$  or Pt) can be written as the sum of dispersive  $\gamma_i^d$  and polar contributions  $\gamma_i^p$ :<sup>5</sup>

$$\gamma_i = \gamma_i^d + \gamma_i^p \quad 3.9$$

For non-polar media such as oils, only the dispersive term contributes to the surface energy. For instance, the surface energy of heptane will be estimated by its interfacial tension with air:  $\gamma_H \approx \gamma_{H-A} = 20.33 \pm 0.64$  mN/m, which is essentially accounted for by the dispersive term:  $\gamma_H^d = 19.8$  mN/m. For polar liquids like water the polar term could be higher than the dispersive term:  $\gamma_W \approx \gamma_{W-A} = 71.9$  mN/m,  $\gamma_W^d = 21.5$  mN/m and  $\gamma_W^p = 50.4$  mN/m.<sup>6</sup>

We measured  $\alpha_{Si,A-W} = 70.9 \pm 3.6^\circ$  by the gel trapping method and an advancing contact angle of water drop on silica  $\alpha_{Si,A-W} = 56.9 \pm 1.0^\circ$  (see Table 3.1). Our results are comparable with the contact angle reported by Binks<sup>6</sup>  $\alpha_{Si,A-W} = 64 \pm 3^\circ$ . For this silica surface  $\gamma_{Si} = 58.6$  mN/m and  $\gamma_{Si}^d = 52$  mN/m and  $\gamma_{Si}^p = 6.6$  mN/m. Then using these values in Equation 3.8, one calculates  $\gamma_{Si-W} = 25$  mN/m.

The  $\gamma_{Si-A}$  and  $\gamma_{Si-W}$  values obtained are consistent with our observation of complete wetting of the silica surface by heptane (see Figure 3.5 (B)) which involves that:

$$\gamma_{Si-A} > \gamma_{Si-H} + \gamma_{H-A} \quad 3.10$$

Where the interfacial energy between heptane and silica is obtained from:

$$\gamma_{Si-H} = \gamma_{Si-A} + \gamma_{H-A} - 2\sqrt{\gamma_{Si}^d \gamma_H^d} = 14 \text{ mN/m} \quad 3.11$$

The energies of the platinum surface can be estimated in the same way. Note that the pure and perfectly clean platinum surface should have a zero equilibrium contact angle with water.<sup>8</sup> However experimental equilibrium contact angle values lay between  $0^\circ$  and  $80^\circ$  because of aging and unavoidable contamination effects.<sup>9</sup> Here we compare our experimental results with the platinum surface energy reported by Leon et al.:  $\gamma_{Pt-A} = \gamma_{Pt}^d \approx 153$  mN/m and  $\gamma_{Pt}^p \approx 0$  mN/m.<sup>10</sup>

By using the combining rule we calculate the platinum-water interfacial tension:

$$\gamma_{Pt-W} = \gamma_{Pt-A} + \gamma_{W-A} - 2\sqrt{\gamma_{Pt}^d \gamma_W^d} = 110 \text{ mN/m} \quad 3.12$$

Using those values in the Young-Laplace equation, we find the contact angle of Pt with water is:

$$\alpha_{Pt,A-W} = \arccos\left(\frac{\gamma_{Pt-A} - \gamma_{Pt-W}}{\gamma_{W-A}}\right) = 54 \pm 3^\circ \quad 3.13$$

This is in fair agreement with the advancing contact angle  $\alpha_A = 59.1 \pm 1.3^\circ$  we measured for a water drop on the Pt-coated surface.

We can compare these results with the observation of complete wetting of heptane drop on the platinum surface, see Figure 3.5 (C). The calculated platinum-heptane surface energy is

$\gamma_{Pt-H} = \gamma_{Pt-A} + \gamma_{H-A} - 2\sqrt{\gamma_{Pt}^d \gamma_H^d} = 63 \text{ mN/m}$ . This value agrees with the complete wetting condition which reads:  $\gamma_{Pt-A} = 153 \text{ mN/m} > \gamma_{Pt-H} + \gamma_{H-A} = 82.5 \text{ mN/m}$ .

| Interfacial energy | Silica  | Platinum |
|--------------------|---------|----------|
| Water              | 25 mN/m | 110 mN/m |
| Air                | 59 mN/m | 153 mN/m |

Table 3.2 Interfacial energies of different materials.

### 3.1.4 Contact angle dependence of the free energy

The interfacial energies of silica and platinum experimentally estimated in the previous section have been introduced in Equation 3.5 and 3.6 to calculate the free energy profiles  $E(\alpha)$  when the Janus boundary is parallel to the water surface (shown in Figure 3.6). Two configurations are presented: the first one is the configuration describing the platinum face oriented towards the water and the second is the one with the platinum face oriented towards the air.

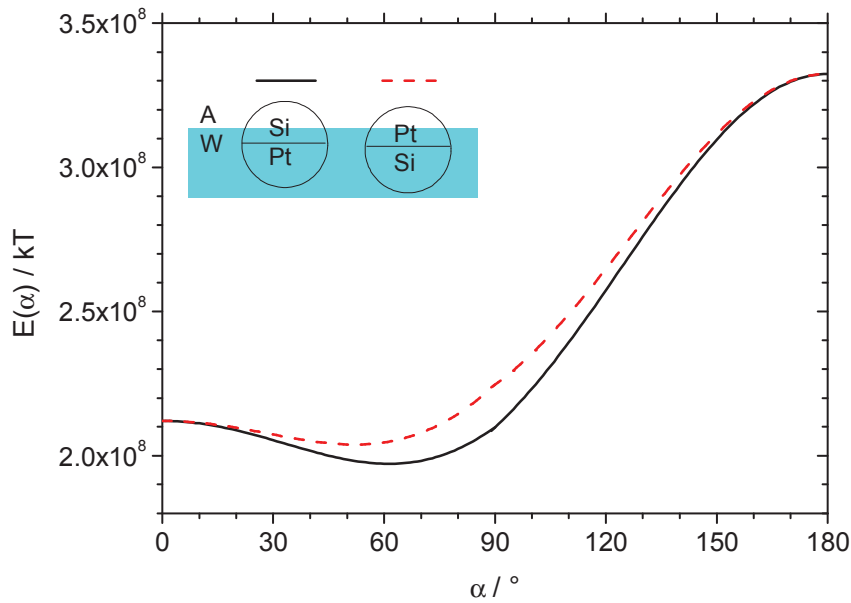


Figure 3.6 Energy profile as a function of contact angle  $\alpha$  under two conditions: (i) the platinum face oriented towards water (black line) and (ii) the platinum face oriented towards air (red dotted line). Here the energy profiles were calculated using Eqn. 3.5 and Eqn 3.6 by plugging in corresponding values:  $R=1 \text{ }\mu\text{m}$ ,  $\gamma_{W-A}=72 \text{ mN/m}$ , (1) black curve:  $\gamma_{HB-A} = \gamma_{Si-A} = 58.6 \text{ mN/m}$ ,  $\gamma_{HB-W} = \gamma_{Si-W} = 25 \text{ mN/m}$ ,  $\gamma_{HL-A} = \gamma_{Pt-A} = 153 \text{ mN/m}$ ,  $\gamma_{HL-W} = \gamma_{Pt-W} = 110 \text{ mN/m}$ ; (2) red curve:  $\gamma_{HB-A} = \gamma_{Pt-A}$ ,  $\gamma_{HB-W} = \gamma_{Pt-W}$ ,  $\gamma_{HL-A} = \gamma_{Si-A}$ ,  $\gamma_{HL-W} = \gamma_{Si-W}$ .



From Figure 3.6, the energy profile for colloid with the platinum face oriented towards the water is lower than that with the opposite orientation, whatever the contact angle. This is due to that the surface energy of platinum is higher than the one of silica and this favors the contact of platinum with the water. Because both faces are hydrophilic, the energy profiles of Pt-SiO<sub>2</sub> Janus colloids at air-water in both configurations are similar to bare platinum or bare silica particles.

## 3.2 Orientation of a Janus colloids at the air-water interface

### 3.2.1 Analytical expression of the interfacial energy as a function of orientation

Now we start to investigate the change of the free energy as a function of the orientation of Janus colloid allow the Janus boundary to be not parallel to the interface. Here the contact angle is fixed at  $\alpha_{eq}$  and is assumed to be the same along the triple line. The air-water interface is flat and both faces of the colloid have the same area ( $2\pi R^2$ ). The orientation is defined by the angle  $\beta$  between the z-axis normal to the water surface and the normal to the Janus boundary (gray arrow, Figure 3.7). In the following we will refer to the complementary angle  $90^\circ - \beta$ .

Note that in the literature the orientation dependence of the interfacial energy of Janus particles has been calculated numerically or using computer simulations.<sup>12–14</sup> An analytical expression will be derived in the next section.

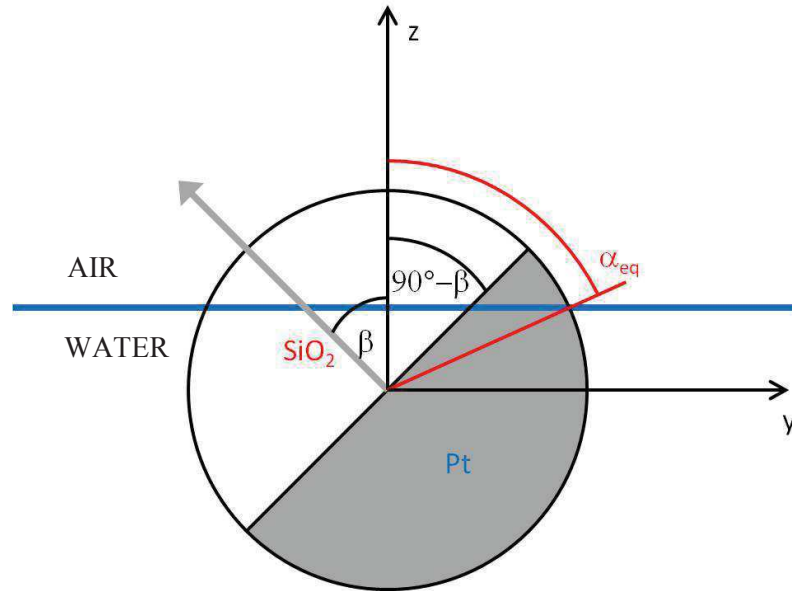


Figure 3.7 Schematic representation of Janus colloid at air-water interface with the Janus boundary normal (gray arrow) defining an angle  $\beta$  with z-axis.

In the range  $0 < 90^\circ - \beta < \alpha_{eq}$ , the free energy  $E(\beta) = E_I - \gamma A$  (see section 3.1) can be written as:

$$E(\beta) = \gamma_{Si-A} A_{Si-A} + \gamma_{Pt-A} A_{Pt-A} + \gamma_{Si-W} A_{Si-W} + \gamma_{Pt-W} A_{Pt-W} - \pi R^2 \gamma_{A-W} \sin^2 \alpha_{eq} \quad 3.14$$

where  $A_i$  are the area of silica or platinum in contact either with air or with water. The conservation of total area of the particle and conservation of the area of each Janus face yield:

$$A_{Si-A} + A_{Pt-A} = 2\pi R^2(1 - \cos \alpha_{eq}) \quad 3.15$$

$$A_{Si-W} + A_{Pt-W} = 2\pi R^2(1 + \cos \alpha_{eq}) \quad 3.16$$

and

$$A_{Si-A} + A_{Si-W} = A_{Pt-A} + A_{Pt-W} = 2\pi R^2 \quad 3.17$$

The dependence on  $\beta$  appears explicitly through a fourth equation obtained by expressing  $A_{Pt-A}$  in spherical coordinates ( $r, \theta, \varphi$ ). From Figure 3.8 the area of contact between platinum and the air can be written as:

$$A_{Pt-A} = R^2 \int_{\theta=\frac{\pi}{2}-\beta}^{\alpha_{eq}} \int_{\varphi=\arcsin(1/\tan\beta\tan\theta)}^{\pi-\arcsin(1/\tan\beta\tan\theta)} \sin\theta \cdot d\theta d\varphi \quad 3.18$$

$$A_{Pt-A} = \pi R^2(1 - \cos\alpha_{eq}) + 2R^2 \left[ \cos\alpha_{eq} \arcsin(\cotan\beta \cdot \cotan\alpha_{eq}) - \arctan \frac{\cos\beta}{\sqrt{\sin^2\beta - \cos^2\alpha_{eq}}} \right] \quad 3.19$$

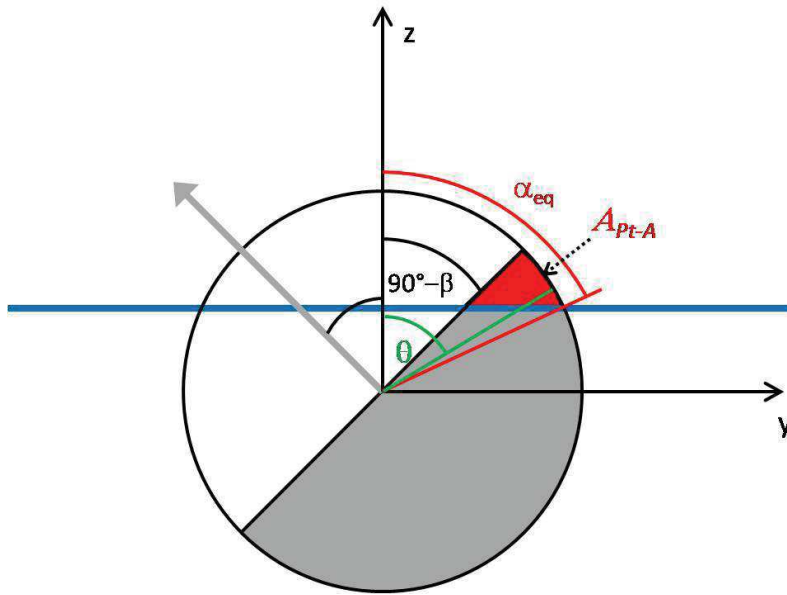


Figure 3.8 Scheme of the area  $A_{Pt-A}$  (red) in a spherical coordinate.

Two profiles have been calculated for two different immersion depth corresponding to the equilibrium contact angle of silica and platinum  $\alpha_{eq} = 61^\circ$  and  $52^\circ$  (as plotted in Figure 3.9). Three regimes are distinguished depending on the variation of  $E$  with  $90^\circ - \beta$ .

In regime I (Figure 3.9), the free energy decreases with  $90^\circ - \beta$  because the air-platinum and silica-water contact areas are progressively substituted by the air-silica and water-platinum areas. It corresponds to  $-\alpha_{eq} < 90^\circ - \beta < \alpha_{eq}$ , at both extremes of the  $x$ -axis in Figure 3.9.

A third regime (III), for  $180^\circ - \alpha_{eq} < 90^\circ - \beta < 180^\circ + \alpha_{eq}$ ,  $E$  increases for the symmetric reasons: the highest surface energy material (*i.e.* platinum) gets into larger and larger contact with the least condensed fluid phase.

Finally, both of regimes II and IV are separated by two ranges of orientations where  $E$  is independent of  $\beta$ , because the Janus boundary never crosses the triple line. It corresponds either to a minimum of  $E$  (platinum completely wetted, regime II) or a maximum (silica completely wetted, regime IV). Note that the extent of this last regime depends on  $180^\circ - 2\alpha_{eq}$ : the smaller  $\alpha_{eq}$  the larger the range.

The coupling between orientation and immersion depth is also pointed out in Figure 3.9: at the minimum of  $E(\beta)$ , the energy is smaller when platinum is completely immersed, while at the maximum of  $E(\beta)$ , the energy is smaller when silica is completely immersed. Along a complete rotation, Janus colloids would need to adjust their contact angle  $\alpha$  to minimize the energy.

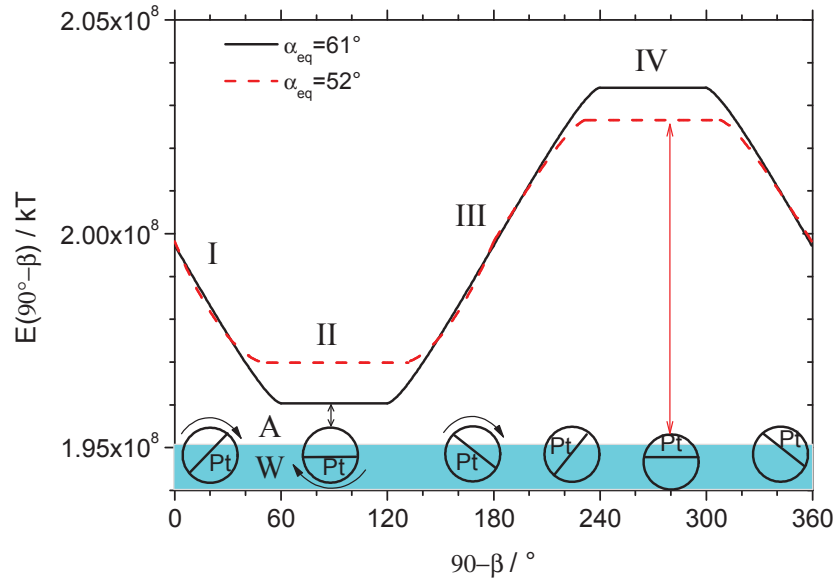


Figure 3.9 Two profiles calculated for two different vertical positions corresponding to the equilibrium contact angle of silica ( $\alpha_{eq} = 61^\circ$ , black line) and platinum ( $\alpha_{eq} = 52^\circ$ , red dashed line). The scheme at the bottom shows the Janus colloid rotates at air-water interface keeping the same immersion depth.

As the density of platinum is much higher than silica, we also studied the effect of gravity on the orientation of Janus colloid. We calculated the potential energy cost to orientate the Pt face from the bottom of Janus colloid to the top (Pt shell thickness, 20nm) and obtained a value of  $3.3 \text{ kT}$

which is much smaller than the energy of trapping the colloid at the water surface ( $\sim 10^6 kT$ , see Section 3.1). Therefore, the gravity influence on the particle orientation can be neglected.

The important point of the above results is that the Pt-silica Janus colloids, classically used as model system for the study of active motion in the bulk, are actually well suited to carry out active motion at the air-water interface. Catalytic platinum surface anticipated to be always in contact with aqueous fuel solution. Moreover, around the minimum of energy, there is a range of degenerated orientation states,  $\alpha_{eq} < 90^\circ - \beta < 180^\circ - \alpha_{eq}$ , and this ensures that the Janus boundary has very little chance to be parallel to the water surface.

In the following section, experimental observations of the orientation distribution of Janus colloids at the air-water interface are compared with the above theoretical considerations.

### 3.2.2 Observation of the orientation of Janus colloids

#### 3.2.2.1 In situ observation of the orientation by optical microscopy

Using the method presented in Chapter 2, Section 2.2.1, Janus colloids are trapped at the air-water interface in between two spaced glass slides. The orientation of Janus colloids can be observed by optical microscopy at high magnification, using an oil-phase  $\times 100$  objective. On the images presented in Figure 3.10, black regions of colloid are Pt caps. The Janus colloids orient with their Janus boundaries out of the air-water interfacial plane.

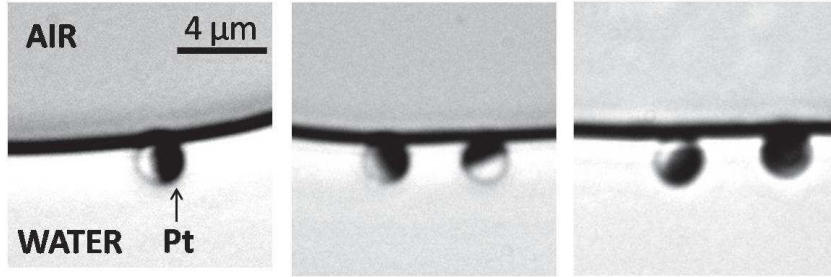


Figure 3.10 Microscopic images of Janus colloids at the air-water interface. The black surfaces of colloids are coated by Pt (see analysis in Chapter 2 Section 2.1.1).

#### 3.2.2.2 Distribution of orientation after gel-trapping

To get better images and to improve the statistics, the particles have been first trapped at the interface of an aqueous gel and transferred into a resin, as already explained. in Chapter 2, Section 2.2.1. Microscopic images are displayed in Figure 3.11 (A) and a histogram of the particles orientation distribution is also shown in Figure 3.11 (B).

Following the reference<sup>15</sup>, three classes of the orientation of Janus particles with respect to the air-water interface were distinguished. When the Janus boundary is parallel to the interface and the Pt face is fully immersed in water, the colloids appear completely dark. Colloids appear completely white when the silica face is fully immersed in water. When the Janus boundary is not

parallel to the interface, both black and white domains are distinguished on the particle (Figure 3.11 (A)). 70% out of 250 observed colloids have the Janus boundaries not parallel to the air-water interfacial plane. For 25% of the particles, the Pt face is completely immersed in water while only less than 5% of the particles have their silica faces completely immersed, which is qualitatively consistent with the fact that complete immersion of Pt corresponds to the minimum of interfacial energy. However, owing to the energy scale of Figure 3.9, it is very surprising to observe as many particles that have their silica faces completely immersed. Moreover, focusing on the particles that have the Janus boundary not parallel to the water surface, it seems that the particle has access to a broader range of orientation than the one expected from Figure 3.9 (even though we do not have the necessary resolution in  $\beta$ ). The orientation of the Janus colloids looks more random than it was anticipated. Such a random orientation has been observed for another Janus systems of gold-polystyrene particles at the oil-water interface.<sup>15</sup>

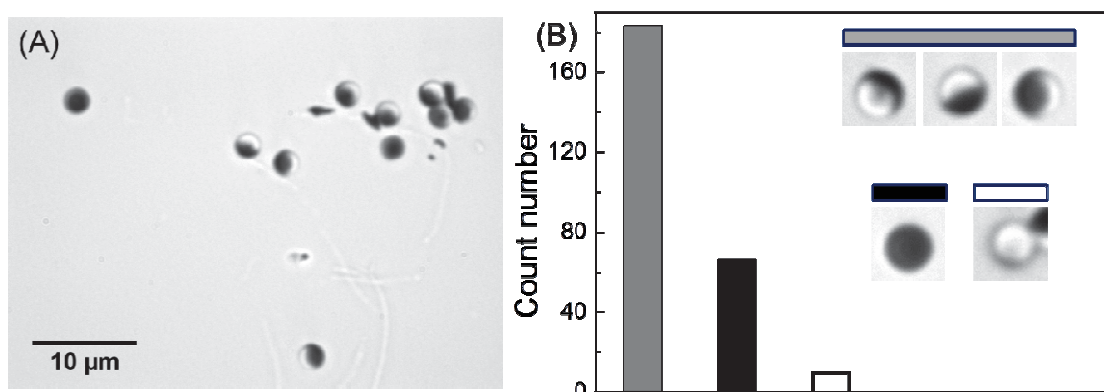


Figure 3.11. (A) Optical microscopy image showing Janus colloids trapped in polymerized NOA81 layer. The parts of beads visible were previously immersed in gelled water. Black region represents the Pt-coated surface. (B) Histogram of the particle orientation distribution. The gray, black and white bars represent separately the numbers of particles with Janus boundary orientated out of the interfacial plane (gray), particles with Pt cap orientated in the water (black) and particle with Pt cap orientated in the air (white).

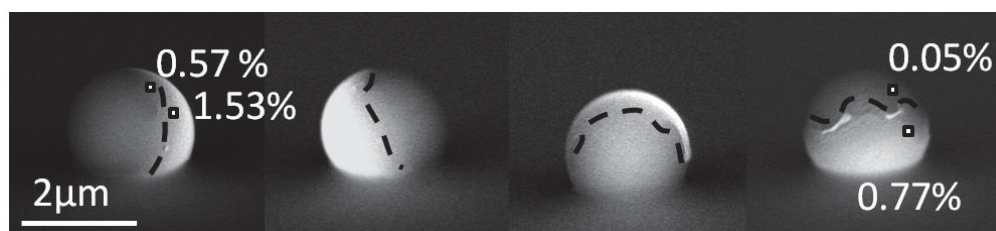


Figure 3.12 SEM images of Pt-SiO<sub>2</sub> beads trapped in the NOA81 layer. Pt atomic percentages were shown for the right two particles and the white parts represent Pt-coated surfaces.

Finer images have been obtained by SEM on the same samples. EDXS analysis shows that bright areas appearing in Figure 1.12 correspond to Pt areas: higher Pt atomic percentages are determined in the bright regions. The orientation of Janus colloids also shows a variety of ranges. Some Janus colloids were straddling the water surface with the air-water interfacial plane crossing their Janus boundaries. This can be seen clearly from the left two SEM images shown in Figure 3.12. For some Janus colloids, the interfacial plane can even cross only the Pt-coated surface (see the right SEM image in Figure 3.12). Note that the latter orientation is the one with the highest free energy (see in Figure 3.9).

### 3.3 Discussions

The energy landscapes as a function of the contact angle and the orientation of Pt face described up to now are ideal because they account only for wetting energies, for perfectly homogeneous and smooth colloidal surfaces and a flat fluid interface. Other interactions including electrostatic and van der Waals may also play a role on the contact angle and on the orientation.<sup>16,17</sup> Moreover, the interfacial energy barrier associated with the thermal hopping of the contact line over defects may lead to a metastable equilibrium contact angle and orientation.<sup>18</sup>

Because of the chemical and physical heterogeneities on the surface of Janus colloid, contact angle hysteresis exists for both faces of the Janus colloid. Hence, a range of stable angles rather than a single one can be observed. The maximum contact angle of this range is the advancing contact angle  $\alpha_A$  and the minimum one is the receding angle  $\alpha_R$  (see Table 3.1).<sup>1</sup>

Hence, similar to the case of a stable drop on an inclined planar substrate, the equilibrium contact angle hysteresis is related to the energy that can be stored on the colloid surface. For drops, one can define a hysteresis  $H = \gamma_{L-A}(\cos\alpha_R - \cos\alpha_A)$  as the force per unit length (see Chapter 1, Section 1.5.2) that keeps the drop staying at the inclined substrate against gravity. We estimated the effects of contact angle hysteresis on the free energy of a colloid and showed that this energy range could be in the order of few  $10^6 kT$ . This will be presented in the following. Note that this energy seems very large in particular when compared to the thermal agitation energy  $kT$ .

First, we consider the case of chemical heterogeneities present on the colloid surface. In this scenario, one could assume that in different regions of the colloid surface the surface energy (or interfacial tension) varies.

Assuming the contact angle hysteresis is in the range  $\alpha_R = 50^\circ$  and  $\alpha_A = 60^\circ$ , we calculate the free energy profile  $E(\alpha)$  for two ideal spheres of which the equilibrium contact angles are  $\alpha_R$  and  $\alpha_A$ , respectively (for  $R = 1 \mu\text{m}$ ,  $\gamma_{L-V} = 72 \text{ mN/m}$ ,  $\gamma_{S-L} = 25 \text{ mN/m}$ ,  $\gamma_{S-A} = 70 \text{ mN/m}$  ( $\alpha_{eq} = 50^\circ$ ) and  $\gamma_{S-A} = 60 \text{ mN/m}$  ( $\alpha_{eq} = 60^\circ$ ), see Figure 3.13). The difference between the energy minima of the two profiles are shown in Figure 3.13,  $\Delta E = E(\alpha_{eq} = 50^\circ) - E(\alpha_{eq} = 60^\circ) = 7 \times 10^6 kT$ . Hence, a variation of the colloid surface energy due to chemical heterogeneities  $\Delta\gamma_{S-A}$  of a few mN/m corresponds to a range of allowed free energy  $\Delta E$  of a few millions of  $kT$ .

Another possible scenario is related to the possibility of many metastable contact angles around the equilibrium one: in between the receding  $\alpha_R$  and advancing  $\alpha_A$  contact angles. The origin of these metastable states could be related to an activation energy connected to the triple line dynamics over the colloid surface. Following Blake's approach, this activation energy depends

on a characteristic frequency and a length describing the jump of the contact line.<sup>19</sup> This jump length  $\lambda$  could be related to the pinning of the contact line due to the roughness of the colloid surface. We can then relate the activation energy to the work of adhesion:  $W = A_L (\gamma_{S-A} + \gamma_{L-A} - \gamma_{S-L})$ , where  $A_L$  estimates the area covered by the line after a jump. Note that the work of adhesion describes the energy needed for creating the solid-air and liquid-air interfaces from a solid-liquid interface, which displays a clear picture of the activation energy during the jump of the triple line when advancing on the colloid surface. One could estimate this energy  $W \approx \lambda 2\pi R \gamma_{L-A} = 0.1 \times 10^6 kT$  (where  $\lambda \approx 1$  nm, Ref. [20]).

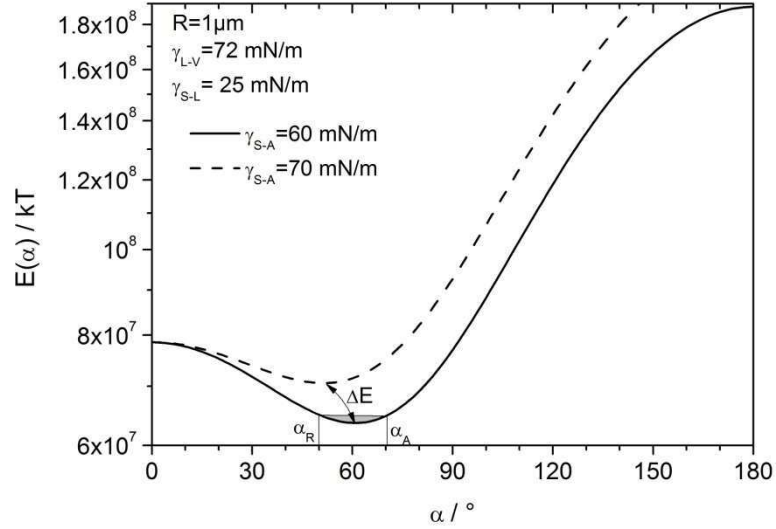


Figure 3.13 Energy profiles as a function of contact angle  $\alpha$  for colloid at two ideal states:  $R = 1 \mu\text{m}$ ,  $\gamma_{L-V} = 72 \text{ mN/m}$ ,  $\gamma_{S-L} = 25 \text{ mN/m}$ , (solid line)  $\gamma_{S-A} = 70 \text{ mN/m}$  ( $\alpha_{eq} = 50^\circ$ ) and (dotted line)  $\gamma_{S-A} = 60 \text{ mN/m}$  ( $\alpha_{eq} = 60^\circ$ ).

Our experiments on the Janus colloid orientations at the air-water interface show a large number of observations of colloids oriented with their Janus boundaries not parallel to the interface. Thermodynamics predicts that only the range  $\alpha_{eq} < 90^\circ - \beta < 180^\circ - \alpha_{eq}$  corresponds to the energy minimum. However, we observed a larger range of possible orientations with respect to the prediction. Orientations of the platinum face towards air were also observed few times, which correspond to the highest energy of the system. This energy cost, which is some millions of  $kT$ , cannot be paid by the thermal agitation energy. Surface roughness and chemical heterogeneities lead to equilibrium contact angle hysteresis, which could be regarded as the range of free energy that a surface can store. We estimate that because of the contact angle hysteresis, a Janus colloid possesses a free energy range of millions of  $kT$ , which explains our experimental observations. Note that heterogeneous regions are present everywhere on the Janus colloid surface, in particular, close to the Janus boundary. Contact angle hysteresis is expected to be very high close to the Janus boundary, which may lead to a larger range of orientation of the Janus colloids than the thermodynamic prediction (see Figure 3.9).



Finally, up to now, we always follow the crude assumption that the air-water interface remains flat for all orientation of the Janus colloid. Deformation of the fluid interfaces due to non-equilibrium orientations have been investigated by computer simulations in the minimum surface energy requirement.<sup>12</sup> The non-equilibrium orientation of the Janus colloid may cause a fluid interface deformation as sketched in Figure 3.14. An isolated single Janus colloid in a non-equilibrium orientation does not feel any capillary interaction because the fluid interface deforms, such that the net force on the triple line is zero. Accounts for a fluid deformation, one can calculate slightly lower free energy than assuming a flat interface.<sup>12</sup>

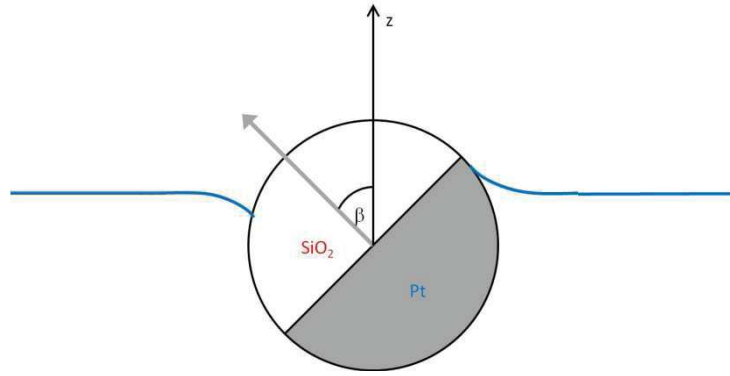


Figure 3.14 Sketch of a Janus colloid at a deformed fluid interface in a non-equilibrium orientation.

Now we consider the hypothetical scenario that the Janus colloid is in a non-equilibrium orientation and the interface remains flat. This scenario may represent just a transitory state after a rotation. The rotation may be due to the hydrodynamic torque felt by the colloid when moving parallel to the air-interface.<sup>21</sup> This torque may arise because the viscous drag is less in the air with respect to that in water (see Figure 3.15).

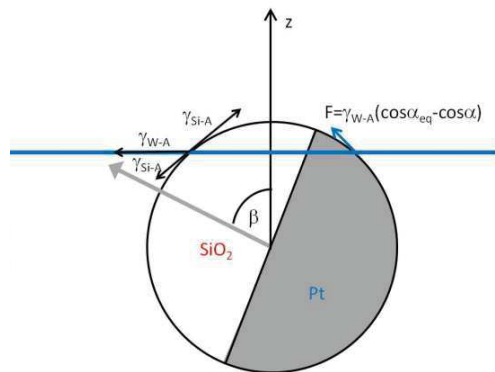


Figure 3.15 Sketch of a Janus colloid at a flat fluid interface in a non-equilibrium orientation.

If the Janus colloid equilibrium contact angle is the one of silica  $\alpha_{eq}(\text{SiO}_2) = 61^\circ$ , at the silica surface the force component tangential to the sphere is null, see Figure 3.15. On the contrary, at the platinum face, the contact angle  $\alpha = 61^\circ$  is higher than its equilibrium value  $\alpha_{eq}(\text{Pt}) = 52^\circ$ . Hence, a tangential force per unit length  $F = \gamma_{W-A} (\cos\alpha_{eq} - \cos\alpha)$  will act trying to move the liquid wedge upwards on the silica surface (Figure 3.15). Since we assume that the interface remains flat, an opposite force will act on the colloid, which tends to move the colloid towards the platinum side and downwards. This transitory force may disappear either upon a fluid interface deformation which leads to  $\alpha = \alpha_{eq}$ , or by a restoring rotation of the colloid to the original orientation with the platinum face completely immersed in water.

### 3.4 Conclusions

In this chapter, we described the energy landscapes for Pt-SiO<sub>2</sub> Janus colloid at the air-water interface as a function of its contact angle and orientation. From the experimental investigations, we found that most of the Janus colloids orientated with their Janus boundaries out of the air-water interfacial plane which would generate an efficient propulsive force parallel to the interface. Some of the colloids were trapped with their Janus boundaries across the air-water interface and some even had their platinum face in the air which conserved relative high energy. We estimated the energy cost for these non-equilibrium states should be some millions of  $kT$ . Further studies on contact angle hysteresis showed that these non-equilibrium orientations could be attributed to chemical or physical heterogeneities present on the two faces of the Janus colloid. The investigations and analysis on the wetting properties and the orientation of Janus colloids indicated that the Pt-SiO<sub>2</sub> Janus colloids were trapped at the interface and partially immersed in the aqueous phase. The range of orientations of the catalytic face of the Janus colloid observed indicated that the active motion at the water surface could occur. In the next two chapters, we will present and discuss the active motions.

### References

1. Bonn, D., Eggers, J., Indekeu, J., Meunier, J. & Rolley, E. Wetting and spreading. *Rev. Mod. Phys.* **81**, 739–805 (2009).
2. Pieranski, P. Two-Dimensional Interfacial colloidal crystal. *Phys. Rev. Lett.* **45**, 569 (1980).
3. Ondarçuhu, T., Fabre, P., Raphaël, E. & Veyssié, M. Specific properties of amphiphilic particles at fluid interfaces. *J. Phys.* **51**, 1527–1536 (1990).
4. Giguère, P. A. & Secco, E. A. Hydrogen peroxide and its analogues. *Canada J. Chem.* **32**, 550–556 (1951).
5. Owens, D. K. & Wendt, R. C. Estimation of the surface free energy of polymers. *J. Appl. Polym. Sci.* **13**, 1741–1747 (1969).
6. Binks, B. P. & Clint, J. H. Solid wettability from surface energy components: relevance to Pickering emulsions. *Langmuir* **18**, 1270–1273 (2002).

7. Binks, B. P. & Clint, J. H. Solid Wettability from Surface Energy Components: Relevance to Pickering Emulsions. *Langmuir* **18**, 1270–1273 (2002).
8. Gardner, J. R. & Woods, R. The hydrophilic nature of gold and platinum. *Journal of Electroanalytical Chemistry and Interfacial Electrochemistry* **81**, 285–290 (1977).
9. Li, Z., Beck, P., Ohlberg, D. a. ., Stewart, D. R. & Williams, R. S. Surface properties of platinum thin films as a function of plasma treatment conditions. *Surf. Sci.* **529**, 410–418 (2003).
10. Leo, V., Tusa, A., Araujo, Y. C. & Leo, V. Determination of the solid surface tensions I. The platinum case. **155**, 131–136 (1999).
11. Casagrande, C., Fabre, P., Raphaël, E. & Veyssié, M. “Janus Beads”: Realization and Behaviour at Water/Oil Interfaces. *Europhys. Lett.* **9**, 251–255 (2007).
12. Rezvantab, H. & Shojaei-Zadeh, S. Capillary interactions between spherical Janus particles at liquid–fluid interfaces. *Soft Matter* **9**, 3640 (2013).
13. Cheung, D. L. & Bon, S. a. F. Stability of Janus nanoparticles at fluid interfaces. *Soft Matter* **5**, 3969–3976 (2009).
14. Park, B. J. & Lee, D. Equilibrium orientation of nonspherical Janus particles at fluid-fluid interfaces. *ACS Nano* **6**, 782–790 (2012).
15. Park, B. J., Brugarolas, T. & Lee, D. Janus particles at an oil–water interface. *Soft Matter* **7**, 6413–6417 (2011).
16. Leunissen, M. E., van Blaaderen, A., Hollingsworth, A. D., Sullivan, M. T. & Chaikin, P. M. Electrostatics at the oil-water interface, stability, and order in emulsions and colloids. *Proc. Natl. Acad. Sci. U. S. A.* **104**, 2585–90 (2007).
17. Xu, L. *et al.* Hydrophobic coating- and surface active solvent-mediated self-assembly of charged gold and silver nanoparticles at water-air and water-oil interfaces. *Phys. Chem. Chem. Phys.* **11**, 6490–7 (2009).
18. Kaz, D. M., McGorty, R., Mani, M., Brenner, M. P. & Manoharan, V. N. Physical aging of the contact line on colloidal particles at liquid interfaces. *Nat. Mater.* **11**, 138–42 (2012).
19. Blake, T. D. The physics of moving wetting lines. *J. Colloid Interface Sci.* **299**, 1–13 (2006).
20. Boniello, G. *et al.* Brownian diffusion of a partially wetted colloid. *Nat. Mater.* 1–5 (2015). doi:10.1038/nmat4348
21. O’Neill Ranger, K. B., Brenner, H., M. E. Slip at the surface of a translating–rotating sphere bisected by a free surface bounding a semi-infinite viscous fluid: Removal of the contact-line singularity. *Phys. Fluids* **29**, 913 (1986).

## Chapter 4

### 4 Directional motion of Janus Colloids at the surface of water

#### Introduction

In this chapter, we explore the motion of Pt-SiO<sub>2</sub> Janus particles at the air-water interface with increasing concentration of the catalytic fuel, i.e. H<sub>2</sub>O<sub>2</sub>. Janus particles are trapped at the interface and their motion is truly two-dimensional. We use particle tracking video-microscopy to monitor the particle displacement in time. We calculate velocity autocorrelation functions and mean squared displacements to evaluate the propulsion velocity and the rotational diffusion time. A comparison with the active motion in the bulk is also presented. By performing image analysis, we could also monitor the orientation of the platinum surface during the active motion.'

#### 4.1 Concentration, contact angle and orientation of Janus colloids at the air-water interface

Using an airbrush we deposited particles onto the air-water interface with an approximate density of 50 particles mm<sup>-2</sup>, as explained in Chapter 2 Section 2.3.1. This interfacial density corresponds to a very dilute regime that the interaction between colloids can be neglected.

We measured the contact angle of Janus colloids using two techniques: (i) in situ optical microscopy; (ii) and the gel trapping method. The techniques were described in Chapter 2 Section 2.2.1. We found  $\alpha = 57.8 \pm 9.1^\circ$  by in situ optical microscopy and  $\alpha = 63.6 \pm 2.2^\circ$  by gel trapping method (see also Chapter 3 Section 3.1).

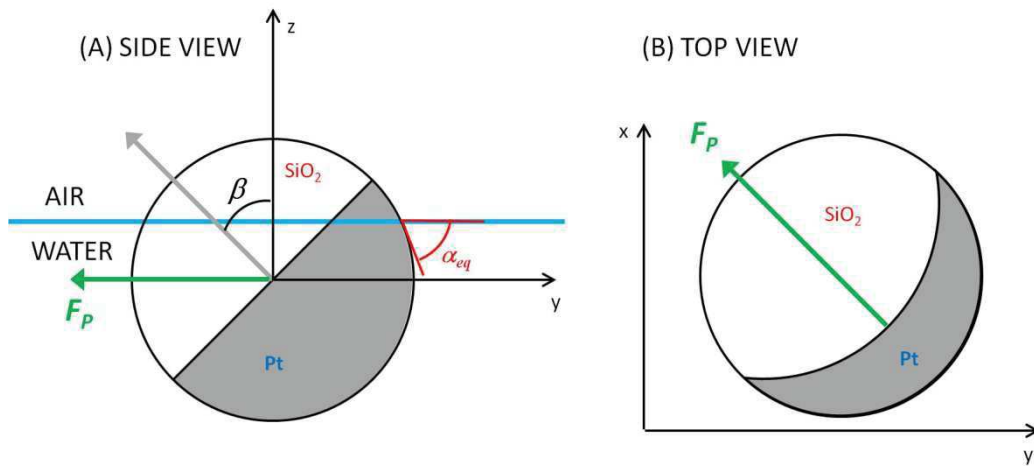


Figure 4.1 Schematic representation of Janus colloid at the air-water interface with its Janus boundary normal formed an angle  $\beta$  with  $z$ -axis.  $\alpha_{eq}$  is the equilibrium contact angle of a colloid with water.  $F_P$  is the effective propulsive force.

The orientations of Janus colloids at the air-water interface in the absence of fuel ( $\text{H}_2\text{O}_2$ ) have been experimentally investigated as presented in Chapter 3, Section 3.2. An angle  $\beta$  is defined as the angle formed between the Janus boundary (i.e. where the two faces meet) normal and the  $z$ -axis (parallel to the interface normal) as shown in Figure 4.1. From a thermodynamic point of view, Janus colloids may orientate within the range  $\alpha_{eq} < 90^\circ - \beta < 180^\circ - \alpha_{eq}$  ( $\alpha_{eq}$  is the equilibrium contact angle, see discussions in Chapter 3, Section 3.3 and 3.4). However a larger range of orientation has been experimentally observed and most of the colloids orientate with their Janus boundaries out of the air-water interfacial plane (the  $x$ - $y$  plane in Figure 4.1). In the presence of  $\text{H}_2\text{O}_2$ , the Pt-cap generates a propulsive force ( $F_p$ ) parallel to the interfacial plane as displayed in Figure 4.1. A discussion are presented in Section 4.4 and 4.5.

Note that once Janus colloids are trapped at the air-water interface, they cannot escape from the interfacial plane ( $x$ - $y$  plane) to the water bulk, being the transfer energy  $\Delta E \gg kT$  (see Chapter 3 Section 3.2.1). Colloids that haven't been trapped at the interface would eventually sediment to the bottom. This sedimentation can be clearly observed by monitoring focus differences under the microscope. For the interfacial measurements reported in the following sections, we did not observe any change of focus on the particle along with time, which is an additional proof that those particles were confined at the two-dimensional air-water interface.

## 4.2 Trajectories

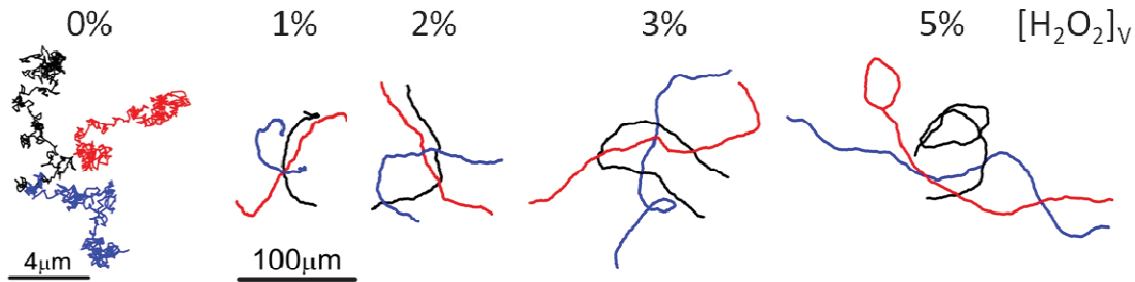


Figure 4.2 Trajectories of Janus particles at the water interface ( $x$ - $y$  plane) over 20 seconds under different fuel concentrations  $[\text{H}_2\text{O}_2]_v$ . Measurements performed at a field of view of  $477 \mu\text{m} \times 358 \mu\text{m}$ .

Figure 4.2 displays two-dimensional trajectories of Janus colloids at the water surface under different  $\text{H}_2\text{O}_2$  fuel concentrations in a field of view of  $477 \mu\text{m} \times 358 \mu\text{m}$ . In the absence of  $\text{H}_2\text{O}_2$  (0%), particles undergo characteristic Brownian motions confining their trajectories in small areas (end-to-end distances of trajectories remain below  $\sim 7 \mu\text{m}$  during 20 s). In the presence of  $\text{H}_2\text{O}_2$ , directional displacements in the order of  $\sim 100 \mu\text{m}$  have been measured over an observation time of 20 seconds. Note that even for such long distances ( $\sim 400$  times the particle radius for trajectories at 5%) and times only few directional changes were observed (Figure 4.2). In contrast, clear long-range random walks have been previously observed for Pt-coated polystyrene beads in the bulk of  $\text{H}_2\text{O}_2$  aqueous solution (for which the rotational diffusion time  $\tau_R = 1/D_R \approx 6$  s and velocity  $V \approx 6 \mu\text{m/s}$ ).<sup>1</sup> In our experimental system, at longer times and distances, the possibility

of very long range random walks might exist. However, those scales are beyond the experimental windows of particle tracking video microscopy shown here ( $477 \mu\text{m} \times 358 \mu\text{m}$ ).

A comparison between two representative trajectories of moving Janus colloids at the surface of water and in the bulk of water are shown in Figure 4.3. The active motion in bulk is three dimensional and the trajectory shown here is the two-dimensional projection. When tracking the motion in bulk, due to the vertical movement of colloid, the focal plane of the microscope needed to be adjusted. Comparing both trajectories in Figure 4.3 strongly suggests that the motion at the air-water interface is much more persistent than the motion in bulk.

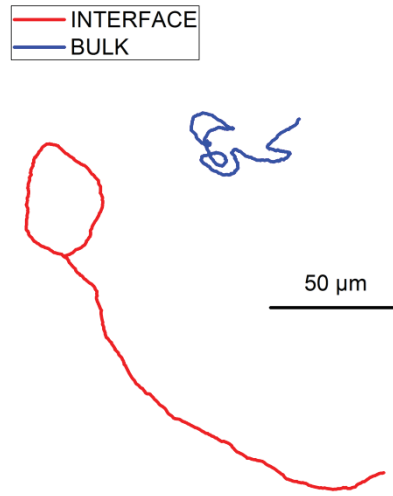


Figure 4.3 Trajectories of a Janus particle at the water interface and in bulk water at  $[\text{H}_2\text{O}_2]_{\text{V}}=5\%$  over 16 seconds.

## 4.3 Motion analysis

### 4.3.1 Velocity autocorrelation functions

To characterize the motion of Janus colloids at the water surface, velocity autocorrelation functions (*VACF*) were calculated. As shown in Figure 4.4, some *VACF* of the velocity vector  $\langle \mathbf{v}(\Delta t) \cdot \mathbf{v}(0) \rangle$ , corresponding to trajectories in Figure 4.4, are plotted as a function of time delay  $\Delta t$ . The quantity  $\langle \mathbf{v}(\Delta t) \cdot \mathbf{v}(0) \rangle$  describes the probability of a colloid keeping the same velocity after a delay time  $\Delta t$ . This probability is lost when the colloid either changes significantly its direction or its velocity modulus.

*VACF* of a Brownian trajectory is also plotted in Figure 4.4 (squared plot). It decays to zero in extremely short time as expected (see Chapter 1, equation 1.4). Hence, the Brownian contribution to *VACF* (see Chapter 1, equation 1.12) was not considered. Therefore, as displayed in Figure 4.4 (solid red line), we fitted the *VACF* by:

$$\langle \mathbf{v}(\Delta t) \cdot \mathbf{v}(0) \rangle = V^2 \exp(-D_R \Delta t) \quad 4.1$$

Autocorrelation function of the velocity vector  $\mathbf{v}$  could also be fitted accounting for a “run-and-tumble” model (see also Chapter 1, equation 1.11):

$$\langle \mathbf{v}(\Delta t) \cdot \mathbf{v}(0) \rangle = V^2 (\tau_R - \Delta t) / \tau_R \quad 4.2$$

where  $\tau_R$  is the characteristic time at which the directional change occurs, i.e. the rotational diffusion time.<sup>3</sup> The fit is shown by the dashed line in Figure 4.4.

As discussed in Chapter 1, Section 1.5, colloids moving at the air-water interface would experience different boundary conditions and frictions from that in bulk. Therefore, we expect that the fitting parameters of the *VACF* describing the interfacial motion of Janus colloid should also differ from that for the bulk motion. In the following we will present the fitting results.

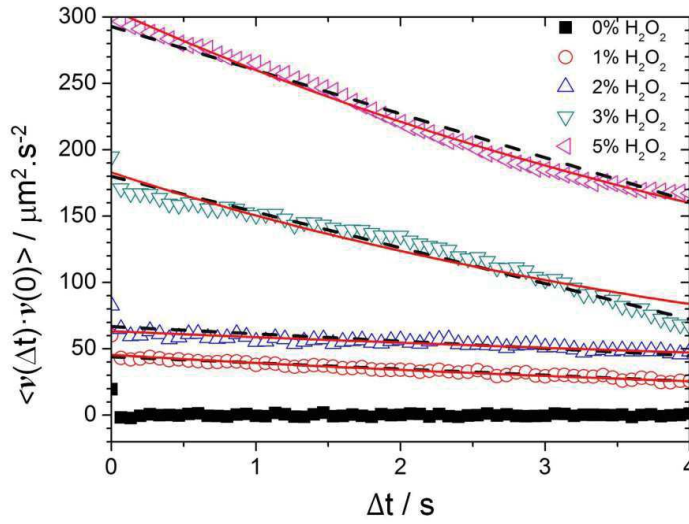


Figure 4.4 Velocity autocorrelation functions under different  $\text{H}_2\text{O}_2$  fuel concentrations. Solid red lines are the fits of the data obtained with equation 4.1. Dashed black lines are the fits of the data obtained with equation 4.2.

### 4.3.2 Propulsion velocity

*VACF* can be fitted by both equation 4.1 and 4.2. The active velocities and rotational times obtained from the two fits lead to very similar values. First we describe the active velocity  $V$ . The active velocity for trajectories measured in a field of view of  $477 \mu\text{m} \times 358 \mu\text{m}$  is plotted in Figure 4.5. It increases with  $\text{H}_2\text{O}_2$  concentration and reaches about  $18 \mu\text{m/s}$  at 5% fuel concentration.

We have also investigated the active motions of colloids in the bulk at three different fuel concentrations, as shown in Figure 4.5. For comparison, the reported bulk velocity of Pt-SiO<sub>2</sub> Janus particles (diameter  $\sim 2.01 \mu\text{m}$ , Pt layer 50 nm) in literature is also plotted (solid line in Figure 4.5).<sup>2</sup> It shows that the active velocity measured at the air-water interface is about twice of the bulk values. This increase will be discussed in Section 4.5. The bulk velocities we measured



are slightly different from the reported values. These differences may be either due to the platinum coating or to the hydrodynamic friction. The Pt layer thickness (50 nm) used in the literature<sup>2</sup> is also different from ours (Pt layer, 20 nm in thickness with  $\sim 10$  nm grains) which may lead to a different chemical reaction rate<sup>17,18</sup> and further resulting in different active velocity (see Chapter 1, Section 1.4). Moreover, the velocity depends on the hydrodynamic friction which increases strongly when the distance between the particle and the wall decreases.<sup>4</sup> We measured the velocity for Janus colloids which are far from the bottom wall; however we do not know if Gibbs and Zhao<sup>2</sup> did the same or measured close to the bottom wall.

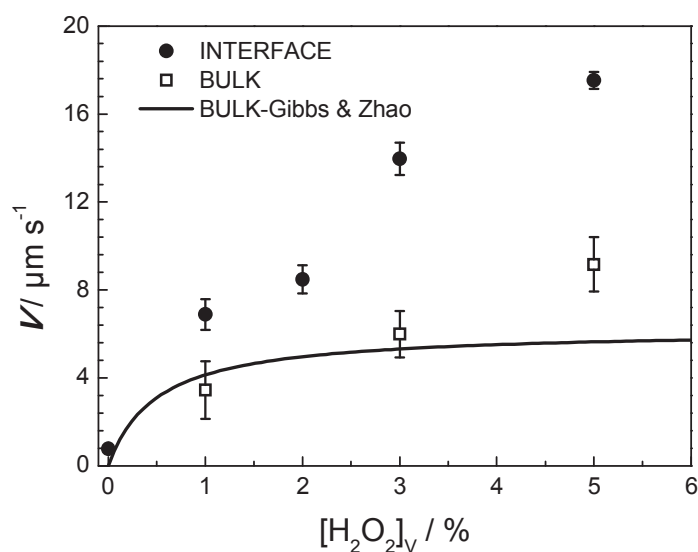


Figure 4.5 Active velocity  $V$  of Janus colloids at the air-water interface (filled circle, corresponding to trajectories in Figure 4.2) and in the bulk (open square). The solid curve is the fitting result of velocity in bulk reported by Gibbs and Zhao<sup>2</sup> for Pt-SiO<sub>2</sub> Janus particles of diameter 2.01  $\mu\text{m}$ .

### 4.3.3 Rotational diffusion coefficient

From velocity autocorrelation function we could also evaluate the characteristic time  $\tau_R = 1/D_R$ , which describes the time scale of directional changes during the active motion. The two fits by different  $VACF$  expressions (see Eqn. 4.1 and 4.2) gave very similar values. We plotted  $D_R$  in Figure 4.6 (circle). For comparison, the theoretical rotational diffusion coefficient of a colloid, (i) fully immersed in the water bulk and far away from the air-water interface (solid line); (ii) half immersed in water (dashed line) and rotating about the  $z$ -axis parallel to the interface normal in no-slip condition (see Chapter 1 Section 1.5.3),<sup>5</sup> are also presented in Figure 4.6.

Since the contact angle of the Janus colloids with water is  $57.8 \pm 9.1^\circ$  (by in situ optical microscopy), the rotational diffusion coefficient should also lay in between the values for fully and half-immersed particles (contact angle, 0 -90°). However in the presence of H<sub>2</sub>O<sub>2</sub>, some of the data show relatively low values of the rotational diffusion coefficients, which can be even

lower than the rotational diffusion coefficient of a colloid completely immersed in the bulk water (solid line in Figure 4.6).

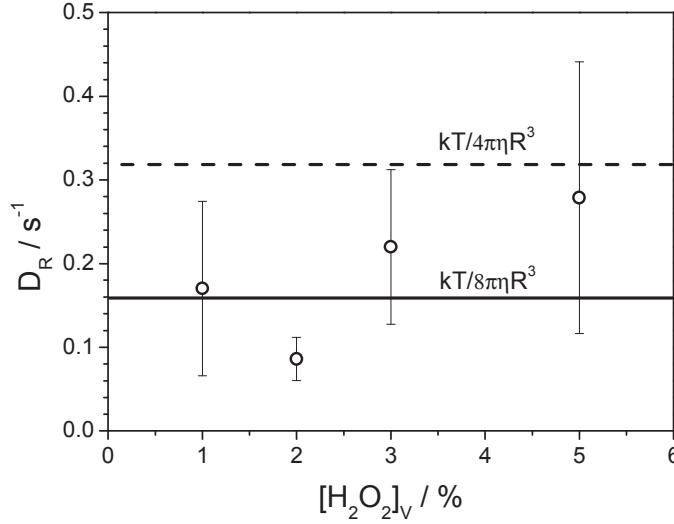


Figure 4.6 Rotational diffusion coefficient as a function of different fuel concentrations, extracted from the fit of the velocity autocorrelation functions for different moving colloids (in Figure 4.2). The error bars were evaluated by the standard deviation. The solid line corresponds to the rotational diffusion coefficient of a Brownian colloid in water bulk and the dashed line to a half-immersed colloid at the air-water interface.

Finally, knowing the velocity and the rotational diffusion time we could estimate a persistence length equal to  $V / D_R \approx 85 \mu\text{m}$ , which is significantly higher than the value obtained in the bulk  $V / D_R \approx 54 \mu\text{m}$  at the same  $\text{H}_2\text{O}_2$  concentration ( $[\text{H}_2\text{O}_2]_V = 5\%$ , see Figure 4.5 and Figure 4.6; in the bulk:  $V \approx 9 \mu\text{m/s}$  and  $\tau_R = 6.3 \text{ s}$ ).

### 4.3.4 Drift velocity and Mean squared displacement

#### 4.3.4.1 Drift velocity

To check the robustness of our results, we also performed a series of control experiments in order to rule out the effect of drift due to the convection, which is always suspected at the water surface.<sup>6</sup> We measured the drift velocities by studying the diffusion of passive silica beads at the same fuel concentrations used for Janus particles. As shown by the filled squares in Figure 4.7, velocities about  $1 \mu\text{m/s}$  have been measured, which are much smaller than the active velocities of Janus colloids (circles in Figure 4.7, also see filled circles in Figure 4.5). Here the drift velocity and active velocity were both evaluated by tracking particles in a field of view  $125 \mu\text{m} \times 94 \mu\text{m}$  to improve the accuracy of the particle position detection and speed evaluation, especially for the passive colloids which move in small steps.

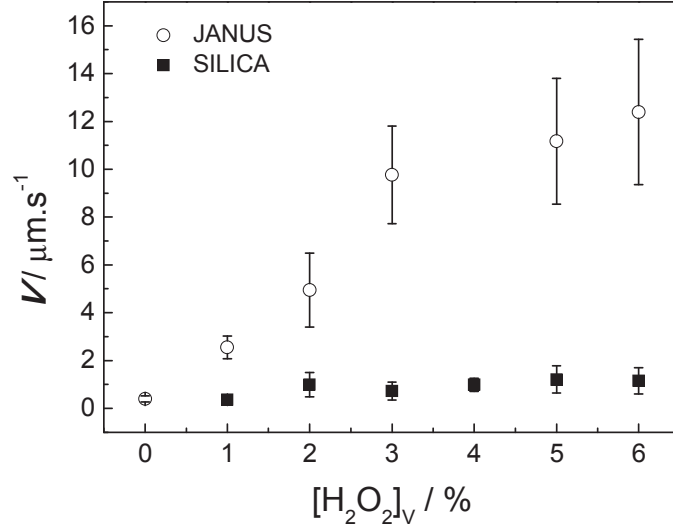


Figure 4.7 Active velocity  $V$  of Janus colloids (circle) and velocity of passive silica beads (filled squares) as a function of  $\text{H}_2\text{O}_2$  fuel concentrations by tracking particles in a field of view  $125 \mu\text{m} \times 94 \mu\text{m}$ . The error bars are the standard deviations of the active velocities of 8 different colloids for each concentration.

#### 4.3.4.2 Mean squared displacement

Just for the sake of comparison, we also used mean squared displacement ( $MSD$ ) analysis ( $VACF$  analysis is shown before) to evaluate the active velocity and the rotational diffusion time. The general expression of the  $MSD$  is (see also Chapter 1 Section 1.2.4):<sup>7</sup>

$$MSD = 4D_T\Delta t + \frac{V^2\tau_R^2}{3} \left[ \frac{2\Delta t}{\tau_R} + e^{-2\Delta t/\tau_R} - 1 \right], \quad 4.3$$

We used this equation to fit the data of the trajectories obtained in a field of view of  $477 \mu\text{m} \times 358 \mu\text{m}$  (see Figure 4.2.) The representative mean squared displacements as a function of delay time at different fuel concentrations and the corresponding fitted curves (solid line) are plotted in Figure 4.8 (A).

We obtained slightly different values for active velocities  $V$  and rotational diffusion coefficient  $D_R$  with respect to that from the  $VACF$  analysis, see Figure 4.8 (B) and (C). As shown in Figure 4.8 (A), we plotted the  $MSD$  until 10 s and obtained good fits at all time delay scale. However, from a statistic point of view, generally the  $MSD$  calculation at shorter time delay is more reliable (see Chapter 2, Section 2.3.4). During the fitting procedure of  $MSD$ , some parameters showed coupling which seemed less robust. Instead, the fits by using  $VACF$  are somewhat more robust since the mathematical expression is simple and the parameters are clearly decoupled.

For trajectories in a field of view  $125 \mu\text{m} \times 94 \mu\text{m}$  (see representative trajectories in Figure 4.10 and Figure 4.12), none or very few significant directional changes occur and the approximated expression of the  $MSD$  for  $\tau_R \gg \Delta t$  (rotational diffusion time is much larger than delay time) was used to fit the data, see Figure 4.9.

$$MSD = 4 D_T \Delta t + 2/3 V^2 \Delta t^2$$

4.4

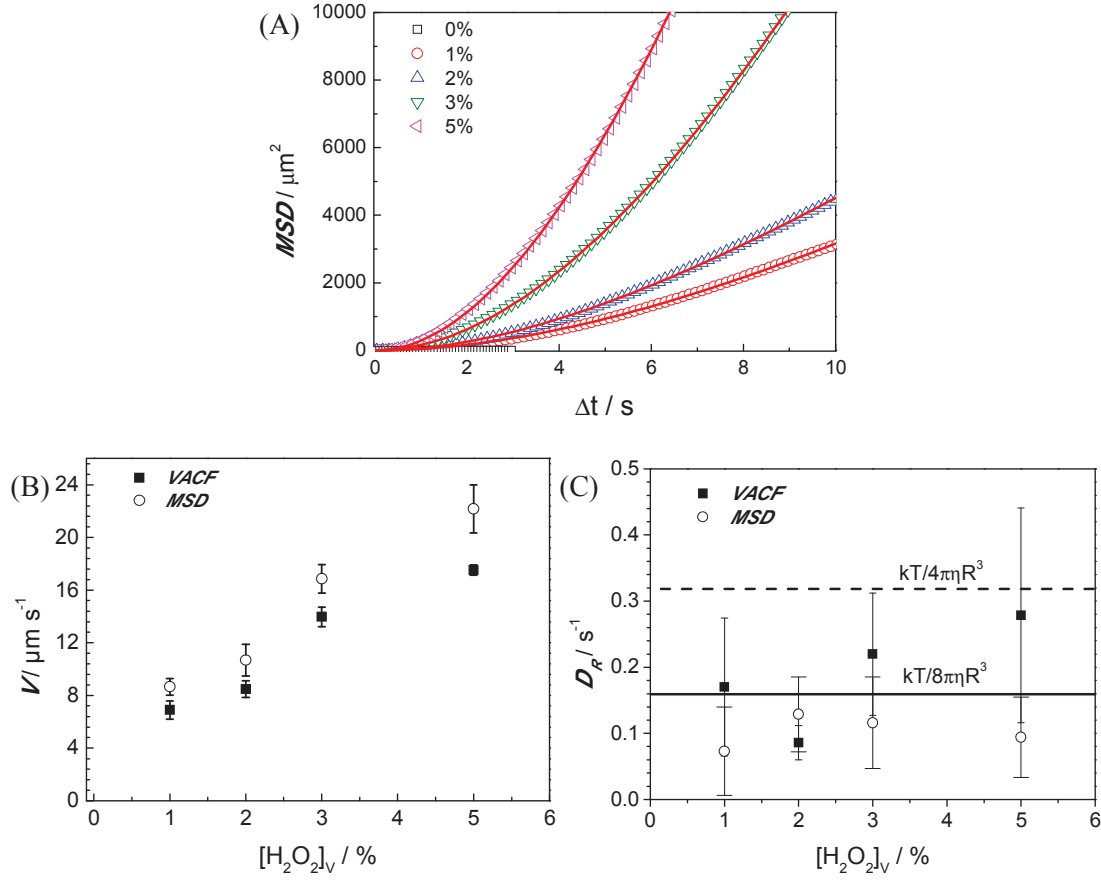


Figure 4.8 (A) Mean squared displacement ( $MSD$ ) as a function of the delay time at different  $[\text{H}_2\text{O}_2]_V$  for trajectories from the field of view  $477 \mu\text{m} \times 358 \mu\text{m}$  (see Figure 4.2.). Solid lines represent the best fits of equation 4.3. (B) Active velocities and (C) Rotational diffusion coefficients calculated from  $VACF$  (filled square) and  $MSD$  (open circle) are plotted as a function of fuel concentrations.

In Figure 4.9  $MSD$  as a function of the delay time until 3 seconds for  $\text{H}_2\text{O}_2$  concentrations in the range between 0 and 6 % is shown in a  $\log\text{-}\log$  plot. In the absence of  $\text{H}_2\text{O}_2$ ,  $MSD$  is linear as expected for random Brownian motion and the slope is 1 in a  $\log\text{-}\log$  plot. In the presence of  $\text{H}_2\text{O}_2$ , all  $MSD$  curves are parabola with the same slope equal to 2 in a  $\log\text{-}\log$  plot.

We determined  $D_T$  with the data in the absence of fuel ( $[\text{H}_2\text{O}_2]_V = 0\%$ ) and constrained the value of  $D_T$  for all other fits (Figure 4.9). We found  $D_T = 0.208 \mu\text{m}^2/\text{s}$  at the interface, a value very similar to the bulk value ( $\frac{kT}{6\pi\eta R} = 0.218 \mu\text{m}^2/\text{s}$ ). In the prediction presented in Chapter 1 Section 1.5.3, the friction at interface was expected to be smaller than that in bulk, which leads to a higher translational diffusion for colloid moving at the air-water interface.<sup>8</sup> However, here we measured a slowing down of the translation diffusion when compared to the prediction.

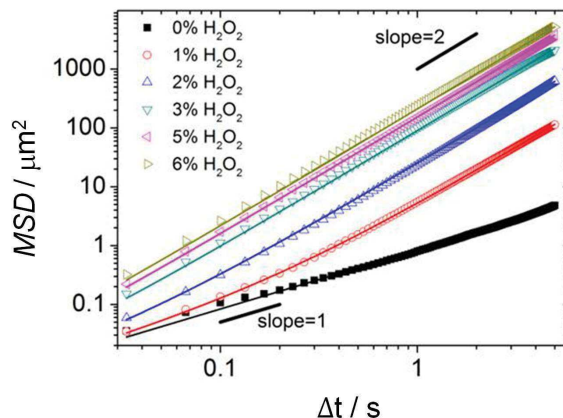


Figure 4.9 Mean squared displacement ( $MSD$ ) as a function of the delay time at different  $[H_2O_2]_V$  for trajectories observed at field of view  $125\ \mu m \times 94\ \mu m$ . Solid lines represent best fits of equation 4.4.

The active velocity  $V$  (averaged for 8 particles for each concentration) for trajectories in this field of view ( $125\ \mu m \times 94\ \mu m$ ), calculated by MSD analysis is shown before in Figure 4.7.  $V$  increases with the fuel concentration and for  $[H_2O_2]_V = 6\%$  the average velocity is ca.  $18\ \mu m/s$ . Here velocities are somewhat lower than that obtained for trajectories in the larger field of view ( $477\ \mu m \times 358\ \mu m$ ) and show larger error bars.

## 4.4 Interfacial orientation of swimming Janus colloids

### 4.4.1 Orientation of Pt cap

For some trajectories, we measured in the field of view  $125\ \mu m \times 94\ \mu m$ , by performing image analysis it was possible to obtain information on the orientation of the Pt-coated surface during the motion of Janus colloid at the water surface. A representative trajectory is shown by the red line in Figure 4.10. The inserted three images below the trajectory are real images of the Janus particle observed by a microscope, which show a darker region corresponding to the Pt cap. To enhance the contrast between the two regions, a binary process was performed to the images using a constant threshold (by implementing a routine in *IDL* software). The processed images are shown above the trajectory (Figure 4.10). White color in the thresholded images corresponds to the darker part (represents the Pt region) of the colloid in the raw images. It indicates that the Janus colloid orients with the Pt cap in the rear during its motion. The same was found for all beads which their Pt faces could be detected. Hence, it demonstrates that the catalytic surface drives the particle to move directionally; ruling out that drift is the cause of directional motion. Approximately constant Pt areas were observed along the motions, which suggests that no significant directional change occurred, and this agrees with the expected slowing down of rotations about an axis perpendicular to the interface normal (the  $x$ - and  $y$ -axis).<sup>5</sup>

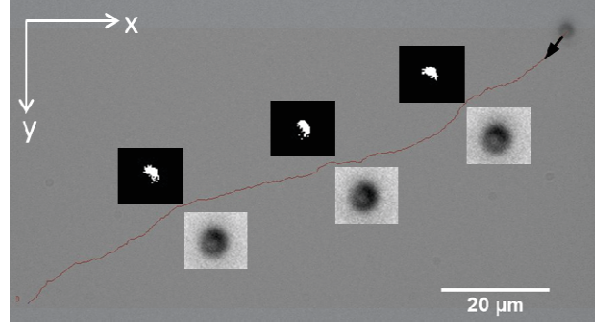


Figure 4.10 Trajectory (red line) of a Janus colloid at 5%  $[\text{H}_2\text{O}_2]_v$  at the water surface. Three pairs of magnified images (raw (below the trajectory) and thresholded (above the trajectory)) are inserted from right to left at time 2, 4, 6 seconds, respectively. Measurements performed at a field of view  $125 \mu\text{m} \times 94 \mu\text{m}$ .

#### 4.4.2 Characterization of orientation by velocity autocorrelation function

To characterize the trajectories displayed in Figure 4.2, we have also computed the autocorrelation function  $\langle \mathbf{v}(\Delta t) \cdot \mathbf{v}(0) \rangle$  of the velocity modulus,  $v = \sqrt{v_x^2 + v_y^2}$  (where  $v_x = \frac{dx}{dt}$  and  $v_y = \frac{dy}{dt}$  are the components of the velocity in the interfacial plane  $x$ - $y$ ).

$\langle \mathbf{v}(\Delta t) \cdot \mathbf{v}(0) \rangle$  can be related to the out of plane orientation of Pt cap as described by the angle  $\beta$  sketched in Figure 4.1. For most of the trajectories we analyzed, the  $\langle \mathbf{v}(\Delta t) \cdot \mathbf{v}(0) \rangle$  keeps constant when the delay time increases; and directional changes occurred smoothly with the Janus colloid rotating about the  $z$ -axis (parallel to the interface normal). Figure 4.11 (A) shows a typical trajectory and in Figure 4.11 (B) the  $VACF$  of the velocity modulus together with the  $VACF$  of the velocity vector are plotted as a function of delay time. The decrease of the velocity vector autocorrelation function can be ascribed to directional changes in the interfacial plane ( $x$ - $y$ ). Velocity modulus keeps approximately constant pointing to a slowing down of rotation about the  $x$ - and  $y$ -axis. In Fig. 4.11, the rotational diffusion time  $\tau_R = 1 / D_R \sim 2.6$  s.

A different scenario occurs for few trajectories when a sharp directional change occurs. In this case, we could also observe a significant change of the Pt cap orientation (also corresponding to the propulsive force direction, see Figure 4.1). Indeed, a clear correlation between the sharp directional change of the trajectory and the orientation change of the platinum regions can be observed in Figure 4.12. Far from the turning point, by performing image analysis as shown by thresholded images in Figure 4.12 (A), one could distinguish the Pt face (white regions) of the Janus colloid. Close to the turning point, the Pt regions cannot be clearly detected. Note that the autocorrelation function of the velocity modulus is not constant but decreases with  $\Delta t$  (Figure 4.12 (B)). By fitting the autocorrelation function of the velocity vector  $\langle \mathbf{v}(\Delta t) \cdot \mathbf{v}(0) \rangle$ , we find a rotational diffusion time  $\tau_R = 1 / D_R \approx 5$  s whilst from the decrease of  $\langle \mathbf{v}(\Delta t) \cdot \mathbf{v}(0) \rangle$  a characteristic time of about 17 s reveals the dramatic slowing down of the out of interfacial plane rotational diffusion.



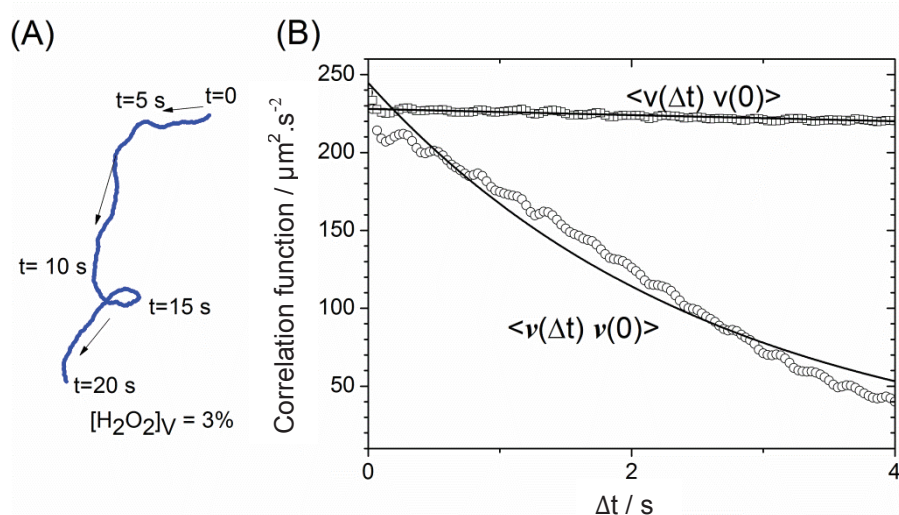


Figure 4.11 (A) Trajectory of a Janus colloid at the interface (from Figure 4.2). (B) Autocorrelation functions of the velocity modulus  $\langle v(\Delta t) \cdot v(0) \rangle$  and vector  $\langle v(\Delta t) \cdot v(0) \rangle$ . Black lines represent the fits of the data using equation 4.1.

These findings indicate that the platinum face changes its orientation at the sharp turning point, rotating about both an axis parallel (the  $x$ - and  $y$ - axis) and perpendicular to the interface normal (the  $z$ -axis). The two rotations are related to the in-plane and out of plane orientations of the platinum face at the air-water interface, respectively (as can be observed in Figure 4.12 (A)).

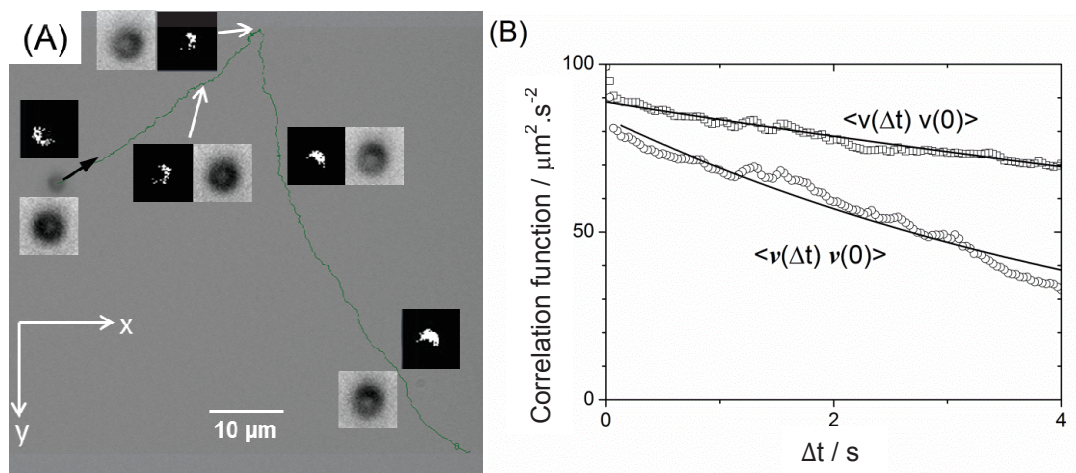


Figure 4.12 (A) Trajectory (green line) of an active Janus colloid at the water surface. Pairs of magnified images (raw and thresholded) inserted from left to right at different times. (B) Autocorrelation functions of the velocity modulus  $\langle v(\Delta t) \cdot v(0) \rangle$  and vector  $\langle v(\Delta t) \cdot v(0) \rangle$ . Black lines represent the fits of the data by equation 4.1.



## 4.5 Discussions and conclusions

We can now discuss the results reported in the previous sections describing the directional motion of Janus colloids at the air-water interface. Comparing to previous investigations,<sup>1,2</sup> we measured velocity as high as  $\sim 18 \mu\text{m/s}$  (twice the value measured in the bulk) and directional trajectories, which show only few directional changes (Figure 4.2).

### 4.5.1 Persistence of trajectory

To explain why directional trajectories are much more persistent at the water surface with respect to the bulk, we need to recall that the randomization process is dictated by the rotational diffusion time.<sup>1</sup> A self-propelled colloid in the bulk can experience rotations about three different Cartesian axes with the same probability and a single diffusion rotational time  $\tau_R \approx 1/D_R$ . In contrast at the interface ( $x$ - $y$  plane) for Janus particles, three different rotational times might exist. Only one rotation  $D_{R,z}$  (about an axis parallel to the interfacial normal) would be allowed in the ideal no-lip condition (see Chapter 1 Section 1.5.3).<sup>5</sup> As known in partial wetting dynamics,  $D_{R,x}$  and  $D_{R,y}$  (rotational diffusion about the  $x$ - and  $y$ -axis respectively) are significantly slowed down (but not completely suppressed) because of the high dissipation occurring close to the triple line.<sup>9,10</sup>

### 4.5.2 Rotational diffusion time

By calculating the autocorrelation function of the velocity vector and modulus, we also gain information on a slowing down of the rotational diffusion (Figure 4.11 (B) and Figure 4.12 (B)). Some rotational times ( $1/D_R$ ) are comparable or even higher than the bulk values for spheres (Figure 4.6). To fit a rotational time of  $\approx 10$  seconds using the rotational diffusion time of a 2D platelet  $1/D_{R,z} = 32\eta R^3/3kT$ , one would find an equivalent radius  $R = 1.56 \mu\text{m}$  which is 50 % larger than the colloid radius.<sup>11</sup>

As reported in the literature, the slowing down of the translational and rotational diffusion of colloids at the interface is a rather complex issue.<sup>12,13,14</sup> A purely hydrodynamic picture of the problem may relate the diffusion only to the contact angle of the particle and the viscosities.<sup>8</sup> However, many experimental data in the literature reported deviations from hydrodynamic predictions.<sup>12,13,14</sup> This slowing down may be attributed to an interfacial friction which adds to the hydrodynamic friction. In particular, thermal fluctuations of the contact line over the colloid surface can slow down significantly the interfacial motion.<sup>9</sup> Very recently Boniello et al. reported a systematic investigation on the slowing down of translational and rotational diffusion of spherical and ellipsoidal particles at the air-water interface.<sup>15</sup> They found that the slowing down could be modeled as an extra friction due to the contact line fluctuations. The interfacial friction could be quantified for two different cases. The first one was related to a fluctuating contact line around an equilibrium position as in the Blake's model of partial wetting (see also Chapter 1, Section 1.5.3).<sup>10</sup> The second scenario dealt with the friction resulting from a thermal capillary wave on a pinned contact line.<sup>15</sup> For ellipsoidal particles, the resulting fluctuating forces at the contact line gave rise to a fluctuating torque and hence to an extra rotational friction. This extra interfacial rotational friction depended on the aspect ratio of ellipsoidal particle and on the heterogeneity of the particle. It was found that for an ellipsoidal colloid with aspect ratio  $\sim 1.5$  the rotational friction at air-water interface is  $\sim 1.7$  times of that in bulk.<sup>15</sup> In our case, as presented in Chapter 2, Section 2.1.2, the Janus colloids have a small but non-negligible thickness of metal

layers (10 nm titanium and 20 nm platinum layer) and the surface roughness of the two distinct faces is different. Hence, as for low aspect ratio ellipsoids, an interfacial rotational friction may manifest in our system.

In the next chapter, we will address further the slowing down of rotational diffusion by showing new experimental results.

### 4.5.3 Propulsion mechanism and active velocity

Here we have demonstrated that by confining the motion of self-propelled particles at the water surface we are able to enhance motion directionality by reducing the particle rotational motion. We also observed that Janus particles propelled away from the catalytic site (Figure 4.10), which agreed with a nanobubble detachment mechanism proposed by Gibbs and Zhao for a similar silica-Pt colloids.<sup>2</sup> However, the direction of motion alone is not enough to determine the mechanism of propulsion, and nanobubbles cannot be observed by optical microscope. Self-diffusiophoresis and self-electrophoresis have been proposed as alternative mechanisms for the propulsion of polystyrene-Pt colloids.<sup>16,17</sup> However, those mechanisms are not able to explain the scaling of the propulsion velocity with the square of the liquid surface tension, as observed for silica-Pt colloids.<sup>2</sup>

An additional major difference between silica-Pt and polystyrene-Pt colloids fabricated so far consists in the thickness of the platinum layer. The thickness used in the latter colloids is about 10 nm or lower.<sup>17,18</sup> Whilst, a thickness of 20 nm or higher was used for silica-Pt colloids.<sup>2</sup> This thickness affects strongly the decomposition rate of  $\text{H}_2\text{O}_2$ ; and for thickness lower than 10 nm the decomposition rate decreases significantly which affects the propulsion mechanism.<sup>18,17</sup>

We can proceed our discussion considering that independently from the differences in propulsion mechanisms, one can always define an effective propulsion force.<sup>19</sup> Here, the propulsion force of the Janus colloid depends on the angle  $\beta$  between the interface normal and the Pt cap normal (see Figure 4.1). As suggested from Figure 4.10,  $\beta$  might lay in between  $45^\circ$  and  $90^\circ$  during directional trajectories, which reduces the propulsion force  $F_P$  by a factor  $\sin(\beta)$ . Nonetheless, the active velocity at the interface is higher than it in the bulk. One might think to attribute this enhancement to a lower translational friction coefficient since the particle is partially immersed in water, and the rest in the air which has a negligible viscosity. For the contact angle we measured, the interfacial friction  $f_T \approx 0.73 \times 6\pi\eta R$  is predicted (see Chapter 1, Section 1.5.3).<sup>8</sup> However as pointed out by MSD analysis, the translational friction at the interface  $f_T \approx 0.95 \times 6\pi\eta R$  is higher than the predicted value (see Section 4.3.4,  $D_T = 0.208 \mu\text{m}^2/\text{s}$ ) in the absence of  $\text{H}_2\text{O}_2$ . This increase of the translational friction at the interface is attributed to the contact line fluctuation, which affects also the rotational friction as discussed before.<sup>15</sup>

The velocity of a self-propelling particle is related to the key parameters of the propulsion mechanism: the interaction length scale  $\tilde{\lambda}$  between solutes and particle in diffusiophoresis (see equation 1.16) and the zeta potential  $\zeta$  of the particle surface in electrophoresis (see equation 1.22). For a particle moving near an interface (gas-liquid, liquid-liquid or liquid-solid), the velocity depends on the competition between the viscous retardation and phoretic propulsion exerted by the interface.<sup>20,21</sup> Relying on self-electrophoresis<sup>17</sup> and referring to literature<sup>21</sup> the velocity for particles moving near the air-water interface was evaluated approximately three

times lower than that in water bulk. Therefore, this could not explain the enhancement of velocity at the interface in our case. In self-diffusiophoresis, assuming that the reaction rate per unit is<sup>17</sup>  $k_r \approx 63.7 \mu\text{m}^2 \text{s}^{-1}$  and taking the obtained velocity of particle in bulk ( $V \approx 10 \mu\text{m/s}$ ), the interaction length between solutes and the colloid is  $\tilde{\lambda} = \sqrt{V / \left(\frac{3\pi}{2} k_r a\right)} \approx 1.8 \text{ nm}$  (see equation 1.18). For an active colloid at the interface, if  $V = 18 \mu\text{m/s}$ , the corresponding interaction length is  $\tilde{\lambda} \approx 2.4 \text{ nm}$ . The increasing of  $\tilde{\lambda}$  at the interface might result from an easier detachment of oxygen bubbles near the water surface than in bulk. However, until now we still cannot draw a full picture to explain this velocity enhancement. Note also that the equation of the interaction length may be different at the interface since the colloid is only partially immersed in the fluid.

To conclude, we have demonstrated that by trapping Janus colloids at the water surface we are able to enhance their directional active motion. Long range directional trajectories have been observed. We explained these findings by the slowing down of the Brownian rotational diffusion at the air-water interface, which is the main limiting factor for achieving directional active motion. In particular, we found that at the same  $\text{H}_2\text{O}_2$  concentration the active velocity of Janus colloid moving at the water surface is significantly higher than it in bulk. This enhancement may be attributed to different boundary conditions at the interface.

## References

1. Howse, J. *et al.* Self-Motile Colloidal Particles: From Directed Propulsion to Random Walk. *Phys. Rev. Lett.* **99**, 048102 (2007).
2. Gibbs, J. G. & Zhao, Y.-P. Autonomously motile catalytic nanomotors by bubble propulsion. *Appl. Phys. Lett.* **94**, 163104 (2009).
3. Wang, Z., Chen, H.-Y., Sheng, Y.-J. & Tsao, H.-K. Diffusion, sedimentation equilibrium, and harmonic trapping of run-and-tumble nanoswimmers. *Soft Matter* **10**, 3209–3217 (2014).
4. Goldmans, A. J., Cox, R. G., Brenner, H. & Neill, O. Slow viscous motion of a sphere parallel to a plane wall-1 Motion through a quiescent fluid. *Chem. Eng. Sci.* **22**, 637–651 (1967).
5. O’Neill, M. E., Ranger, K. B. & Brenner, H. Slip at the surface of a translating–rotating sphere bisected by a free surface bounding a semi-infinite viscous fluid: Removal of the contact-line singularity. *Phys. Fluids* **29**, 913–924 (1986).
6. Gehring, T. & Fischer, T. M. Diffusion of Nanoparticles at an Air/Water Interface Is Not Invariant under a Reversal of the Particle Charge. *J. Phys. Chem. C* **115**, 23677–23681 (2011).
7. Palacci, J., Cottin-Bizonne, C., Ybert, C. & Bocquet, L. Sedimentation and Effective Temperature of Active Colloidal Suspensions. *Phys. Rev. Lett.* **105**, 088304 (2010).
8. Fischer, T. M., Dhar, P. & Heinig, P. The viscous drag of spheres and filaments moving in membranes or monolayers. *J. Fluid Mech.* **558**, 451–475 (2006).
9. Kaz, D. M., McGorty, R., Mani, M., Brenner, M. P. & Manoharan, V. N. Physical ageing of the contact line on colloidal particles at liquid interfaces. *Nat. Mater.* **11**, 138–142 (2012).

10. Blake, T. D. The physics of moving wetting lines. *J. Colloid Interface Sci.* **299**, 1–13 (2006).
11. Holmqvist, P., Meester, V., Westermeier, F. & Kleshchanok, D. Rotational diffusion in concentrated platelet systems measured with X-ray photon correlation spectroscopy. *J. Chem. Phys.* **139**, 084905 (2013).
12. Du, K., Liddle, J. A. & Berglund, A. J. Three-dimensional real-time tracking of nanoparticles at an oil-water interface. *Langmuir* **28**, 9181–9188 (2012).
13. Stocco, A., Mokhtari, T., Haseloff, G., Erbe, A. & Sigel, R. Evanescent-wave dynamic light scattering at an oil-water interface: Diffusion of interface-adsorbed colloids. *Phys. Rev. E* **83**, 1–11 (2011).
14. Nelson, A., Wang, D., Koynov, K. & Isa, L. A multiscale approach to the adsorption of core-shell nanoparticles at fluid interfaces. *Soft Matter* **11**, 118–129 (2015).
15. Boniello, G. *et al.* Brownian diffusion of a partially wetted colloid. *Nat. Mater.* **14**, 908–911 (2015).
16. Ebbens, S. J. & Howse, J. R. Direct observation of the direction of motion for spherical catalytic swimmers. *Langmuir* **27**, 12293–12296 (2011).
17. Brown, A. & Poon, W. Ionic effects in self-propelled Pt-coated Janus swimmers. *Soft Matter* **10**, 4016–4027 (2014).
18. Ebbens, S. *et al.* Electrokinetic effects in catalytic platinum-insulator Janus swimmers. *Europhysics Lett.* **106**, 58003 (2014).
19. Hagen, B. *et al.* Can the self-propulsion of anisotropic microswimmers be described by using forces and torque? *J. Phys. Condens. Matter* **27**, 194110 (2015).
20. Chang, Y. C. & Keh, H. J. Diffusiophoresis and electrophoresis of a charged sphere perpendicular to two plane walls. *J. Colloid Interface Sci.* **322**, 634–653 (2008).
21. Gao, Y. & Li, D. Translational motion of a spherical particle near a planar liquid-fluid interface. *J. Colloid Interface Sci.* **319**, 344–52 (2008).



## Chapter 5

### 5 Rotational diffusion of Janus colloids

#### Introduction

This last chapter is devoted to a deeper discussion on the rotational friction of the active colloids. Cycloidal trajectories in the bulk and at the air-water interface are observed showing that the as-prepared Janus colloids in the presence of fuel are not only generated an effective force but also an effective torque. They are analyzed by the fitting of the velocity autocorrelation function (*VACF*). This yields in principle all the parameters that characterize the cycloidal motion of a colloid at the interface: the speed  $V$  and the angular velocity of the circular translation  $\omega$ , the translational diffusion coefficient  $D_T$ , the rotational diffusion coefficient  $D_R$  and the speed drift  $V_d$ . The rotation of the colloid is also measured and the angular velocity associated is found to be equal to the angular velocity of the circular translation, validating the current model proposed by Ebbens.<sup>14</sup> The ratio  $V/\omega$  yields an estimate of the rotational diffusion coefficient which suggests a strong influence of the contact line pinning dynamics on the degree of persistence of the motion of active colloids at the interface.

We first recall the theoretical description of cycloidal motion associated with the rotation of the colloid. Analysis of the cycloidal motion observed in the bulk will be reported. Finally, the results obtained at the interface will be presented.

#### 5.1 Equations describing rotational motion of an active spherical Janus particle

Geometrically asymmetric microswimmers are able to generate not only an effective propulsive force but also an effective torque which enables the microswimmer to rotate and perform circular or cycloidal trajectories.<sup>1,2,3,4</sup> The presence of an external field, such as the gravitational field, strongly affects the motion of asymmetric microswimmer and a transition from circular-like to straight trajectories was also observed.<sup>5</sup>

Effective torque should not exist for ideal Janus spherical colloids consisting of two equal semi-spherical faces with sharp Janus boundary. Independently from the propulsion mechanism, the direction of the effective propulsive force should always pass through the center of mass of the colloid, owing to the symmetry of the particle. However, reviewing experimental results obtained for spherical Janus colloids, we noted that Howse *et al.* have observed cycloidal trajectories and discussed the possibility of small net angular velocity  $\omega$  which could explain the apparent decrease of the rotational diffusion time ( $\tau_R$ ) if the fuel concentration increased.<sup>7</sup> From the *MSD* analysis, the rotational diffusion time ( $\tau_R = 1/D_R$ ) changed from  $\sim 5.2$  s (theoretical value) to  $\sim 3.5$  s when the fuel concentration increased.<sup>7</sup> Palacci *et al.*<sup>6</sup> fitted *MSD* data using a value of the rotational time equal to 0.9 s, which was significantly smaller than the theoretical value of 1.7 s.

When a spherical Janus colloid performs an active motion in a liquid, a competition between the persistent motion due to the propulsion and the Brownian random motion is observed.<sup>7</sup> The active velocity  $V$  of the colloid could be described in terms of an effective force which depends on the propulsion mechanism of the system.<sup>4,15</sup> The presence of an effective torque acting on the particle

leads to a net angular velocity  $\omega$  of the colloid. An effective torque may occur when the effective force does not pass through the center of mass of the particle.

The velocity autocorrelation function (*VACF*) of an active particle (with an active velocity  $V$  and an angular velocity  $\omega$ ) can be derived by the Langevin equation:<sup>10</sup>

$$\langle \mathbf{v}(\Delta t) \cdot \mathbf{v}(0) \rangle = 4D_{T,0}\delta(\Delta t) + V^2 \cos(\omega\Delta t) \exp(-D_R\Delta t) \quad 5.1$$

The first term  $4D_{T,0}\delta(\Delta t)$  is the Brownian translational contribution which decorrelates very quickly and is described with a Dirac function. The second term describes the active motion characterized by the root mean square average speed  $V$ , the rate of change of the velocity direction  $\omega$  due to active motion and the rotational diffusion coefficient  $D_R$ . This second term is a damped sinusoid. In the absence of Brownian diffusion, the *VACF* of an active particle becomes identical to the one of a macroscopic rigid sphere translating with a velocity  $V$  and rotating with an angular velocity  $\omega$ .

In the following, we recall the equations describing the motion of a rigid body at low Reynolds number in the presence of a torque and consider the particular case of a Janus spherical particle moving in a viscous medium in the absence of Brownian motion. We consider the two-dimensional case depicted in Figure 5.1, where the catalytic face of the particle dictates the direction of the motion: a force  $\mathbf{F}_p$  is acting perpendicular to the Janus boundary of the particle at a distance  $L$  from the center of mass of the particle, so that a torque  $\mathbf{T}_\tau$  is exerted on the particle. The force lays in a two-dimensional plane  $x$ - $y$  while the rotation induced by the torque is about the  $z$ -axis (see Figure 5.1).

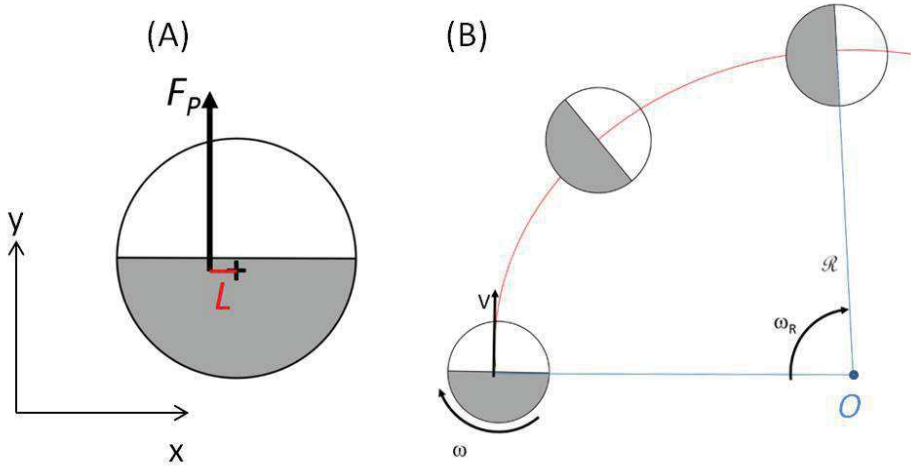


Figure 5.1 (A) A propulsion force  $F_p$  acts on the spherical Janus colloid from a distance  $L$  to the center of mass of the particle. (B) In the absence of Brownian motion, a spherical Janus particle moves within the  $x$ - $y$  plane with a velocity  $V$  and angular velocity  $\omega$ . The trajectory of the moving particle is circular with a radius  $\mathcal{R}$  (from the origin  $O$ ) and a frequency  $\omega_R$ . ( $\omega_R = \omega$ ).



A torque  $\mathbf{T}_\tau$  is the vector product of the force vector and the lever arm  $\mathbf{L}$  vector:

$$\mathbf{T}_\tau = \mathbf{F}_P \times \mathbf{L} \quad 5.2$$

In the Stokes regime,  $dV/dt = d\omega/dt = 0$ :

$$\begin{cases} F_P = V f_T \\ T_\tau = \omega f_R \end{cases} \quad 5.3$$

where  $f_T = 6\pi\eta R$  and  $f_R = 8\pi\eta R^3$  are the translational and rotational Stokes frictions in no-slip condition, respectively.

Hence, a Janus spherical particle as depicted in Figure 5.1 rotates and translates circularly (or revolves) at the same time. The Janus particle, while rotating, is revolving around an external point. The radius of this circular motion  $\mathcal{R}$  obeys:

$$\mathbf{V} = \boldsymbol{\omega}_R \times \mathcal{R} \quad 5.4$$

where  $\boldsymbol{\omega}_R$  is the angular velocity about an axis located in the center of the circular trajectory and  $\mathcal{R}$  is the vector describing the motion of revolution (circular translation).

## 5.2 Active motion in bulk

### 5.2.1 Trajectories of active colloids in bulk

Two-dimensional projections of trajectories for Janus colloids moving in the water bulk at different  $\text{H}_2\text{O}_2$  fuel concentrations are presented in Figure 5.2. Some trajectories are very persistent with cycloidal shapes, such as those at the fuel concentrations of 3% and 5% (Figure 5.2). It means that trajectories of some Janus colloids have a persistent circular contribution in their translational motion and this suggests a break of circular symmetry of the catalytic half area. For the cycloidal motions both counter-clockwise (CCW) or left loops and clockwise (CW) or right loops orbits were observed. More important is that some trajectories cross over from CCW to CW motion such as the red trajectories at 3% and 5% fuel concentrations in Figure 5.2. This crossover from CCW to CW motion reveals a rotation of the colloid about an axis that lies in the plane of the trajectory: for a fixed orientation of the force vector, the lever arm vector  $\mathbf{L}$  (Figure 5.1 (A)) has opposite orientations for CW and CCW motion. The crossover from left loops to right loops in the bulk is pointed out because it reveals an important qualitative difference between bulk and interfacial cycloidal motion. In the bulk, rotations about axes that lie in the plane of the trajectory are allowed while at interface they have never been observed. Whether the rotation is due to Brownian rotational diffusion or is an active rotation is not known, but the rotational diffusion coefficient of the colloid (see below) suggests an active contribution to this rotation. Left loops and right loops are distant by about 3s, which corresponds to an angular velocity of rotation of  $\pi/3$  rad/s. This is a larger value, which reveals the contribution of the persistent active rotation, with respect to the random Brownian rotation ( $D_R = 0.15 \text{ s}^{-1}$ ). The switch from CW to CCW occurs by rotational diffusion only if  $D_{R,x}$  (or  $D_{R,y}$ ) is of the order of  $\omega^2 \Delta t$ .

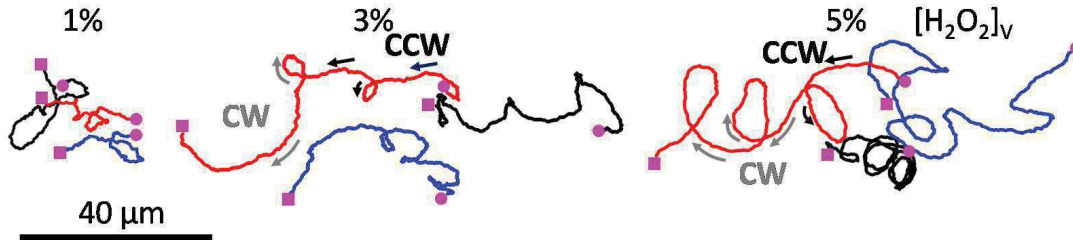


Figure 5.2 Trajectories of two-dimensional projections of Janus particles moving in water bulk under different fuel concentrations ( $[\text{H}_2\text{O}_2]_v$ ) over 15 seconds. The filled circle represents the beginning of the motion and the filled square is the end. The arrows represent rotational directions. There are apparent switches between CCW and CW rotations represented by the red curves at 3% and 5% fuel concentrations.

### 5.2.2 Velocity autocorrelation function of the motion in bulk

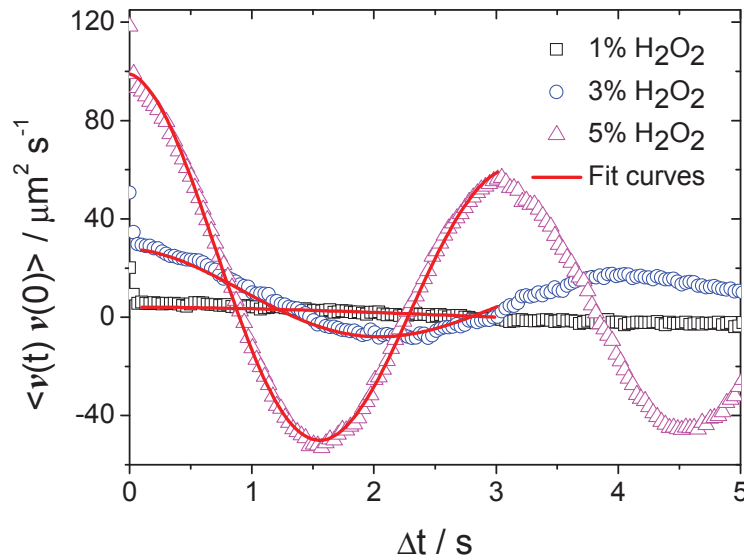


Figure 5.3 Representative velocity autocorrelation functions of motions in bulk versus time delay under different  $\text{H}_2\text{O}_2$  fuel concentrations. Solid lines represent best fits till 3 seconds by equation 5.5.

From the successive positions of the particles, velocity autocorrelation functions of the velocity vector  $\langle \mathbf{v}(\Delta t) \cdot \mathbf{v}(0) \rangle$  have been calculated. Note that the velocity we can determine is not an instantaneous velocity, but it is an average one, averaged over the sampling time of the images. Three examples of  $VACF$  of active motion in the bulk are plotted in Figure 5.3 for different fuel concentrations. They are all characterized by a rapid decrease from  $\Delta t = 0$  to  $\Delta t = 1/30$  s (the time resolution of the record), which characterizes the Brownian passive motion of the colloid. For  $\Delta t > 1/30$  s the  $VACF$  are damped sinusoids oscillating around a value close to but sometimes different from 0 which reveals the uncontrolled drift. Focusing on the damped oscillations,

equation 5.5 has been used to fit the data over 3s (see Figure 5.3), which corresponds to one-fifth of the trajectory duration:

$$\langle \mathbf{v}(\Delta t) \cdot \mathbf{v}(0) \rangle = V^2 \cos(\omega \Delta t) \exp(-D_R \Delta t) + V_d^2 \quad 5.5$$

From the fits, we obtained the active velocity  $V$ , the angular velocity  $\omega$  and also the rotational diffusion  $D_R$ . Note that the angular velocity accessible from the analysis of the successive positions of the colloid is actually  $\omega_R$ , the angular velocity of the revolution in Figure 5.1. But since it will be shown that  $\omega_R = \omega$ , it will be regarded as  $\omega$ . The value of the drift velocity obtained ( $< 2.6 \mu\text{m/s}$ ), which accounts for the advection, is always lower than the active velocity  $V$ .

$V$  versus  $\omega$  is plotted in Figure 5.4 for different concentrations of fuel. Both  $V$  and  $\omega$  increased when increasing  $\text{H}_2\text{O}_2$  concentration. At 5%  $V$  reached an average value of  $\approx 7.7 \mu\text{m/s}$  while  $\omega \approx 2.4 \text{ rad/s}$  at 1%. A linear correlation is observed between  $V$  and  $\omega$  for the whole series, with a correlation coefficient of 0.92. The slope which has the dimension of a length is  $2.7 \pm 0.4 \mu\text{m}$ . This corresponds to the average radius of curvature  $\mathcal{R}$  of the set of cycloidal trajectories as expressed in equation 5.4 and seems not to depend on the fuel concentration contrary to what was observed for geometrically asymmetric microswimmers (see Chapter 1, Section 1.3.1). The linear fit of Figure 5.4 does not pass through the origin:  $V = 1.1 \pm 0.7 \mu\text{m/s}$  when  $\omega = 0 \text{ rad/s}$ , as if a threshold value of the speed was needed for the torque to build up.

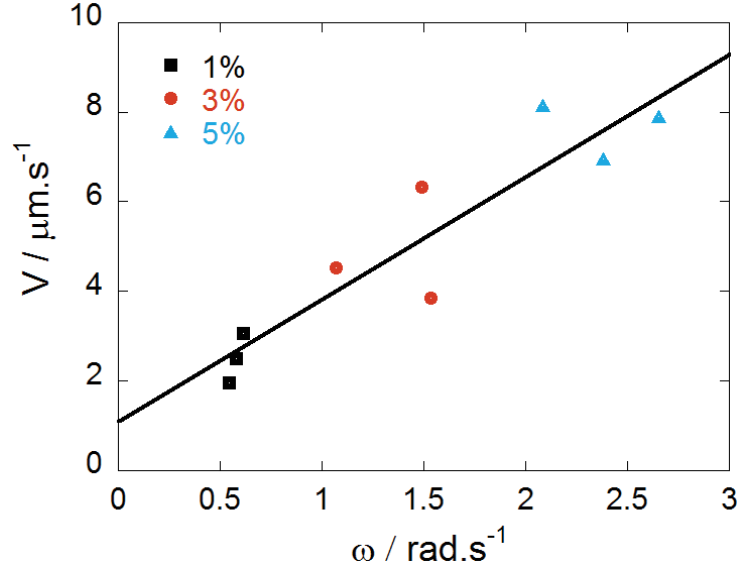


Figure 5.4 Translational velocity as a function of the angular velocity of motions in bulk at different  $\text{H}_2\text{O}_2$  concentrations. The equation of the fitted line is  $V = 2.7\omega + 1.1$  (correlation coefficient is 0.92).

The rotational diffusion coefficient of motion in bulk is obtained from the damping of the  $VACF$ . It is plotted as a function of  $\text{H}_2\text{O}_2$  fuel concentrations in Figure 5.5. A comparison with the theoretical value of rotational diffusion coefficient for a particle moving in bulk ( $D_R = kT/8\pi\eta R^3$ )

in no-slip condition is also plotted. In literature, it was reported that the active translational propulsion of Janus colloids showed a systematic increase of the rotational diffusion coefficients when the fuel concentration increases.<sup>7</sup> Figure 5.5 shows, however, that in our case  $D_R$  does not depend on the activity of the particle. Finally, knowing  $V$ ,  $\omega$ ,  $D_R$  and  $D_T = 6\pi\eta R$  we could evaluate the effective lever arm  $L = \frac{\omega f_R}{V f_T} = \frac{\omega D_T}{V D_R}$  of the propulsive force in the scenario depicted in Figure 5.1. It is constant within experimental error for all fuel concentrations:  $L = 0.41 \pm 0.26\mu\text{m}$  at 1% fuel concentration,  $L = 0.23 \pm 0.09\mu\text{m}$  at 3% and  $L = 0.45 \pm 0.37\mu\text{m}$  at 5%. This suggests that the existence of an effective torque is closely related to the Janus particle itself and probably to some asymmetry of the Pt coated face (See Chapter 2 Section 2.1.1).

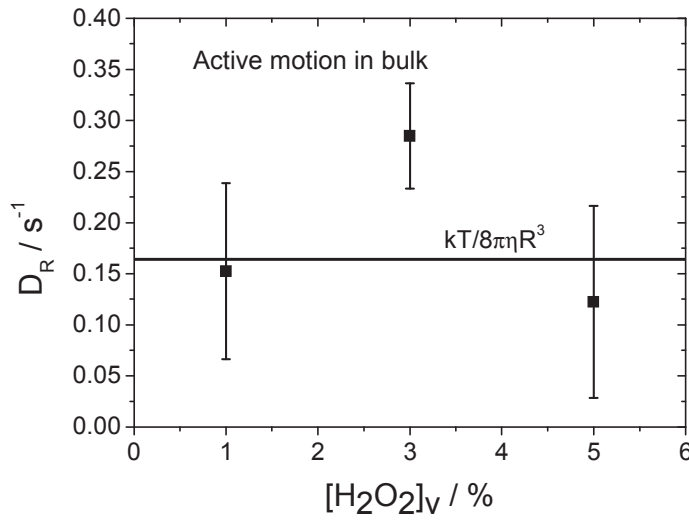


Figure 5.5 Rotational diffusion coefficient of motion in bulk as a function of  $\text{H}_2\text{O}_2$  fuel concentrations. The solid line represents the theoretical rotational diffusion coefficient ( $D_R = kT/8\pi\eta R^3$ ) in bulk.

### 5.3 Rotational diffusion of Janus colloid in the absence of $\text{H}_2\text{O}_2$ at the surface of water

Now we turn our focus to the rotational diffusion of Janus colloids at the surface of water and we address a fundamental question on a possible slowing down of the rotational diffusion even in the absence of any active motion. Hence, we investigated the Brownian rotational and translational motion of Janus colloids in order to check if a slowing down of Brownian diffusion exists as reported for passive spherical and ellipsoidal colloids.<sup>11</sup>

For ellipsoidal colloids at the water surface, the Brownian rotational diffusion could be measured directly by monitoring the vector along the axis (long or short axis) of the particle.<sup>11</sup> In our case by performing image analysis, as described in Chapter 2 Section 2.3.3, the Pt area and the  $\text{SiO}_2$  area of some Janus colloids can be distinguished. Therefore, we can define a rotational angle  $\varphi$  of Pt-cap the variation of which over time characterizes the rotation of the colloid (the definition of  $\varphi$  see Chapter 2, Figure 2.17).

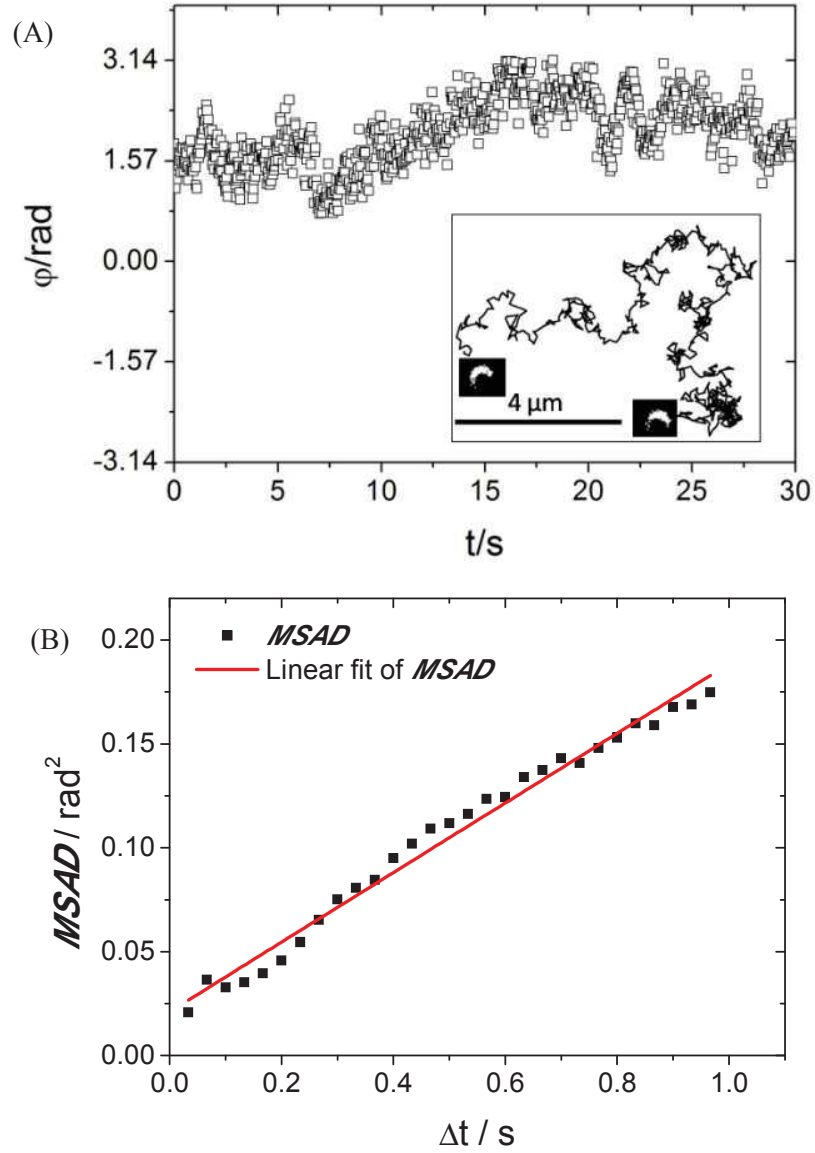


Figure 5.6 (A) Rotational angle  $\phi$  of Janus colloid performing Brownian motion in the absence of fuel. Inserted is the corresponding trajectory with thresholded images representing Pt-cap. (B) Mean squared angular displacement  $MSAD$  as a function of time delay. Solid line is the best fit by equation  $MSAD = MSAD_0 + 2D_{R,0}\Delta t$ .

As shown by the inserted images in Figure 5.6 (A), the white crescents represent the Pt-cap. At the starting and ending points of the trajectory, the location of Pt-cap with respect to the colloid does not change much. The rotational angle  $\phi$  of Janus colloid under Brownian motion (in the absence of  $\text{H}_2\text{O}_2$  fuel) was calculated and plotted as a function of time in Figure 5.6 (A). It shows that the particle rotates in the range of  $\pi/4$  to  $\pi$ .

The mean squared angular displacement ( $MSAD$ ) is calculated and displayed in Figure 5.6 (B). The solid line is the best fit of equation  $MSAD = MSAD_0 + 2D_{R,0}\Delta T$ . The parameter  $MSAD_0$

describes the experimental error on angle  $\varphi$  measurement and depends on the accuracy of the Pt-cap profile detection.  $D_{R,0} = 0.077 \pm 0.049 \text{ s}^{-1}$ . Compared with the theoretic rotational diffusion coefficient of a colloid immersed in water bulk ( $kT/8\pi\eta R^3 = 0.164 \text{ s}^{-1}$ ), the experimental results for Janus colloids at the water surface are smaller by a factor of 2. As discussed in Chapter 4 Section 4.5, this slowing down can be attributed to an interfacial friction due to the fluctuation of the contact line.

## 5.4 Cycloidal motion at the surface of water

### 5.4.1 Trajectories of active colloid at the interface

About 30% of the active colloids observed at interface showed cycloidal motion. Some examples are displayed in Figure 5.7 for the different  $\text{H}_2\text{O}_2$  concentrations studied. Circular and cycloidal trajectories were observed. The rotational motion persists over the observation time of 20 seconds without showing randomization of the motion due to the Brownian rotation. Both CCW (counterclockwise) and CW (clockwise) trajectories were observed. However, each trajectory presents either left loops or right loops, never both! This is a striking difference from the bulk observations described in Section 5.2.1. As already mentioned, considering the case sketched in Figure 5.1, the coexistence of CW and CCW motions in a single trajectory would involve a rotation about an axis within the plane of the trajectory. Contrary to the bulk ones, the interfacial rotational diffusion coefficients  $D_{R,x}$  and  $D_{R,y}$  do not seem high enough to permit such a rotation within 20s nor any possible rotational active motion. Furthermore, if the random rotational diffusion  $D_{R,z}$  was significant, one should not observe a persistence in the radius of curvature of the trajectory  $\mathcal{R}$  as observed.

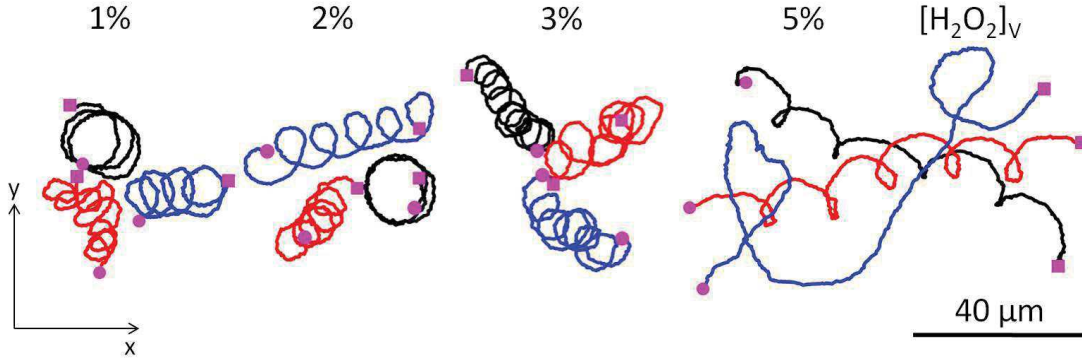


Figure 5.7 Trajectories of Janus particles at the air-water interface ( $x$ - $y$  plane) under different fuel concentrations ( $[\text{H}_2\text{O}_2]_v$ ) over 20 seconds. The filled circle represents the beginning of the motion and the filled square is the end.

### 5.4.2 Velocity autocorrelation function

The  $VACF$  characterizing the cycloidal interfacial motion are presented in Figure 5.8. Comparison of this figure with Figure 5.3 points out negligible damping for interfacial motion. We fitted the  $VACF$  curves for interfacial motions using equation 5.5 up to time delay of 3

seconds, which corresponds to one-tenth of the trajectories duration. The resulting values of the fitting parameters  $V$  and  $\omega$  were robust, however, many pairs of values for  $D_R$  and  $V_d$  lead to fits of similar quality. Except for very few cases, we could not extract both  $D_R$  and  $V_d$ .

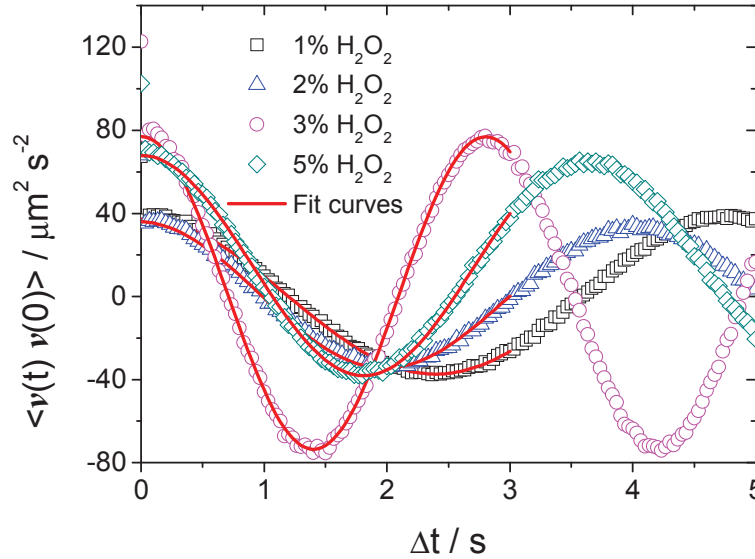


Figure 5.8 Velocity autocorrelation function of motion at the water surface versus time delay under different  $\text{H}_2\text{O}_2$  fuel concentrations. Solid lines represent best fits till 3 seconds by equation 5.5.

The root mean square speed  $V$  versus angular velocities of circular translation  $\omega$  is plotted in Figure 5.9 for the interfacial motions at different fuel concentrations.  $V$  reaches  $12 \mu\text{m/s}$  when the concentration of fuel is 5%. Compared with the active velocities of directional motions presented in Chapter 4 (see Figure 4.5 and 4.7) showing values up to  $18 \mu\text{m/s}$ , the velocity is lower.  $\omega$  ranges from 0.2 to 3 rad/s. The linear correlation between  $V$  and  $\omega$  is less good for interfacial motion than for motion in the bulk: regression coefficient is 0.42 on the whole set of data while it was 0.92 for the bulk data, which was much fewer (Figure 5.4). Many data points obtained at high fuel concentration show small values of  $\omega$ , as if a high concentration of fuel would lower the torque induced by catalytic surface asymmetry.

Since  $V$  and  $\omega$  are particularly uncorrelated at the highest fuel concentration 5% (regression coefficient=0.35), but a linear correlation is apparent at 1% with regression coefficient=0.85, we considered a subset of data reduced enough so that a regression coefficient larger than 0.9 is reached. The data are embedded in the dotted ellipse in Figure 5.9 (A) and the regression coefficient is 0.97. The best fit on this subset of data yields a slope of  $3.1 \pm 0.2 \mu\text{m}$  close to the one obtained in the bulk.  $V = 2.4 \pm 0.3 \mu\text{m/s}$  when  $\omega = 0 \text{ rad/s}$ , significantly higher than the value obtained in the bulk. If this value would correspond to a threshold value of speed in order to build up a significant torque, then it might suggest that a sort of pinning would be higher at the interface than in the bulk. However, it is worth noting that this value is obtained through the fitting of data obtained with different particles and not from the same particle to which more and



more fuel is provided. The variability of the catalytic area from one particle to the other is more probably responsible for the fact that the fits do not pass through the origin.

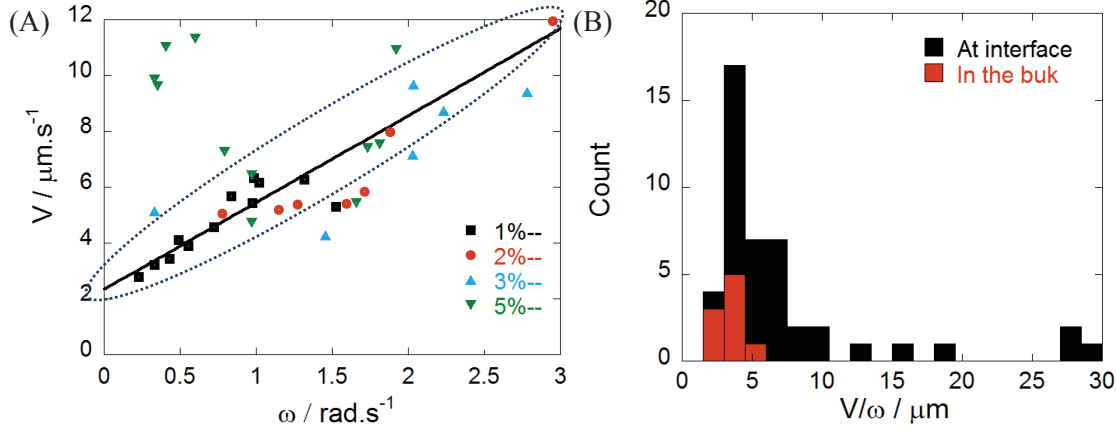


Figure 5.9 (A) Speed as a function of angular velocity under different  $\text{H}_2\text{O}_2$  fuel concentrations. The line corresponds to the best linear fit on the data circled by the dotted ellipse:  $V = 2.4 + 3.1\omega$  (B) Distribution of the values of  $V/\omega$  for trajectories observed in the bulk (red) and at the interface (black).

A more convenient way of looking at the relation between  $V$  and  $\omega$  is to look at the distribution of values of the ratio  $V/\omega$  that is presented in Figure 5.9 (B).  $V/\omega$  reflects the average radius of curvature of the trajectory of a single particle while the slope of  $V$  versus  $\omega$  reflects the radius of curvature of the trajectories averaged over all the particles. The distribution of  $V/\omega$  gives a better picture of the variability from one active colloid to another. Low values of  $V/\omega$  correspond to circular trajectories with a small radius of curvature while more straight trajectories correspond to large values of  $V/\omega$ . The minimum value of  $V/\omega$  that has been measured is  $2.9 \mu\text{m}$ , which is three times the radius of the particle  $R$ .

Considering  $V/\omega$  allows us to evaluate  $D_{R,z}$  following an active rheological approach.  $D_{R,z}$  is related to the rotational friction by  $f_R = kT/D_{R,z}$ . The persistent rotational motion can be described by equations:  $T_\tau = F_P L$ , where  $F_P = V f_T$  and  $T_\tau = \omega f_R$  (see section 5.1). Hence knowing accurately  $V$  and  $\omega$  we can evaluate  $D_{R,z}$  using the following relation:

$$\frac{V}{\omega} = \frac{f_R}{f_T L} = \frac{kT/D_{R,z}}{f_T L} \quad 5.6$$

and

$$\left(\frac{V}{\omega}\right)^{-1} \cdot \frac{kT}{f_T L} = D_{R,z} \quad 5.7$$

where the effective lever arm  $L$  of the propulsion force is, in general, unknown. In Figure 5.10 we plot  $\left(\frac{V}{\omega}\right)^{-1} \cdot \frac{kT}{f_T L}$  as a function of  $\omega$  using  $f_T = 6\pi\eta R$  and assuming  $L = 0.3 \mu\text{m}$  as suggested by the results obtained in the bulk. The results show an increase of the rotational diffusion  $D_{R,z}$  when

increasing the angular velocity. For low angular velocities the calculated  $D_{R,z}$  values (circles in Figure 5.10) agree with the  $D_{R,0}$  of Brownian Janus colloids (the gray region in Figure 5.10 represents the error bar of  $D_{R,0}$ ). When increasing  $\omega$ ,  $D_{R,z}$  increases up to the predicted values in between the bulk and the  $90^\circ$  contact angle predictions (red region in Figure 5.10). Hence our results point to a lower rotational friction  $f_R$  when the angular velocity of the colloids increases. As already described, the low value of  $D_{R,0}$  is attributed to an interfacial friction due to the pinning-depinning dynamics of contact line. Result suggests that an increase of the angular velocity reduces the effect of the pinning-depinning dynamics of contact line<sup>11</sup> and eventually cancels the friction due to the contact line.

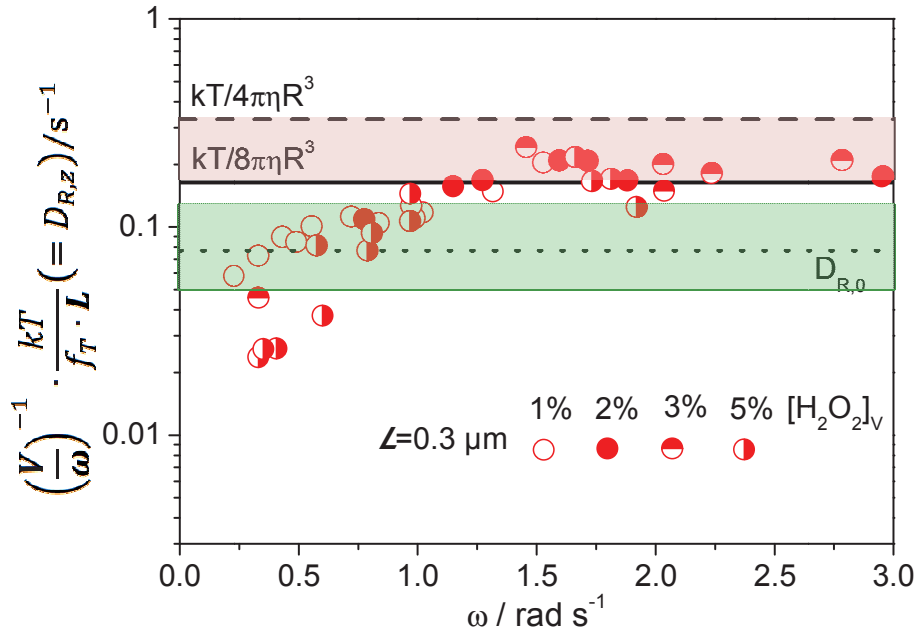


Figure 5.10 The calculated results by using equation 5.7 for estimating  $D_{R,z} = \left(\frac{V}{\omega}\right)^{-1} \cdot \frac{kT}{f_T \cdot L}$  are plotted as a function of experimental rotational velocity  $\omega$ . The arm length is given as  $L = 0.3 \mu\text{m}$  (red circles) according to the value evaluated for particles moving in water bulk. The solid line represents  $D_R$  of a Brownian colloid in water bulk and the dashed line of a half-immersed colloid at water surface (the red region represents  $kT/8\pi\eta R^3 < D_{R,z} < kT/4\pi\eta R^3$ ). The dotted line is the experimental result  $D_{R,0}$  measured for a Janus colloid undergoing Brownian motion (see Section 5.3) and the gray region represents the error bar.

The active rheological approach that has been used to estimate  $D_{R,z}$ , assumes that the angular velocity  $\omega$  characterizing the circular translation (revolution) motion is equal to angular velocity of the rotational motion. The next section aims at showing that this hypothesis is correct.

## 5.5 Rotational motion of Janus colloid at the water surface

As described in section 5.3, for some active Janus colloids moving at the water surface, the Pt-cap could be detected by performing image treatments. The results are presented in Figure 5.11

and the Pt-cap is corresponding to the white crescent. Pt coated surface was always in the rear during the motion, which is in accordance with directional motions described in Chapter 4.

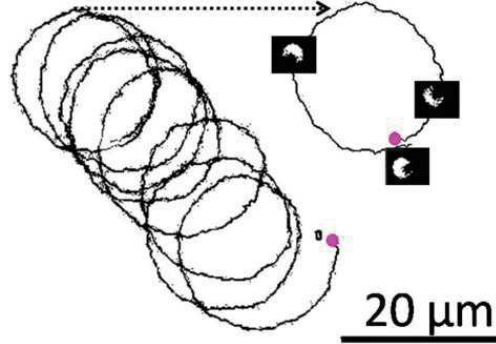


Figure 5.11 Trajectory of a circular motion over 40 seconds. Inserted are the thresholded images of the particle at different locations within a complete loop (magenta filled circle is starting point), and the white crescents are corresponding to Pt-cap.

The rotational angle  $\varphi$  of detected Pt-cap is plotted as the function of time in Figure 5.12. Here  $\varphi$  is ranging from  $-\pi$  to  $\pi$ . Note that close to  $-\pi/2$  data are missing and rotational angles jump. When looking into the thresholded images showing Pt-cap, as presented in the inserted images of Figure 5.12, Pt-cap area detected is rather small and the Janus boundary does not appear clearly which leads to large uncertainty on the  $\varphi$  values. Therefore the data in this region are not reliable. This regular decrease of detected Pt surface area can be attributed to the fact that the light illuminating the Janus particles is not at right incidence. When Pt-cap faces the declined light it gave higher reflection of illumination, while in contrary it gave lower reflection of illumination. Therefore, the rotational angles higher than  $-\pi/2$  (corresponds to large Pt area detected) in Figure 5.12 (B) are more reliable.

The angular velocity of rotation evaluated through image analysis is  $\psi = 1.16 \pm 0.07$  rad/s (see Figure 5.12,  $\varphi = \psi t$ ) which is comparable to the angular velocity calculated by *VACF*:  $\omega = 1.31$  rad/s. We have performed image treatments for all the rotational motions when the Pt-cap of the Janus colloids could be distinguished. The results show that the rotational motions are propelled with Pt-cap at the rear, which means that effective torque is generated at the catalytic surface.

As one can see from Figure 5.11, the trajectory shows rather persistent rotational motion. Therefore, we calculated the angular velocity  $\omega_R$  (definition see Figure 5.1) from the curvature of the trajectory to be  $1.30 \pm 0.002$  rad/s which agrees with the value  $\omega$  extracted from *VACF* analysis and  $\psi$ . It demonstrates that the angular velocity of the colloid  $\omega$  is the same as the angular velocity of the trajectory revolution  $\omega_R$ , as it was discussed at the beginning of this chapter.

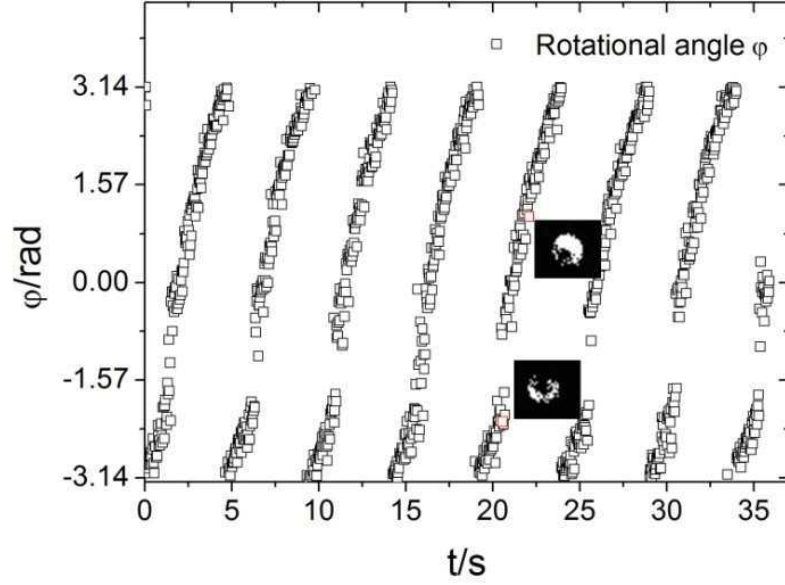


Figure 5.12 Rotational angle  $\phi$  of Pt-cap in the function of time corresponded to the trajectory in Figure 5.11. Inserted are the thresholded images of the particle at different time and white crescents represent Pt-cap.

## 5.6 Conclusions

In this chapter, we have shown some trajectories of Janus particles measured both in the bulk and at the air-water interface of which the net angular velocity  $\omega$  can be accurately measured. In the bulk, we were able to evaluate  $V$ ,  $\omega$  and the rotational diffusion coefficient  $D_R$  from the  $VACF$  (Figure 5.3).  $V$  and  $\omega$  both increase proportionally with the fuel concentration, hence  $V/\omega$  doesn't depend on the fuel concentration or  $\omega$  (Figure 5.4).  $D_R$  calculated by  $VACF$  analysis fluctuates significantly but it agrees with the theoretical prediction (Figure 5.5) and seems to not depend on the fuel concentration or  $\omega$ . Describing the net angular velocity in terms of an effective torque due to the product of the propulsive force and a lever arm as sketched in Figure 5.1, we found  $L \sim 0.2\text{-}0.4 \mu\text{m}$  (see section 5.2.2), which was interpreted in terms of an asymmetric Pt coating of Janus colloids (see Chapter 1, Section 2.1.1).

For motion at the air-water interface, we observed that trajectories strongly differed from the two-dimensional projections of the bulk motion.  $V$  and  $\omega$  do not increase proportionally with the fuel concentration, and  $V/\omega$  seems to be dependent on the angular velocity  $\omega$ . Through image analysis, we were able to show that the Pt coating dictated the motion direction (Figure 5.11) as also observed in Chapter 4 for directional trajectories. Moreover the same angular velocity has been determined for the rotation as for the revolution of the colloids. These observations allows us to validate the simple model of an effective torque due to effective propulsive force acting at a distance  $L$  from the centre of mass of the particle (Figure 5.1 (A)).

We found the absence of switch between CW and CCW rotations and observed trajectories with quite persistent curvatures (Figure 5.7). The absence of this rotational direction switch was related to the decrease of the rotational diffusion coefficients about the axis parallel to the

interfacial plane,  $D_{R,x}$  and  $D_{R,y}$  (see Section 5.4.1). In the absence of fuel, rotational diffusion coefficient  $D_{R,z}$  was calculated (here defined as  $D_{R,0}$  to represent the absence of fuel) and a slowing down due to the contact line fluctuations was observed ( $\frac{D_{R,0}}{8\pi\eta R^3} \approx 0.2$ ), which is similar as that observed for low aspect ratio ellipsoids.<sup>11</sup>

By decoupling the effect of  $\omega$  and rotational diffusion coefficient  $D_R$ , we were able to evaluate the rotational diffusions of Janus colloids moving in the water bulk and at the air-water interface (in the absence or presence of H<sub>2</sub>O<sub>2</sub> fuel).

In the bulk,  $D_R$  values agree with the theoretical prediction ( $kT/8\pi\eta R^3 < D_{R,z} < kT/4\pi\eta R^3$ ). At the interface, in the absence of fuel we observed  $0.077 \pm 0.049 \text{ s}^{-1}$  which is about 5-10 times lower than the prediction. This decrease can be interpreted in terms of an interfacial friction due to the contact line pinning dynamics. We also evaluated the rotational diffusion  $D_{R,z}$  from the rotational friction  $f_R$  of the active motion (see Figure 5.10). We found that  $D_{R,z}$  increases from  $D_{R,0}$  up to the hydrodynamic prediction if the angular velocity increases and this could be interpreted in terms of a reduced interfacial friction due to the pinning of the contact line. In other words, the pinning of the contact line becomes less effective when the particle is able to rotate in a persistent way.

## References

1. Gibbs, J. G. & Zhao, Y. P. Design and characterization of rotational multicomponent catalytic nanomotors. *Small* **5**, 2304–2308 (2009).
2. Gibbs, J. G., Kothari, S., Saintillan, D. & Zhao, Y. P. Geometrically designing the kinematic behavior of catalytic nanomotors. *Nano Lett* **11**, 2543–2550 (2011).
3. K ummel, F. *et al.* Circular Motion of Asymmetric Self-Propelling Particles. *Phys. Rev. Lett.* **110**, 198302 (2013).
4. Ten Hagen, B. *et al.* Can the self-propulsion of anisotropic microswimmers be described by using forces and torques? *J. Phys. Condens. Matter* **27**, 194110 (2015).
5. Hagen, B. *et al.* Gravitaxis of asymmetric self-propelled colloidal particles. *Nature Communications* **5**:4829 (2014).
6. Palacci, J., Cottin-Bizonne, C., Ybert, C. & Bocquet, L. Sedimentation and effective temperature of active colloidal suspensions. *Phys. Rev. Lett.* **105**, 1–4 (2010).
7. Howse, J. *et al.* Self-Motile Colloidal Particles: From Directed Propulsion to Random Walk. *Phys. Rev. Lett.* **99**, (2007).
8. Gibbs, J. G. & Zhao, Y. P. Autonomously motile catalytic nanomotors by bubble propulsion. *Appl. Phys. Lett.* **94**, 163104 (2009).
9. Brown, A. & Poon, W. Ionic effects in self-propelled Pt-coated Janus swimmers. *Soft Matter* **10**, 12 (2014).

10. Ebbens, S., Jones, R. a L., Ryan, A. J., Golestanian, R. & Howse, J. R. Self-assembled autonomous runners and tumblers. *Phys. Rev. E* **82**, 015304 (2010).
11. Boniello, G. *et al.* Brownian diffusion of a partially wetted colloid. *Nat. Mater.* **14**, 908–911 (2015).
12. O’Neill Ranger, K. B., Brenner, H., M. E. Slip at the surface of a translating–rotating sphere bisected by a free surface bounding a semi-infinite viscous fluid: Removal of the contact-line singularity. *Phys. Fluids* **29**, 913–924 (1986).
13. Takagi, D., Braunschweig, A. B., Zhang, J. & Shelley, M. J. Dispersion of self-propelled rods undergoing fluctuation-driven flips. *Phys. Rev. Lett.* **110**, 1–5 (2013).
14. Archer, R. J., Campbell, a. I. & Ebbens, S. J. Glancing angle metal evaporation synthesis of catalytic swimming Janus colloids with well defined angular velocity. *Soft Matter* **11**, 6872–6880 (2015).
15. Yan, W. & Brady, J. F. The swim force as a body force. *Soft Matter* **11**, 6235–6244 (2015).





## Conclusions and Perspectives

In this thesis the active motion of isolated platinum-silica (Pt-SiO<sub>2</sub>) Janus colloids at the surface of water was realized and deeply investigated. The hydrophilic Janus colloid straddled the two-dimensional water surface with its catalytic face in contact with the liquid. Therefore the catalytic surface could react with hydrogen peroxide (H<sub>2</sub>O<sub>2</sub>) in the water subphase and generate propulsion parallel to the interfacial plane.

The propulsion velocity measured was as high as 18  $\mu\text{m s}^{-1}$  at H<sub>2</sub>O<sub>2</sub> concentration of 5% in volume, which was twice the value measured for colloids moving in the bulk. The active colloids performed very persistent motions at water surface, which means that randomization of the velocity direction is very slow and hardly observable in the accessible time window. We distinguished two types of trajectories: nearly straight trajectories with only few directional changes and circular or cycloidal trajectories. Each cycloidal trajectory is associated with either clockwise or counter-clockwise rotation of the particles. It is worth noting that the rotation can switch from one orientation to the other in the bulk, but not at interface, which is clear sign of the strong slowing down of the rotational diffusion about an axis perpendicular to the interface normal.

The persistence of the motion was attributed to the slowing down of Brownian rotational diffusion for colloids moving at water surface. The rotations of colloid around the axes parallel to the air-water interfacial plane are significantly slowed down because of the high dissipation close to the triple line, which is the same dissipation described in the dynamics of partial wetting. On the other hand, the Brownian rotational diffusion about an axis parallel to the interface normal were found to be lower than the theoretical value for colloids at water surface in absence of fuel, which could be due to extra interfacial frictions due to the pinning dynamics of the contact line. Our results point to an increase of the rotational diffusion  $D_{R,z}$  from the low value measured in passive condition up to the theoretical prediction when the angular velocity of the colloid increases.

The wetting properties and the orientation of Janus colloids were also investigated. The contact angle of colloids at air-water interface was measured by using optical microscopy and gel-trapping method while the energies of platinum coated surface and silica surface were estimated through static contact angle measurements for different liquids with planar substrates. The orientation of Janus colloids at water surface was observed by using both optical microscopy and scanning electronic microscopy. We found that most of the Janus colloids oriented with their Janus boundaries (where two faces meet) out of the air-water interfacial plane. This ensures contact between the catalytic area and the bulk fuel reservoir and lead to the generation of effective propulsions in the presence of fuel. The orientations combined with the partial wetting properties were pivotal for the realisation of two-dimensional active motions for colloids at water surface. The energy landscapes for Janus colloids at air-water interface as a function of its contact angle and orientations were also described. We found that the contact angle hysteresis and the non-equilibrium orientations could be attributed to chemical or physical heterogeneities present on the two faces of the Janus colloid.

For the preparation of Janus colloids, metal deposition technique was used. We also proposed a chemical approach for the fabrication. The silica particles were first stabilized by Pickering-

emulsion and then the bared surface was chemically modified and platinum was loaded after. However, the products didn't show any active motion in the presence of  $\text{H}_2\text{O}_2$  while the colloidosomes generated gas bubbles on the surface. We proposed the platinum layer may be very thin which couldn't generate effective propulsion. Therefore, further improvement of this method can be done by growing more platinum onto the particle surface.

For the further investigations on Janus colloids moving at the surface of water, some improvements can be done. First of all, to study the rotational diffusion of spherical colloids, fluorescent particles are preferred for better observation. We have already prepared Janus colloids by half coating fluorescent particles through platinum deposition and a first study of the colloid under Brownian motion at water surface was done as shown in Figure 1.

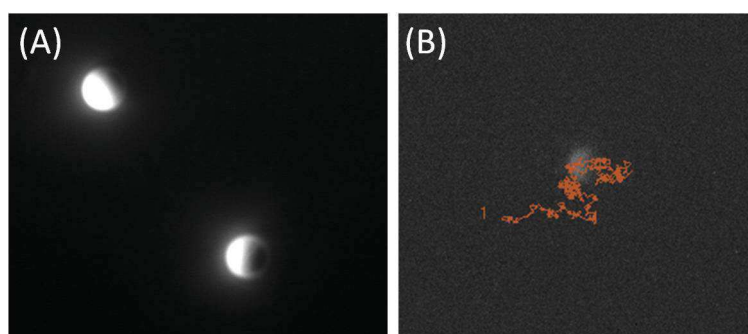


Figure 1 (A) Optical microscopic image of Janus colloids with the invisible parts coated by platinum. (B) The orange curve represents the trajectory of the visible fluorescent part of colloid under Brownian motion.

Secondly, the wetting property of Janus colloids can be tuned and the dependence of active motion on contact angle will be of great interests.

We have shown rotational propulsion for the spherical Janus colloids at water surface. However the geometries of the catalytic surfaces were not well controlled which led to different torques acting on isolated particles. We propose to fabricate geometrically asymmetric active colloids by using glancing angle metal evaporation technique to control the rotational propulsion.

For the active system at interface, the investigation of the Marangoni effect due to surface tension gradient is also very interesting. We have studied the wetting property of platinum-silica Janus colloids at aqueous solution of the surfactant sodium dodecyl sulfate (SDS) at the critical micellization concentration (CMC). The surface tension of this solution was  $\gamma = 35.53 \pm 0.39$  mN/m. As shown in Figure 2, the Janus colloids stayed at the interface of air-SDS solution showing very small contact angles. This specific wetting properties combined with Marangoni effect may give a rich scenario for the active motion of Janus colloids at interface.

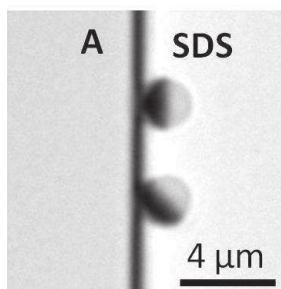


Figure 2 Optical microscopic image of Janus colloids at air-SDS aqueous solution interface. The black faces are corresponding to the Pt-coated surfaces.

We have well studied the motion of isolated platinum-silica Janus colloids at water surfaces under two-dimensional confinement. The motion in more complex situations such as active Janus colloids moving in the crowd of passive particles (undergoing Brownian motion) is still worth of investigations. We have obtained preliminary results as shown in Figure 3. The moving Janus colloid pointed out by red circles pushed the passive colloids in front and “opened up a new road” (red arrows) to go through. The dynamics and interactions between the moving Janus colloid and passive colloids all deserved to be studied.

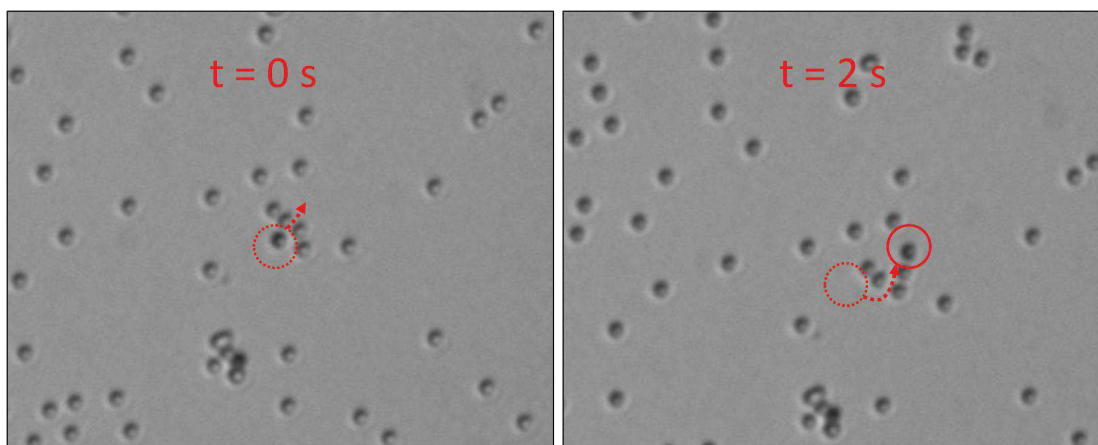


Figure 3 The motion of Janus colloid (pointed by the red circles) in a crowd of passive colloids at water surface in the presence of  $\text{H}_2\text{O}_2$  fuel. The images show the motion at time 0 and 2 seconds recorded by video microscope. The arrows represent moving direction.



## List of symbols

$a$  = diameter of solute molecules

$A_i$  = interfacial area

$b$  = slip length

$c$  = concentration

CW = clockwise

CCW = counterclockwise

$D_B$  = bulk translational diffusion coefficient

$D_{eff}$  = effective diffusion coefficient

$D_R$  = bulk rotational diffusion coefficient

$D_{R,\parallel}$  = rotational diffusion coefficient about an axis parallel to the interface normal

$D_{R,\perp}$  = rotational diffusion coefficient about an axis perpendicular to the interface normal

$D_T$  = translational diffusion coefficient

$E_F$  = electric field

$E, E_{i-j}$  = free energy

$F_f$  = friction force

$F_P$  = propulsion force

$F$  = tangential force per unit length

$f$  or  $f_T$  = translational friction coefficient

$f_R$  = rotational friction coefficient

$f_{T,\perp}$  = translational friction coefficient perpendicular to the interface

$f_{T,\parallel}$  = translational friction coefficient parallel to the interface

$f_{R,\perp}$  = rotational friction coefficient perpendicular to the interface

$H$  = hysteresis force

$\hbar$  = local specific enthalpy increment

$h$  = distance and height

$j$  = current density

$k_r$  = the chemical reaction rate per unit area

$k'$  = chemical reaction rate constant

$kT$  = thermal energy

$K$  = conductivity

$k_T^{(0)}$  = interfacial translational friction factor

$k_{\perp}^r$  = rotational friction factor about an axis perpendicular to the interface normal

$k_{\parallel}^r$  = rotational friction factor about an axis perpendicular to the interface normal

$L$  = length, level arm length

$m$  = mass

$MSAD$  = mean squared angular displacement

$MSD$  = mean squared displacement

$W$  = work of adhesion

$n_d$  = 1, 2, 3-dimension

$n_m$  = molar number

$n$  = number of lag time

$N$  = number

$P$  = pressure

$Pe$  = Péclet number

$\mathbf{r}_i$  = particle positions

$R$  = particle radius

$\mathcal{R}$  = radius of circular motion

$Re$  = Reynolds number

$R_g$  = universal gas constant

$\Delta t$  = lag time or delay time

$\delta t$  = the lag time between two consecutive frame

$t$  = time

$T$  = temperature,

$T_{eff}$  = effective temperature

$T_{\tau}$  = torque

$U, u$  = velocity

$V, v_i$  = velocity modulus or speed

$V_d$  = drift velocity

$\mathbf{v}$  = velocity vector

$V'$  = volume

$VACF$  = velocity autocorrelation function

$\nabla Y$  = gradient of the field potential

$z$  = vertical coordinate and distance

### **Greek Symbols**

$\alpha$  = contact angle

$\beta$  = angle between the platinum face normal with the  $z$ -axis

$\tilde{\beta}$  = dimensional sliding friction coefficient

$\varepsilon$  = dielectric constant

$\varphi$  = angle between platinum face with  $x$ -axis

$\gamma$  = interfacial tension

$\eta$  = dynamic viscosity

$\tilde{\lambda}$  = interaction length between the solute and the particle

$\lambda_{\eta}$  = viscosity ratio

$\lambda_t$  = tumbling rate

$\lambda_t^{-1}$  = the mean run time of bacteria

$\lambda$  = length of contact line jump

$\rho$  = density

$\rho_I$  = first moment particle distribution

$\sigma$  = shear stress



$\tau_{ar}$  = angular momentum relaxation time

$\tau_{mr}$  = momentum relaxation time

$\tau_R$  = rotational diffusion time

$\tau_t$  = tumbling time

$\mu_E$  = electrophoretic mobility

$\mu_Y$  = slip-velocity coefficient

$\omega$  = angular velocity

$\zeta$  = zeta potential

## Résumé

Considérant une particule isolée, la différence principale entre un colloïde actif et un colloïde passif réside dans le temps de persistance du régime balistique. La transition du régime balistique vers le régime diffusif est déterminée dans les deux cas par des coefficients de friction ou de manière équivalente par des coefficients de diffusion. Le mouvement d'une particule colloïdale passive micrométrique est diffusif lorsqu'il est observé sur des intervalles de temps d'au moins une microseconde, suffisamment longs pour que la direction de la quantité de mouvement soit rendue aléatoire par des collisions avec les molécules de solvant. A l'échelle macroscopique ces collisions se traduisent par un coefficient de friction de translation. Pour une particule colloïdale active, un mouvement diffusif est observé pour des intervalles de temps de plusieurs secondes, suffisamment longs pour que la direction d'auto-propulsion soit rendue aléatoire par la diffusion rotationnelle de la particule.

Dans cette thèse, nous étudions le mouvement d'une particule colloïdale active déposée à la surface de l'eau. Des particules Janus aux propriétés catalytiques ont été préparées par dépôt de platine métal à la surface de particules de silice. La profondeur d'immersion des particules ainsi que leur orientation par rapport à la surface de l'eau ont été caractérisées et discutées en tenant compte des propriétés de mouillage non-uniformes de la surface des particules Janus. Le mouvement de particules isolées en présence de quantités variables d'eau oxygénée utilisée comme source d'énergie, a été enregistré par vidéo-microscopie optique et les trajectoires analysées en termes de déplacement carré moyen et de fonction d'auto-corrélation des vitesses. L'observation de deux types de trajectoires, rectilignes et circulaires, révèle la force effective ainsi que le couple induit par la décomposition catalytique de l'eau oxygénée à la surface de la particule Janus. Le résultat principal de ce travail est que le mouvement des particules actives confinées à l'interface persiste plus longtemps dans le régime balistique que celui de particules actives totalement immergées en solution. Ceci est dû au confinement qui réduit le nombre de degrés de liberté de rotation mais aussi aux conditions de mouillage partiel qui font apparaître des contributions supplémentaires à la friction de rotation.

Mots clés : Colloïde Janus, mouvement actif, interface eau-air, mouillage partiel





## **Abstract**

At the single-particle level, the main difference between active colloids and passive ones is the time scale over which the motion crosses from ballistic to diffusive regime. In both cases, friction coefficients or equivalently diffusion coefficients determine this time scale. For instance, the motion of a passive colloid of  $1\mu\text{m}$  radius is diffusive when observed over lag times longer than a microsecond, once the direction of its momentum has been randomized by collisions with solvent molecules. At the macroscopic scale, these collisions are accounted for by the translational friction coefficient. For an active colloid, the effective diffusive behavior observed over lag times larger than few seconds results from the randomization of the direction of self-propulsion by rotational diffusion.

In this thesis, we investigated the motion of an active Janus colloid trapped at the air-water interface. Spherical catalytic Janus colloids have been prepared through the deposition of platinum metal at the surface of silica particles. Immersion depth of the Janus colloid as well as their orientation with respect to the water surface has been characterized and interpreted in terms of the non-uniform wetting properties of the Janus particles. The motion of the active Janus colloids in the presence of various concentrations of hydrogen peroxide ( $\text{H}_2\text{O}_2$ ) as fuel was characterized by video microscopy and the trajectories analyzed through the mean square displacement and the velocity autocorrelation function. The types of trajectories, directional and circular ones that we observed in our experiments, revealed the effective force and torque induced by the catalytic decomposition of  $\text{H}_2\text{O}_2$ . At the water surface, active colloids perform more persistent directional motions as compared to the motions performed in the bulk. This has been interpreted as due to the loss of degrees of freedom resulting from the confinement at the interface and also to the partial wetting conditions that possibly bring new contributions to the rotational friction at the interface.

**Keywords:** Janus colloid, active motion, air-water interface, partial wetting